MECHANISMS OF ELECTROHYDRODYNAMIC TWO-PHASE FLOW STRUCTURES AND THE INFLUENCE ON HEAT TRANSFER AND PRESSURE DROP

MECHANISMS OF ELECTROHYDRODYNAMIC TWO-PHASE FLOW STRUCTURES AND THE INFLUENCE ON HEAT TRANSFER AND PRESSURE DROP

By

Kevin Ng, B.Eng

A Thesis

Submitted to the School of Graduate Studies

in Partial Fulfillment of the Requirements

for the Degree

Masters of Applied Science

McMaster University

Hamilton, Ontario, Canada

MASTERS OF APPLIED SCIENCE (2010)
(Mechanical Engineering)

McMASTER UNIVERSITY
Hamilton, Ontario, Canada

TITLE	Mechanisms of Electrohydrodynamic Two-Phase Flow Structures and the Influence on Heat Transfer and Pressure Drop
AUTHOR	Kevin Ng, B.Eng
SUPERVISOR	Dr. J.S. Cotton Department of Mechanical Engineering
NUMBER OF PAGES	xviii, 168

ABSTRACT

The objectives of this research is to determine the mechanisms involved in the development of electrohydrodynamic (EHD) flow structures, such as twisted liquid cones, twisted liquid columns and entrained liquid droplets, in a two-phase flow and to determine their impact on convective condensation heat transfer. EHD involves the application of high voltage to a dielectric fluid flow to induce electric forces that can create additional convection currents in single-phase and two-phase flows and also the redistribution of the different phases within the channel in a two-phase flow. The EHD phenomenon was investigated inside a smooth horizontal tube with a concentric rod electrode used to apply high voltage to a flow of refrigerant R-134a.

The EHD flow structures were initially observed to be a transient phenomenon that appeared during the initial step input of high voltage and were not present after steady state. Investigations to sustain the EHD two-phase flow structures using various ±8kV pulse width modulated waveforms (PWM) are performed for a range of mass flux between 45 to 110kg/m^{2}s and a quality of 50%, conditions which correspond to a stratified/stratified wavy flow pattern. The effect of sustaining flow patterns consisting of these flow structures on condensation heat transfer and pressure drop is measured. The purpose of this research is to evaluate the potential of sustaining specific EHD two-phase flow patterns as a means of enhancement and control of heat transfer and pressure drop for industrial heat exchange applications.

An evaluation of the mechanisms involved in the development of the EHD flow structures was first performed by determining the effect of applying positive and negative

polarity high voltage to a single-phase flow to determine the mechanisms of charge injection in this particular geometry. A negative polarity high voltage applied to the concentric rod electrode was found to result in a larger heat transfer enhancement due to the charge injection occurring at the center electrode, whereas a positive polarity high voltage applied to the rod electrode resulted in negative charge injection at the grounded tube wall. This method of charge injection was used to explain the difference in the development of the twisted liquid cone and twisted liquid column flow structures that arise due to an applied positive and negative voltage respectively.

An analysis of the development and sustainability of the EHD two-phase flow structures using various PWM waveforms was investigated using a high speed camera to visualize the flow. An image analysis of these high speed videos determined the suitable pulse width, duty cycle and voltage polarity conditions for the development of the twisted liquid cones/columns and in sustaining the structures during the pulse ON period. The sustainability of these flow structures were determined to be mainly influenced by the charge distribution within the flow and a means to sustain these flow structures for a range of duty cycles between 10%-90% was found using waveforms consisting of both positive and negative high voltage pulses. For duty cycles of 100%, an inverse annular flow pattern was observed, where liquid is extracted and encircles the concentric rod electrode. For the entrained droplets produced using EHD, the required high voltage pulse conditions for the production of the droplets was determined and the effect of EHD on the coalescence of droplets was also observed.

Experiments were performed to measure the condensation heat transfer and pressure drop performance of flow patterns consisting of EHD flow structures. The results show that flow patterns consisting of different EHD flow structures exhibit different heat transfer and pressure drop characteristics. The heat transfer enhancement was determined to be a result of the extraction of liquid from the heat transfer surface and into the central core, the increase in convection within the phases and a disruption of the thermal boundary layer. The increase in pressure drop is due to the increase in frictional pressure drop between the liquid and electrode surfaces and an increase in the interfacial area resulting in greater liquid-vapour shear. The maximum enhancement of heat transfer and the maximum increase of pressure drop by using the EHD technique were determined to be 2.9-fold and 5.0-fold respectively. The results also indicate that EHD can be used to independently control the heat transfer and pressure drop as it was shown that for a fixed heat transfer or pressure drop performance, a range of corresponding pressure drop or heat transfer conditions can be achieved depending on the flow pattern established using PWM waveforms. The findings in this study show the promise in utilizing the EHD technique as an effective means of enhancement and control of heat transfer and pressure drop performance in advanced heat exchange systems.

ACKNOWLEDGEMENTS

First and foremost, I would like to acknowledge my sincerest gratitude to Dr. Jim Cotton for his exceptional supervision, guidance, support and friendship provided throughout my studies. It was a pleasure working with you throughout this thesis and I believe that the success of this thesis is attributed to your commitment to your students. I would also like to thank Dr. Chan Ching for his guidance and unique ability to motivate. His involvement in this research was similar to that of a co-supervisor and I would like to acknowledge his efforts. Special thanks is given to Dr. Jen-Shih Chang and Dr. Hossam Sadek, whose advice and insight into this research was invaluable.

I would like to acknowledge the support from the mechanical engineering technicians Joe Verhaeghe, J.P. Talon, Ron Lodewyks, Mark MacKenzie and Jim McLaren and also to the mechanical engineering staff Lily Sazz-Fayter, Florence Rosato and Vania Loyzer for your kind help. I would also like to thank the organizations NSERC and OGS for providing financial support and funding this research.

To my family, friends and colleagues in the Thermal Management Research Laboratory and Mechanical Engineering Department, I would like to thank you for your support. The time spent during this period of study was an amazing experience because of all the wonderful people that I have encountered.

Finally, I would like to thank Diane Le for her encouragement and understanding throughout this period. Thank you for believing in me and making this accomplishment possible.

TABLE OF CONTENTS

LIST OF TABLES

LIST OF FIGURES

NOMENCLATURE

Symbols

A	Flow area (m^2)
Bo	Boiling number
D	Diameter [m]
$\bar{D}$	Dielectric displacement [C/m^2]
D_h	Hydraulic diameter [m]
D_i	Diffusion coefficient of ions [m^2/s]
$\bar{E}$	Electric field strength [V/m]
$\bar{E}_b$	Electric breakdown strength [V/m]
Ehd	EHD number
$\bar{F}_E$	Electric force [N]
Fr	Froude number
G	Mass flux [kg/m^2s]
Ga	Galileo number
I	Electric current [A]
Ja_l	Liquid Jakob number
K^*	Characteristic wave number [1/m]
L	Characteristic length scale [m]
Md	Masuda number
Nu	Nusselt number
Nu_E	Nusselt number in the presence of an electric field
P	Pressure [Pa]
$\boldsymbol{P}$	Non-dimensional pressure
Pr	Prandtl number
Re	Reynolds number
T_C	Electrical stability parameter
T_s	Surface temperature [K]
T_{sat}	Saturation temperature [K]
U	Velocity [m/s]
V	Voltage [V]
V_E	Dimensionless parameter for electric force/surface tension
V_{eff}	Effective voltage [V]
V_p	Pulse voltage [V]
W	Work [J]
$\bar{W}$	Work function [eV]
We	Weber number
X	Lockhart-Martinelli parameter
c	Speed of sound[m/s]
c_p	Specific heat [J/kgK]
d	Material thickness [m]
e	Energy of an electron, $1.602\ x\ 10^{-19}$[J] or 1 [eV]
f	Friction factor
$\bar{f}_{eB}$	Electric body force [N/m^3]
g	Acceleration due to gravity, 9.81 [m/s^2]
h	Planck's constant, $6.626\ x\ 10^{-34}$[Js]
h	Heat transfer coefficient [W/m^2K]
h_{lv}	Latent heat of evaporation [kJ/kg]
h'_{lv}	Modified latent heat of evaporation [kJ/kg]
$\bar{J}$	Current density [A/m^2]
$\bar{J}_D$	Displacement current density [A/m^2]
k	Thermal conductivity [W/mK]
$\dot{m}$	Mass flow rate [kg/s]
m_e	Electron mass, $9.91\ x\ 10^{31}$[kg]
$\bar{n}$	Unit vector
q	Electric charge [C]
$q"$	Heat flux [W/m^2K]
q'''_{eB}	EHD energy generation rate per unit volume [W/m^3]
r	Radius [m]
t	Time [s]
$\bar{u}$	Velocity [m/s]
$\bar{\boldsymbol{u}}$	Non-dimensional velocity

x	Mass vapour quality
x_F	Potential barrier thickness [m]
x_L	Distance scale [m]
$\tilde{x}$	Non-dimensional length
z	Axial distance [m]

Greek Symbols

α	Void fraction
β	Volumetric thermal expansion coefficient [1/K]
δ	Uncertainty
ε	Dielectric permittivity [N/V^2]
ε_r	Dielectric constant, $\varepsilon/\varepsilon_o$
ε_o	Dielectric permittivity in free space, $8.85\ x\ 10^{-12}$ [N/V^2]
η	Non-dimensional electric field
λ	Wavelength [m]
λ_c	Charge density per unit length [C/m]
λ^*	Most unstable wavelength in the presence of an electric field [m]
μ	Dynamic viscosity [Pas]
μ_e	Ion mobility [m^2/Vs]
ν	Kinematic viscosity [m^2/s]
ϕ	Two-phase multiplier
ϕ_E	Electric flux [V/m]
Φ	Fermi energy [eV]
ρ	Density [kg/m^3]
ρ_c	Space charge density [C/m^3]
θ	Non-dimensional temperature
σ	Surface tension [N/m]
σ_e	Electric conductivity [S/m]
τ	Non-dimensional time
τ_c	Charge relaxation time [s]
τ_1	Pulse width [ms]
τ_2	Period [ms]

Subscripts

R	Refrigerant
T	Temperature
$elec$	Electrical preheater
fr	Frictional
in	Inlet
l	Liquid
lo	Liquid only
o	Reference
out	Outlet
o^+	Positive ion
o^-	Negative on
tp	Two-phase
v	Vapour
vo	Vapour only
w	Water
S, sat	Saturated
sub	Subcooled

Chapter 1 – Introduction

1.1 Advanced Heat Exchange Technology

Heat exchange technology is used in many different industries such as power generation, refrigeration, automotive and aerospace. In each application, methods in enhancing heat transfer has received considerable interest because of the potential benefits for increased efficiency, reduction in the physical size of the heat exchanger and control over the heat transfer and pressure drop performance. All these benefits in using enhancement and control techniques can result in substantial capital and operational costs when compared to systems with no heat transfer augmentation.

There is a wide variety of enhancement techniques available for implementation in heat exchangers and these techniques can be classified under two categories: *passive* or *active* techniques. Passive techniques do not require the addition of any external power while active techniques require the addition of external power for enhancement. A summary of both types of enhancement techniques can be found in Webb and Kim (2005) and is given in Table 1.1(a) and Table 1.1(b).

Although there are many active enhancement methods available, passive techniques remain the method of choice in commercial applications because of the lower capital cost and concerns over safety and reliability of active methods. However, research in active enhancement methods remains high because of the greater range of control over

Table 1.1 – Heat transfer enhancement techniques.
Summarized from [Webb and Kim (2005)]

a) Passive Techniques

Technique	Description	Applicability
Coated Surfaces	Non-wetting coating (Teflon) to promote dropwise condensation.	Two-phase.
Rough Surfaces	Formed by machining or restructuring surface - promotes boundary layer mixing and increase in heat transfer area	Single or two-phase
Extended Surfaces	Reduce thermal resistance by increasing heat transfer coefficient or area.	Single or two-phase.
Displaced Insert	Inserts (eg. Coils) inside to improve energy transport from heated surface. Either used for mixing main flow or disturbing boundary layer without affecting main flow.	Single or two-phase.
Swirl Flow	Twisted tape. Create Secondary flow.	Single or two-phase.
Surface Tension	Condensate drainage technique.	Two-phase.
Additives for Liquid	Solid particles or gas bubbles in single-phase flows.	Single-phase liquid.
Additives for Gas	Liquid droplets or solid particles.	Single-phase gas.

b) Active Techniques

Technique	Description	Applicability
Mechanical Aids	Stirrers or surface rotators.	Widely used for viscous fluids.
Surface Vibration	Piezoelectric device to vibrate surface or impinge droplets onto heated surface (two-phase).	Mainly for single-phase. Occasionally two-phase.
Fluid Vibration	Vibrate fluid.	Mainly for single-phase.
Injection	Supply gas through porous heat transfer surface to a flow of liquid.	Augmentation method for single-phase liquid.
Suction	Vapour removal through porous surface.	For evaporation.
Jet Impingement	Force single phase liquid onto surface.	Mainly for single-phase. Can result in Evaporation.
Electrohydrodynamics	Electric fields to create secondary flow or redistribute the phases in a two-phase flow.	Single or two-phase dielectric flows.

both heat transfer and pressure drop available by varying the external input power into the technique and also because many of the active techniques can also be implemented into systems with passive methods already in place.

A review of the active enhancement methods in Table 1.1 (b) shows that the electrohydrodynamic (EHD) technique, which uses electric fields to enhance the heat transfer potential of the fluid, is an attractive augmentation method as it is applicable in single-phase flows, two-phase flows undergoing condensation or evaporation and can be used in conjunction with other traditional passive techniques. The wide range of applicability is much greater than other methods, which may be restricted to either single-phase or two-phase flows or for certain modes of heat transfer. In addition, the EHD technique is relatively simple in design, requiring no moving mechanical parts and heat transfer and pressure drop characteristics can be either controlled or enhanced. The control of the heat transfer is as simple as varying the input voltage, which effectively changes the strength of the electric fields and the electric body force influencing the flow field. Additionally, finer control measures can be achieved using different electrical waveforms (DC, AC or pulse) and by tuning the waveform parameters. The EHD technique is a dynamic method that has the ability to adapt to various system demands unlike conventional heat transfer augmentation techniques.

1.2 Electrohydrodynamic Heat Transfer Research

Electrohydrodynamics is the study of the interaction between electric fields and an electrically non-conducting (dielectric) fluid medium and has been a field of immense interest to researchers for its potential in heat transfer applications. This field of research has been studied for over 70 years, with the earlier work focusing on the EHD effect on single-phase flows and more recently, the focus has shifted on the EHD effect on two-phase flows [Laohalertdecha et al. (2007)]. The shift in EHD research from single-phase to two-phase flows is due to the much higher (an order of magnitude) heat transfer coefficients for a similar heat transfer surface area and mass flux.

EHD has been proven to be capable of inducing secondary motions and in two-phase flows, manipulating the flow distribution when applied to a dielectric fluid [Panofsky and Phillips (1962), Chang and Watson (1994), Yabe et al. (1996) and Cotton et al. (2005)]. The coupling between the electric fields to a dielectric fluid flow results in electric body forces, which are responsible for the additional secondary motions. The effect of this flow manipulation is the increase in the bulk mixing within the fluid and the enhancement of the heat transfer mechanisms (for both boiling and condensation in two-phase heat flows) at the heat transfer surfaces, both of which can have a significant impact on increasing/controlling the heat transfer in a heat exchanger. A detailed summary of EHD heat transfer research in both single-phase and two-phase flows is presented in detail in Chapter 3.

A review of the heat transfer research presented in Chapter 3 shows that the mechanisms for the enhancement of heat transfer due to EHD is the convection of charge in the medium, which increases the bulk mixing and destabilizes the thermal boundary layer, and additionally in two-phase flows, the redistribution of the liquid and vapour phases in the channel and an increase in the interfacial area due to the EHD forces. The influence of flow redistribution in a two-phase flow is that the thermal boundary layer can also be destabilized and the heat transfer performance for a condensation or evaporation process is highly dependent on the phase in contact with the heat transfer surface. For a condensation process, liquid in contact with the heat transfer surface inhibits the heat transfer performance because the liquid acts as a thermal resistance to the condensation of the vapour phase and alternatively for an evaporation process the vapour will act as a thermal resistance to the evaporation of the liquid phase. Therefore the effect of EHD on the flow redistribution plays an important role in the heat transfer enhancement and as discussed in Chapter 3, different flow patterns can be observed for different applied voltage waveforms. The various flow patterns can be classified as steady state or transient flow patterns. Typical steady state EHD flow patterns observed are an inverse annular flow pattern [Cotton et al. (2003)] or an oscillatory entrained droplet flow pattern [Cotton et al. (2001)] and typical transient flow patterns consist of unique flow structures that are described as twisted liquid cones [Sadek (2009)]. For the transient flow patterns, they were observed during the initial stages of a step input of high voltage and were not present during a continuous application of EHD. The transient flow patterns are postulated to result in the highest heat transfer if they can be sustained [Sadek (2009)], however, the only investigations performed to attempt to sustain the transient flow patterns have been a preliminary analysis by Sadek (2009), who investigated the various time scales on the development and decay of the structures. The primary focus of the research in this thesis is to further evaluate the mechanisms for the development of the various transient EHD flow structures and to devise a means to sustain the structures in a steady state flow pattern. As heat transfer and pressure drop are closely linked to the flow pattern, the ability to create various flow patterns such as an inverse annular, oscillatory entrained droplet and twisted liquid cone flow patterns will allow for a fine control of the heat transfer and pressure drop.

1.3 Research Objectives

The main objectives of this research are to investigate the EHD phenomenon on a dielectric fluid flow and to determine the potential to sustain EHD specific transient flow patterns in two-phase applications. In past two-phase EHD research, various high voltage waveforms were applied to measure the effect on heat transfer and pressure drop and various steady state and transient EHD flow structures were observed as a result of these waveforms. The approach in this research is to identify all the various EHD flow structures that may be developed using high voltage waveforms, determine a means to sustain the transient flow structures during steady state, and then determine the resulting effect of the flow patterns consisting of these structures on heat transfer and pressure drop. In this investigation, the effect of EHD in both single-phase and two-phase flows is explored.

In the single-phase experiments, high voltage waveforms will be applied to a flow of liquid to investigate the effect of the liquid secondary motions on the enhancement of heat transfer and the mechanisms of charge injection in the test section. Single-phase experiments are performed because factors such as flow redistribution, which must be accounted for in two-phase systems, may be neglected. The specific objectives of the single-phase studies include

i. To determine the mechanisms responsible for heat transfer enhancement.

ii. To investigate the effect of continuous and pulse high voltage waveforms on heat transfer enhancement.

iii. To investigate the significance of voltage polarity on heat transfer enhancement.

iv. To elicit the method of charge injection in the configuration investigated.

An understanding of the mechanisms investigated in the specific objectives of the single-phase studies will provide insight into the determination of a means to sustain the transient two-phase flow structures and to understand mechanisms that may be responsible for the flow redistribution.

The focus of the two-phase flow studies includes sustaining the transient flow structures and evaluating the condensation heat transfer and pressure drop performance. The specific objectives include

i. Identifying the various EHD flow structures that may be produced.

ii. To determine the specific high voltage waveforms required for production and sustainability of the various EHD flow structures.

iii. To evaluate the condensation heat transfer and pressure drop performance of the flow patterns using the specific waveforms.

iv. To identify the mechanisms resulting in the heat transfer and pressure drop performance.

Chapter 2 – Background

2.1 Study of Electrohydrodynamics

EHD is an interdisciplinary subject and a strong foundation in the fundamentals of electrostatics, two-phase flows and heat transfer is a necessity in order to study and understand the EHD phenomena. In this chapter, the theory relevant to EHD from each of the various disciplines is provided and discussed and many of these theories will be used in the discussion in later chapters.

2.2 Electrostatics

The electrostatic definitions and equations, sourced from [Jonassen (1998), Crowley (1995), Singh (1995) and Castellanos (1998)], relevant to an EHD flow are provided in this section.

2.2.1 Electric Field

An electric field is a region in which any electric charge within the field will experience an electric force. The electric force, $\bar{F}_E$, is proportional to the charge itself and the electric field strength is given as, $\bar{E}$.

$$\bar{E} = {}^{\bar{F}_E}\!/_{q} \quad \text{or} \quad \bar{F}_E = q \cdot \bar{E} \tag{2.1}$$

For a point charge, q, the electric field strength of a point P at a distance, L, can be determined by the following equation

$$\bar{E} = \frac{q}{4\pi\varepsilon_o L^2}\bar{n} \tag{2.2}$$

where $\bar{n}$ is a unit vector in the direction towards point P.

2.2.2 Gauss's Law

Electric flux is given as the flux of the electric field, $\bar{E}$, through a surface, S, and can be described as

$$\phi_E = \int_S \bar{E} \cdot dS \tag{2.3}$$

If the surface, S, is closed (Gaussian surface), the electric flux can be rearranged as

$$\int_{CS} \bar{E} \cdot d\bar{S} = \frac{q}{\varepsilon_o} \tag{2.4}$$

In Eq. (2.4), q is the sum of all charges within the closed surface and the electric field within the conductor is zero. Here Gauss's Law gives the relation between the electric field strength and the charge density. Gauss's Law may also be written to relate the charge density, q, to the dielectric displacement, $\bar{D}$. The dielectric displacement is given as

$$\bar{D} = \varepsilon\bar{E} \tag{2.5}$$

where ε is the dielectric permittivity (or permittivity of the material). The dielectric permittivity is related to the permittivity in free space by the relative permittivity (or dielectric constant) of the material.

$$\varepsilon = \varepsilon_r \varepsilon_o \tag{2.6}$$

The dielectric displacement gives the degree of polarization in the medium due to an electric field. Gauss's Law written in terms of the dielectric displacement is as follows

$$\int_{CS} \bar{D} \cdot d\bar{S} = q \tag{2.7}$$

2.2.3 Electric Potential

An electric field, $\bar{E}$, will perform work in moving a charge, q, placed within the field. For example, the work performed by the electric field in moving a charge from points A to B can be determined as

$$W_{AB} = -q \int_A^B \bar{E} \cdot d\bar{l} \tag{2.8}$$

where $\bar{l}$ is the distance between the points of interest. The electric field is conservative and can be written as a function of the potential difference (or voltage difference).

$$W_{AB} = q[V_B - V_A] \tag{2.9}$$

$$V_B - V_A = -\int_A^B \bar{E} \cdot d\bar{l} \tag{2.10}$$

The potential difference represents the integral of the electric field strength between points A and B. Consequently, the electric field can be determined if the potential difference is known. In this research, the EHD effect is established by applying high voltage to a rod electrode placed concentrically inside a grounded tube. The electric field strength and potential difference for this configuration can be determined by first assuming that the charge on the inner rod is uniform to get the relation

$$q = \lambda_c L \tag{2.11}$$

where λ_c is the charge density per unit length and L is the length of the rod. The electric field strength can then be determined by substituting Eq. (2.11) into Gauss's Law (Eq. (2.4)) and then integrating to get

$$\bar{E} = \frac{\lambda_c}{2\pi\varepsilon_o r} \tag{2.12}$$

The potential difference between the inner rod and outer tube can now be solved by substituting Eq. (2.12) into (2.10) to get

$$V_B - V_A = \frac{\lambda_c}{2\pi\varepsilon_o} ln\left(\frac{r_B}{r_A}\right) \tag{2.13}$$

Substituting Eq. (2.13) into (2.12), the electric field strength can now be defined in terms of the potential difference as

$$\bar{E} = \frac{V_B - V_A}{r ln\left({}^{r_B}/_{r_A}\right)} \tag{2.14}$$

Eq. (2.14) shows that the electric field strength will be strongest near the inner rod and decrease with radius.

2.2.4 Electric Current

Conduction electric current is the transport of charges due to an electric field and can be expressed as a function of the current density, $\bar{J}$, which is a measure of the amount of charge that has passed through a unit area per unit time. The current density is described using the following charge transport equation for a fluid

$$\bar{J} = \rho_c \mu_e \bar{E} - D_i \nabla \rho_c + \rho_c \bar{u} \tag{2.15}$$

The three terms on the right side of Eq. (2.15) are the movement of the ions under the influence of an electric field, the diffusion of charge and the convection of the charges due to the velocity field, respectively. A fluid can be classified as either being ohmic or non-ohmic depending on the behaviour of the charge transport with applied voltage. If the charge density varies linearly with the applied potential, the fluid is classified as being ohmic and if it varies non-linearly, the fluid is classified as non-ohmic. An ohmic or non-ohmic behaviour is not an intrinsic property and one of the main deciding factors on the charge transport behaviour is the electric field intensity. For low electric field strengths, the behaviour of most fluids will be ohmic while at high electric fields, the material is non-ohmic because of the addition of charge injection.

In addition to the conduction current, which is the transport of charge, there exist another current known as the dielectric displacement current (or simply displacement current). The displacement current is due to the formation of electric dipoles. When an electric field is applied to a dielectric medium, the molecules become polarized because the positive and negative charges slightly separate. This slight movement due to polarization represents the displacement current, which is a charge displacement without charge transport and will be present for any changes in the electric field. Changes in the electric field strength can be a result of applying a DC voltage in pulses or for an AC voltage. The displacement current density may be determined as follows

$$\bar{J_D} = \varepsilon_o \frac{d\bar{E}}{dt} = \frac{d\bar{D}}{dt} \tag{2.16}$$

2.2.5 Charge Injection

In dielectric liquids, the presence of charge is due to charge injection in the regions of high electric field and is generally electrochemical in nature, which differs from gases where the charges would arise due to a corona discharge [Atten and Castellanos (1995)]. There are two generally accepted mechanisms on the origins of free charges [Coelho (1979) and Fujino (1989)]. The first is the charges arise due to the variation in the conductivity due to thermal variations (temperature gradients) and the charge produced is intrinsic to the system. The other mechanism for the presence of charge is due to charge injection from an electrode, where the charges are now extrinsic to the system. The charges due to the first mechanism are known as the conductivity component and the charges due to the second are known as the mobility component.

The current flux is dependent on the electrical conductivity and electric field strength as shown in Eq. (2.15). The electrical conductivity is a function of the temperature and therefore any temperature gradients will result in the production of charge due to the thermal excitation of the charge carriers. For an injection process, the mechanisms of charge injection in a dielectric are still not well understood because the dielectric fluid affects two important charge injection parameters, the work function and the potential barrier, in a means that is not yet understood [Coelho, 1979 and Denat, 1988]. The work function is the minimum energy needed to remove an electron (from the Fermi level) from a solid electrode to a point immediately outside the solid surface and the potential barrier is the electrostatic forces restraining the charges. A lowering of the potential barrier reduces the electric potential required for injection. There have been various models developed to explain the charge injection process; however they consider a vacuum in place of a dielectric material [Coelho (1979)]. Two of the most common charge injection models are i) Schottky injection and ii) Fowler-Nordheim injection [Coelho (1979), Kuffel et al. (2000) and Shrimpton (2009)].

i) Schottky Injection

Schottky injection is classified as a field enhanced thermionic emission process, where the injection occurs from a metal cathode due to lowering of the potential barrier by high electric field strengths. This process is shown in Figure 2.1. The electric field of an electron that leaves the metal surface in Figure 2.1 can be approximated using Coulomb's law to give

$$\bar{F} = \frac{-e^2}{4\pi\varepsilon_o(2x_L)^2} \tag{2.17}$$

where the electron is a distance x_L from the metal electrode and there exists an image of charge of +e inside the electrode at a distance of $-x_L$. The potential energy can then be determined for any distance by integrating Eq. (2.17) from x to ∞ to give

$$\bar{W}_a = \frac{-e^2}{16\pi\varepsilon_o x_L} \tag{2.18}$$

This potential energy is the work function shown in Figure 2.1 in the absence of an external electric field. The energy of an external electric field on the electron can be determined as

$$\bar{W}_E = -eEx_L \tag{2.19}$$

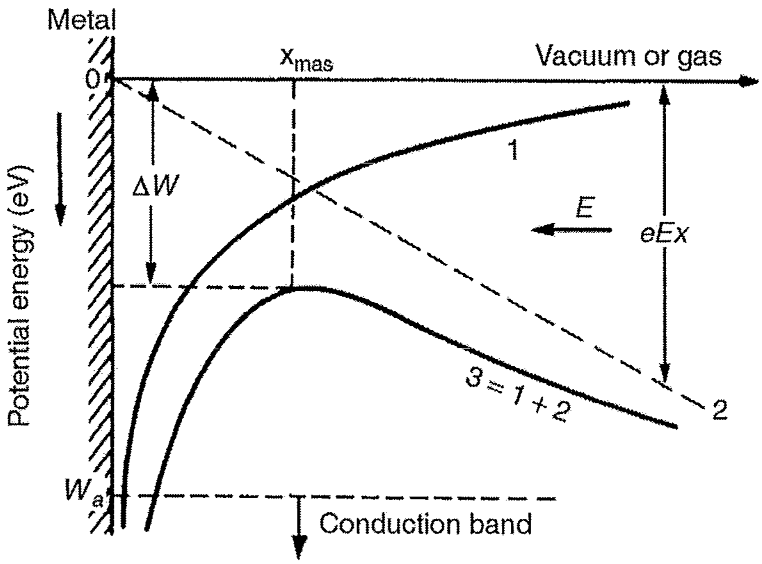

Figure 2.1 – Decrease in the work function due to an external electric field. 1 - Work function with no field, 2 – Energy due to field and 3 – Total energy.
[Kuffel et al. (2000)]

The total energy can then be determined by summing up Eq. (2.18) and (2.19) to give

$$\overline{W} = \overline{W}_a + \overline{W}_E = \frac{-e^2}{16\pi\varepsilon_o x_L} - eEx_L \tag{2.20}$$

The maximum decrease in work function can be determined by finding the inflection point at distance x_m by differentiating Eq. (2.20) as follows

$$\frac{d\overline{W}}{dx} = \frac{e^2}{16\pi\varepsilon_o {x_m}^2} - eE = 0$$

$$x_m = \sqrt{\frac{e}{16\pi\varepsilon_o E}} \tag{2.21}$$

Therefore, a new effective work function for charge injection in the presence of an external field can be determined by substituting Eq. (2.21) into (2.20) to give

$$\overline{W}_{eff} = \overline{W}_a - \sqrt{\frac{e^3 E}{4\pi\varepsilon_o}} \tag{2.22}$$

Eq. (2.22) shows the enhancement of charge injection by using an electric field to lower the work function. This method of charge injection is considered valid for electric field strengths less than 10^8V/m.

i) Fowler-Nordheim (Tunnel) Injection

Tunnel injection predicts that the electrons in the electrode can pass through the potential barrier if the wavelength of the probability wave associated with the electrons is larger than the thickness of the barrier. The wavelength of an electron hitting the surface of the electrode can be predicted as

$$\lambda = \frac{h}{\sqrt{2m_e \Phi}} \tag{2.23}$$

where h is Plank's constant, m_e is the mass of the electron and Φ is the Fermi energy. Injection of charges will occur if this wavelength is larger than the thickness of the potential barrier, which is given as

$$x_F = \frac{V}{\overline{E}} \tag{2.24}$$

This method of injection is not believed to be responsible for charge injection in dielectrics because the electric fields required for the tunneling process is in the order of 10^8-10^9V/m, which is much higher than the electric fields observed in dielectric applications [Shrimpton (2009)].

2.3 Fluid Mechanics and Heat Transfer

2.3.1 Single-Phase Heat Transfer

In convective single-phase flows, enhancement of heat transfer can be accomplished by increasing the bulk mixing within the fluid and/or disrupting the thermal boundary layer. The effect of the bulk mixing and or disruption of the thermal boundary layer on the heat transfer performance can be seen in Figure 2.2, where a transition from a laminar flow to turbulent flow results in a sharp increase in heat transfer.

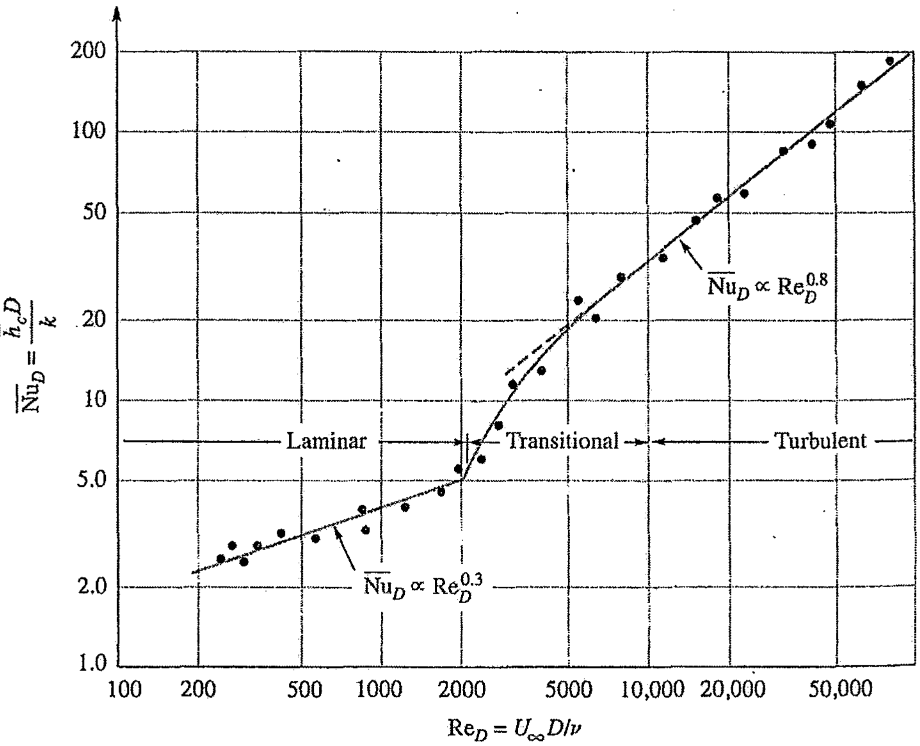

Figure 2.2 – Nusselt number versus Reynolds number for air flowing in a long heated pipe [Kreith and Bohn (2001)]

EHD can be used to promote secondary motions in single phase flows (i.e. pure liquid or pure vapour) due to the electric body forces, which is later discussed in Chapter 3. These motions result in the generation of turbulence [Yabe et al. (1996)] and therefore it is expected that EHD in single-phase flows will exhibit the same considerable increase in heat transfer as a promotion from a laminar flow to turbulent flow.

2.3.2 Two-Phase Flows

Two-phase flows (i.e. liquid-vapour flows) are ideal in the design of heat exchangers because the principle mode of heat transfer is through a phase change of the working fluid. Phase change heat transfer in liquid-vapour flows is more effective than single phase flows because it utilizes the latent heat of evaporation in exchanging heat. Two-phase flows are a difficult topic of study because of the need to account for a variety of important flow parameters and characteristics. These difficulties are outlined in [Levy (1999)] and some of the major difficulties are

- *A large number of gas-liquid interfaces exist in the flow, where at each interface momentum, energy and mass transfer will occur. These interfaces are difficult to specify or predict.*

- *The interaction of the two phases can result in a large variety of different flow patterns. These patterns may vary over time. For example, a stratified wavy flow (see Figure 2.3(iv)) will have different wave amplitudes over time and in a slug flow (see Figure 2.3(v)), the frequency of slugs vary.*

Due to difficulties in two-phase flow research, a phenomenological approach is commonly employed to describe two-phase flows [Castellanos (1998) and Hewitt (1981)]. Common research techniques in this approach are [Castellanos (1998)]:

- *Identification of the flow patterns (or flow regimes)*
- *Observation of the detailed phenomena and the performance of appropriate measurements such as temperatures, pressures, void fractions, quality, flow rates or velocities etc.*
- *Construction of physical models with theoretical links to describe the local phenomena*
- *Integration of the local models to achieve a complete system description*
- *Use of the integrated model for prediction and design*

This approach is utilized in describing the EHD phenomenon presented in this research.

2.3.2.1 Two-Phase Flow Patterns

Specific flow regimes are observed for two-phase liquid-vapour flows based on the flow characteristics, such as the volume fraction of liquid and vapour, velocity of each of the phases, the flow orientation, etc. The general agreed upon horizontal flow regime classifications that may exist in a two phase flow in the absence of an electric field are described below and shown in Figure 2.3 [Collier and Thome (1994), Castellanos (1998) and Carey (2008)].

Bubbly Flow

- Classified according to small vapour bubbles in an otherwise liquid flow. Bubbles travel in the upper half of the tube due to differences in phase densities.

Plug Flow (Intermittent Flow)

- In this flow regime, large bubbles are present and are separated by slugs of liquid. Bubbles are in the upper half of the tube.

Stratified Flow (or Stratified Smooth Flow)

- Classified according to liquid at the bottom and vapour at top. Only occurs in horizontal flows where the phases are separated by gravity.

Stratified Wavy Flow

- Similar to the stratified smooth flow except the liquid-vapour interface is wavy due to a higher vapour velocity. This results in a higher interfacial shear force. Only occurs in horizontal flows where the phases are separated by gravity.

Slug Flow (Intermittent Flow)

- Further increases in the vapour velocity in a stratified wavy flow results in an instability in the waves at the liquid-vapour interface and results in the development of a slug of liquid bridging the tube walls. A residual is left on the upper wall due to the wetting by the slug and this liquid eventually drains back into the fluid bulk.

Annular Flow

- A further increase in the vapour velocity in slug flow will result in an annular flow. Classified according to the wetting of the walls by a thin film and high velocity vapour passing through the center. May have liquid droplets entrained in the vapour core. This flow pattern occurs at high mass flux where the fluid inertia dominates the gravitational forces.

Mist and Droplet Flow

- Classified according to small liquid drops or mist in an otherwise gas flow.

Numerous flow pattern maps have been developed to predict the transition between the various two-phase flow patterns in a horizontal tube geometry. Maps have been developed by Baker (1954), Taitel and Dukler (1976), Hashizume (1983) and Steiner (1993) to predict flow pattern transitions under adiabatic conditions. For diabatic conditions, maps to predict flow pattern transitions under condensation have been developed by Breber (1988), Tandon et al. (1982), Cavallini et al. (2002) and El Hajal et al. (2003) and for evaporation, a transition map has been developed by Kattan et al. (1998). The flow regime map shown in Figure 2.4 [Thome and El Hajal (2002)] predicts the flow pattern for specific flow parameters and using refrigerant R-134a as the working fluid. In this figure, transition lines from the various flow patterns are shown based on the mass flux and vapour quality for both evaporation and condensation.

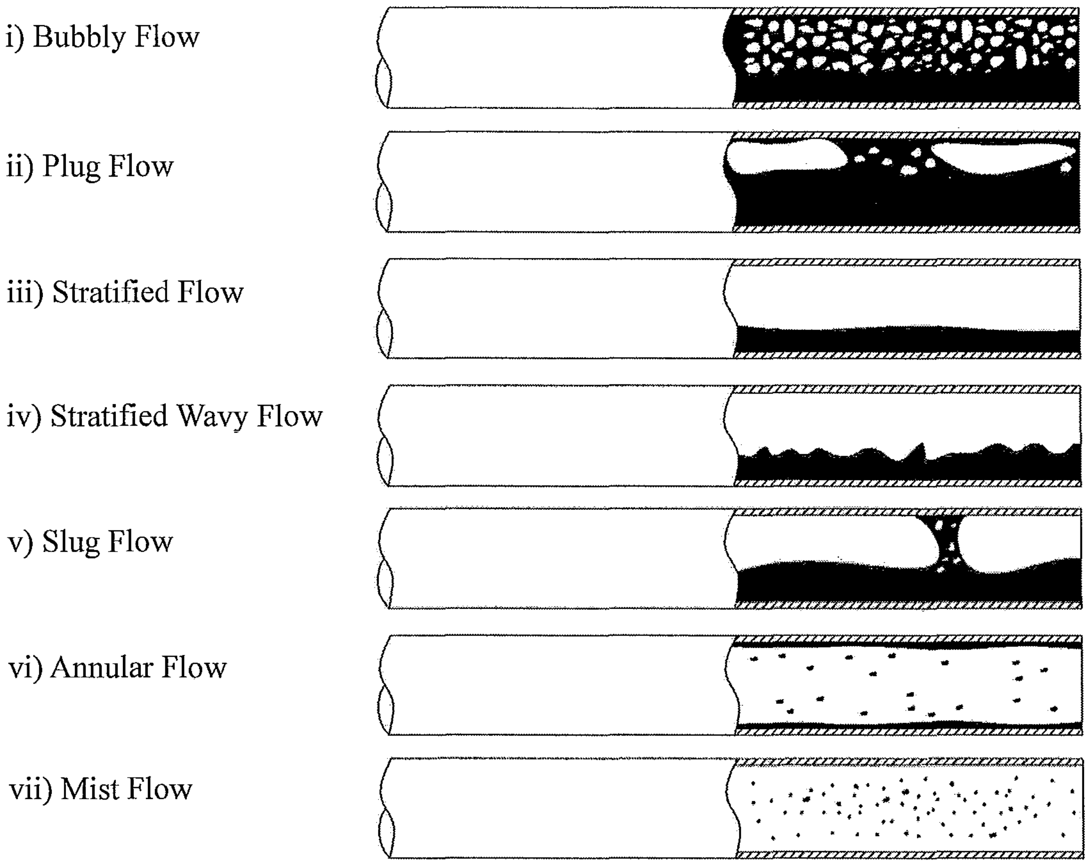

Figure 2.3 – Two-phase flow patterns in a horizontal tube.

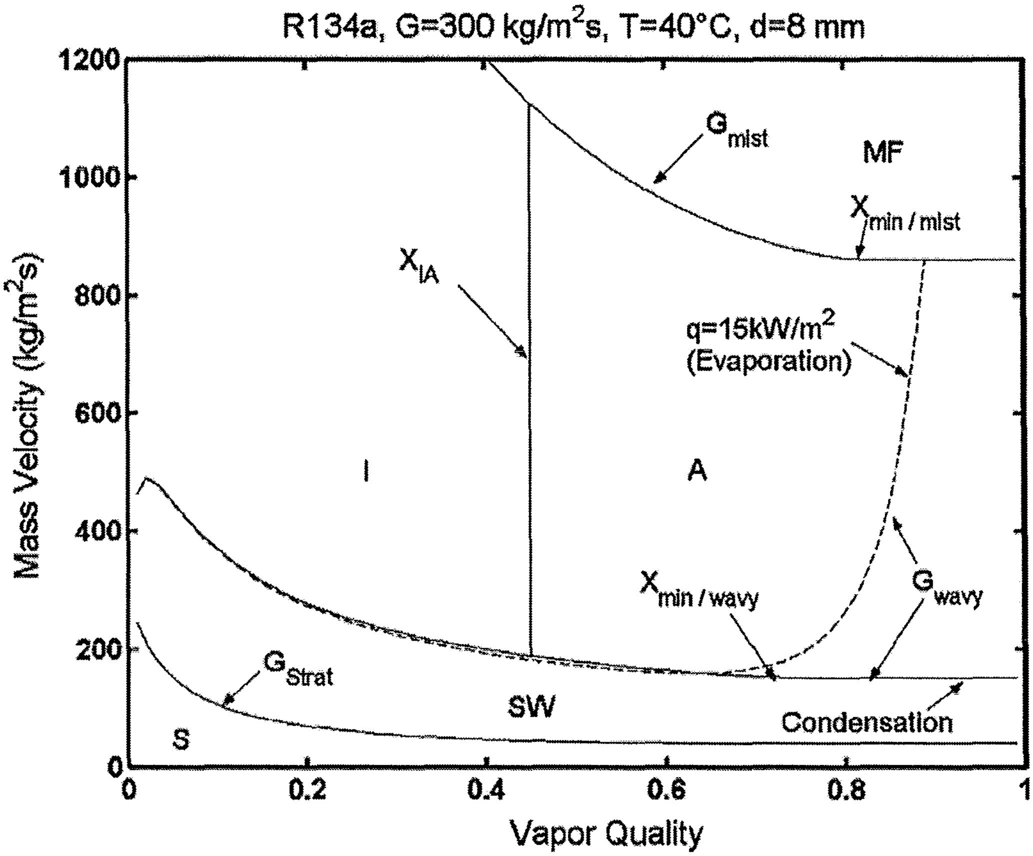

Figure 2.4 – R-134a flow pattern transition map for both condensation and evaporation processes where S – Stratified, SW – Stratified wavy, I – Intermittent (Slug and Plug), A – Annular and MF – Mist flow.

2.3.2.2 Two-Phase Condensation Heat Transfer

The heat transfer characteristics of a two-phase flow are strongly related to the flow pattern because the heat transfer mechanism is dependent on the phase in contact with the heat transfer surface. For a condensation process, the heat transfer mechanisms depend on whether the flow is gravity driven (i.e. stratified, stratified wavy and slug flows) or shear driven (i.e. annular flows) [Dobson and Chato (1998)]. For the different types of flows, correlations are developed to determine the heat transfer in terms of the Nusselt number, which is defined as

$$Nu = {}^{\bar{h}D_h}\!/_{k} \tag{2.25}$$

For tube geometries, the hydraulic diameter, D_h, is taken as the inner diameter of the tube.

- **Gravity Driven Flows**

  i. *Stratified Smooth Flow*

In this flow, the vapour velocity is low and the vapour shear forces can be neglected. The distribution of vapour at the upper portion of the tube and liquid at the bottom portion of the tube result in two very different heat transfer coefficients. The condensation heat transfer mechanism at the top of the tube is film condensation. In this mode of heat transfer, vapour condenses at the surface and a liquid film is produced. This liquid film grows in thickness as it flows down the circumference of the tube walls before collecting at the bottom of the tube. The film flows down the tube because the gravitational forces are stronger than the shear forces in this type of flow and the dominant mode of heat transfer at the film is by conduction through the liquid film. On the bottom of the tube, convective condensation occurs where the heat transfer is mainly through convection between the liquid layer and neighbouring vapour. For stratified flows, which occurs at low mass flux, the heat transfer from the lower liquid stratum is found to be negligible compared to the regions in the tube undergoing film condensation because of the thickness of the liquid stratum [Dobson and Chato (1998)]. The heat transfer for a stratified flow can be determined using correlations developed by Chato (1962) or Jasker and Kosky (1976). The correlation developed by Chato (1962) is given as

$$Nu = 0.555\left[\frac{\rho_l(\rho_l-\rho_v)gh_{lv}(1+0.68Ja_l)D^3}{k_l\mu_l(T_{sat}-T_s)}\right]^{1/4} \tag{2.26}$$

where
$$Ja_l = \frac{c_{p_l}(T_{sat}-T_S)}{h_{lv}} \tag{2.27}$$

and the correlation developed by Jasker and Kosky (1976), which incorporates the void fraction, is given as

$$Nu = 0.728\alpha^{3/4}\left[\frac{\rho_l(\rho_l-\rho_v)gh_{lv}(1+0.68Ja_l)D^3}{k_l\mu_l(T_{sat}-T_s)}\right]^{1/4} \tag{2.28}$$

The recommended void fraction correlation [Zivi (1964)] to be used in Eq. (2.28) is given as

$$\alpha = \left[1+\frac{1-x}{x}\left(\frac{\rho_v}{\rho_l}\right)^{2/3}\right]^{-1} \tag{2.29}$$

A comparison of the two correlations shows that the Jasker and Kosky correlation overpredicts Nu for qualities greater than 0.2. In both correlations presented by Chato and Jasker and Kosky, the conduction heat transfer is assumed negligible in the liquid stratum. This assumption is considered valid in a stratified flow but not in a stratified wavy or slug flow where the vapour and liquid velocity is greater and the convective heat transfer from the liquid stratum will become more significant.

ii. Stratified Smooth Flow

The heat transfer in both stratified wavy and slug flows is similar to that of a stratified smooth flow except that the vapour velocity is higher and thus the vapour shear forces are significant in the heat transfer process. This flow regime can be classified as a viscous-turbulent flow because the vapour velocity is turbulent and the liquid velocity is still laminar. Correlations to determine the heat transfer was developed by Rosson and Myers (1965), and they determined that the heat transfer in these types of flow can be characterized using two Nusselt correlations, one for film condensation which occurs at the top of the tube and one for convective condensation which occurs at the bottom of the tube. The correlation is given as

$$Nu = \beta Nu_{Top} + (1+\beta)Nu_{Bot} \tag{2.30}$$

where

$$\beta = Re_{vs}^{0.1} \qquad \text{if} \qquad \frac{Re_{vs}^{0.1} Re_{ls}^{0.5}}{Ga} < 6.4 \times 10-5 \tag{2.31}$$

$$\beta = \frac{1.74 \times 10^{-5} Ga}{\sqrt{Re_{vs} Re_{ls}}} \qquad \text{if} \qquad \frac{Re_{vs}^{0.1} Re_{ls}^{0.5}}{Ga} > 6.4 \times 10-5 \tag{2.32}$$

The Nusselt number correlations for the top and bottom regions of the tube are given as

$$Nu_{Top} = 0.31 Re_{vs}^{0.12} \left[\frac{\rho_l(\rho_l - \rho_v) g h_{lv} (1 + 0.68 Ja_l) D^3}{k_l \mu_l (T_{sat} - T_s)}\right]^{1/4} \tag{2.33}$$

$$Nu_{Bot} = \frac{\phi_{l,lt}\sqrt{8Re_{ls}}}{5\left[1 + \frac{ln(1+5Pr_l)}{Pr_l}\right]} \tag{2.34}$$

where

$$\phi_{l,lt} = \sqrt{1 + \frac{1}{X_{lt}} + \frac{12}{{X_{lt}}^2}} \tag{2.35}$$

In Eq. (2.35), X_{lt} is the Lockhart-Martinelli parameter for a laminar-turbulent flow of liquid-vapour. The Lockhart-Martinelli parameter is defined as

$$X = \left[\frac{\left({dP}/{dz}\right)_l}{\left({dP}/{dz}\right)_v}\right]^{1/2} \tag{2.36}$$

The Lockhart-Martinelli parameter is based on the frictional pressure drops of the liquid and vapour phases and details determining the pressure drop can be found in Section 2.3.2.3.

- **Shear Driven Flows**

  i. *Annular Flow*

In an annular flow, the high vapour velocity results in a more uniform distribution of liquid around the circumference and the heat transfer characteristics differs from that of a gravity driven flow. The factors affecting the rate of heat transfer is the film thickness around the tube walls, which acts as a thermal resistance to heat transfer. This liquid thickness, along with the thermal conductivity and velocity of the liquid, determines the temperature difference across the film and therefore the rate of heat transfer in the condensation process.

Three methods of predicting the heat transfer of an annular flow will be discussed in this section, which are a) two-phase multiplier models, b) shear-based models and c) boundary-layer models.

a) Two-Phase Multiplier Models

This model assumes that the heat transfer performance of an annular flow can be determined using a single-phase heat transfer correlation with the addition of a multiplier to correct for the differences in the single-phase and two-phase heat transfer. The single-phase correlation generally modified is the Dittus-Boelter correlation, which is given as

$$Nu = 0.023 Re_{ls}^{0.8} Pr_l^{m} F\left(x, \frac{\rho_l}{\rho_v}, \frac{\mu_l}{\mu_v}, Fr_l\right) \tag{2.37}$$

Where F is the two-phase multiplier and m takes a value of 0.3 for condensation and 0.4 for evaporation. The two-phase multiplier may be determined using correlations by Shah (1979) or Cavallini and Zecchin (1974).

b) Shear-Based Models

This model for predicting condensation heat transfer in an annular flow was first developed by Carpenter and Colburn (1951) and assumes that the thermal resistance in the liquid layer in an annular flow is entirely in the laminar sublayer and that the wall shear is due to friction, acceleration and gravity. The model by Carpenter and Colburn was improved by Soliman et al. (1968), who corrected an error in the computation of the shear due to acceleration and also determined new coefficients in the coefficients using sets of experimental data from other researchers. The correlation by Soliman et al. is given as

$$Nu = 0.036 Re_l^{0.8} Pr_l^{0.65} \left(\frac{\rho_l}{\rho_v}\right)^{0.5} \times \sqrt{\frac{2(0.046)x^2}{{Re_v}^{0.2}} {\phi_v}^2 + Bo \sum_{n=1}^{5} a_n \left(\frac{\rho_v}{\rho_l}\right)^{n/3}} \tag{2.38}$$

where

$$a_1 = x(2-\gamma) - 1$$

$$a_2 = 2(1-x)$$

$$a_3 = 2(\gamma - 1)(x - 1)$$

$$a_4 = \frac{1}{x} - 3 + 2x$$

$$a_5 = \gamma\left[2 - \frac{1}{x} - x\right]$$

For a turbulent flow, $\gamma = 1.25$. A comparison of this correlation with experimental data shows that the trends predicted are correct, however the deviations were large. No statistical information on the standard deviations was provided by the authors.

c) Boundary-Layer Models

This model is similar to the shear-based model except that the entire film thickness is considered as a thermal resistance. Correlations by Dukler (1960), Kosky and Staub (1971), Azer et al. (1972) and Traviss et al. (1973) have been proposed based on this model. In this section, only the correlation by Traviss et al. is presented and is given as

$$Nu = \frac{F(X_{tt})Pr_l Re_l^{0.9}}{F_2} \tag{2.39}$$

where

$$F(X_{tt}) = 0.15\left[\frac{1}{X_{tt}} + 2.85X_{tt}^{-0.476}\right] \tag{2.40}$$

and

$$F_2 = 0.707 Pr_l Re_l^{0.9} \qquad \text{if} \quad Re_l < 50$$

$$F_2 = 5Pr_l + 5\ln\left[1 + Pr_l\left(0.09636 Re_l^{0.585} - 1\right)\right] \qquad \text{if} \quad 50 < Re_l < 1125$$

$$F_2 = 5Pr_l + 5\ln[1 + 5Pr_l] + 2.5ln\left(0.00313 Re_l^{0.812}\right) \qquad \text{if} \quad Re_l > 1125$$

The correlation by Traviss et al. was found to be in good agreement with experimental results as the maximum deviation was within 7%.

2.3.2.3 Two-Phase Pressure Drop

In an internal two-phase flow there are many components that contribute to the overall pressure drop. These various components are the frictional, momentum and gravitational effects on pressure drop. The frictional component consists of the interfacial shear between the liquid and vapour phases and the shear between the liquid and vapour phases with the channel walls, the momentum component is due to the changes in the momentum by the acceleration/deceleration of the phases or by a mass transfer between the phases (i.e. condensation or evaporation process) and the gravitational component is mainly considered in a vertical flow where the gravitational force will act against an upward flow. The governing equation for the pressure gradient is given as

$$-\left(\frac{\partial P}{\partial z}\right) = -\left(\frac{\partial P}{\partial z}\right)_{fr} + [(1-\alpha)\rho_l + \alpha]gsin\theta + \frac{d}{dz}\left[\frac{G^2x^2}{\rho_v\alpha} + \frac{G^2(1-x)^2}{\rho_l(1-\alpha)}\right] \qquad (2.41)$$

The first term in the equation represents the frictional component to the pressure drop, the second term represents the gravitational component, where θ represents the angle of the channel inclined from the horizontal, and the third term represents the momentum change component. To evaluate the overall pressure gradient, the frictional pressure drop component is often modeled using a two phase multiplier approach. In this approach, the two-phase frictional pressure gradient is modeled as a function of the pressure gradient that would occur if only a single-phase liquid or vapour flowed through the channel and a two-phase multiplier is used to correct for the differences due to this simplification. The three commonly used two-phase multiplier models are given as

$$-\left(\frac{\partial P}{\partial z}\right)_{fr} = -\phi_l^2\left(\frac{dP}{dz}\right)_l = -\phi_{lo}^2\left(\frac{dP}{dz}\right)_{lo} = -\phi_v^2\left(\frac{dP}{dz}\right)_v = \phi_{vo}^2\left(\frac{dP}{dz}\right)_{vo} \qquad (2.42)$$

In Eq. (2.42), ϕ is the two-phase flow multiplier and the subscripts denote the following conditions:

l - Pressure drop of a flow of only liquid through a channel with the mass flow rate of $\dot{m}_l = G(1-x)A$

lo - Pressure drop of a flow of only liquid through a channel with the same mass flow rate as the two-phase flow, $\dot{m}_{lo} = GA$

v - Pressure drop of a flow of only vapour through a channel with a mass flow rate of $\dot{m}_v = GxA$

vo - Pressure drop of a flow of only vapour through a channel with the same mass flow rate as the two-phase flow, $\dot{m}_{lo} = GA$

The single-phase pressure gradients used in the two-phase multiplier models may be determined using the following general single-phase friction factor model

$$-\left(\frac{\partial P}{\partial z}\right)_x = \frac{2f_x\dot{m}_x^2}{\rho_x A^2 D_h} \tag{2.43}$$

The two-phase flow multiplier used in the model may be determined as a function of the Martinelli parameter and is given as [Chisholm and Laird (1958)]

$$\phi_l = \left(1 + \frac{C}{X} + \frac{1}{X^2}\right)^{1/2} \tag{2.44}$$

$$\phi_v = (1 + CX + X^2)^{1/2} \tag{2.45}$$

The parameter C in Eq. (2.44) and (2.45) is dependent on if the liquid and vapour phases are laminar or turbulent, where Re = 2000 is considered the critical value for the transition. A list of the various values of C is given in Table 2.1. This correlation, which is based on the Martinelli parameter, was found to be in good agreement with experimental results for adiabatic two-phase flows in horizontal tubes [Lockhart and Martinelli (1949)].

Table 2.1 – Values of the parameter C for various flow conditions.

Liquid	Vapour	Parameter C
Turbulent	Turbulent	20
Viscous	Turbulent	12
Turbulent	Viscous	10
Viscous	Viscous	5

If the two-phase multiplier drop ϕ_{lo} is used to predict the pressure gradient, the parameter may be determined using the correlation by Friedel (1979), which is given as

$$\phi_{lo}^2 = C_{F1} + \frac{3.24C_{F2}}{Fr^{0.045}We^{0.035}} \tag{2.46}$$

where

$$C_{F1} = (1-x)^2 + x^2 \left(\frac{\rho_l}{\rho_v}\right)\left(\frac{f_{vo}}{f_{lo}}\right) \tag{2.47}$$

$$C_{F2} = x^{0.78}(1-x)^{0.24}\left(\frac{\rho_l}{\rho_v}\right)^{0.91}\left(\frac{\mu_v}{\mu_l}\right)^{0.19}\left(1-\frac{\mu_v}{\mu_l}\right)^{0.7} \tag{2.48}$$

$$Fr = \frac{G^2}{g D_h \rho_{tp}^2} \tag{2.49}$$

$$We = \frac{G^2 D_h}{\rho_{tp}^2 \sigma} \tag{2.50}$$

$$\rho_{tp} = \left(\frac{x}{\rho_v} + \frac{1-x}{\rho_l}\right)^{-1} \tag{2.51}$$

This correlation for predicting the pressure drop is recommended for flows where $\left(\frac{\mu_v}{\mu_l}\right) < 1000$ and the standard deviation of this correlation when matched with over 25000 experimental data points is approximately 30% [Carey (2008)].

Chapter 3 – Electrohydrodynamics

3.1 The Electrohydrodynamic Phenomenon

Electrohydrodynamics is the study of the interactions between electric fields and dielectric fluid flows and the effect on the hydrodynamics has been well documented in past research. For example, Faraday (1838) observed the violent movement of the dielectric fluid, turpentine, when subjected to an electric field. The fluid was observed to rise up the electrical wire before eventually darting off as jets. The liquid motions were later hypothesized by Gemant (1929) to be due to the movement of the space charges under the influence of an electric field. Advancements in the study of EHD have identified the various influences of an electric field on dielectric liquids, such as electroconvective eddies [Turnbull (1968), Lacroix et al. (1975) and Fujino et al. (1989)], liquid extraction [Yabe et al. (1982)] and on the physics describing these effects [Chang and Watson (1994)].

3.2 Fundamentals of Electrohydrodynamics

The conservation equations for a laminar flow with an applied electric field can be expressed as follows

i. Mass Conservation

$$\frac{\partial \rho}{\partial t} + \rho \nabla \cdot \bar{u} = 0 \tag{3.1}$$

ii. **Momentum Conservation**

$$\rho\frac{\partial\bar{u}}{\partial t}+\rho(\bar{u}\cdot\nabla)\bar{u}=-\rho\bar{g}\beta(T-T_0)-\nabla P+\bar{f}_{eB}+\mu\nabla^2\bar{u} \tag{3.2}$$

iii. **Energy Conservation**

$$\rho c_P\frac{\partial T}{\partial t}+\rho c_P\bar{u}\cdot\nabla T=k\nabla^2T+q_{eB}''' \tag{3.3}$$

The presence of an electric field has an influence on the momentum conversation and energy conservation equations. In the energy conservation equation there is an additional energy generation term q_{eB}''' and in the momentum conservation equation there is an additional electric body force, $\bar{f}_{eB}$, which influences the flow. The energy generation and electric body force term was first derived by Chu (1959), who considered the interactions of the free charge, electric dipole and magnetic dipole interactions on the energy and momentum of a fluid flow. For a dielectric fluid flow, the magnetic field components in the Chu's equations may be neglected because of the negligible current and the energy and electric body force equations can be simplified [Chang and Watson (1994) and Cotton (2000)]. The simplified energy generation term for a dielectric fluid may be expressed as

$$q_{eB}'''=\sigma_e E^2 \tag{3.4}$$

and the simplified electric body force equation may be expressed as

$$\bar{f}_{eB}=\rho_c\bar{E}-\frac{1}{2}E^2\nabla\varepsilon+\frac{1}{2}\nabla\left[E^2\left(\frac{\partial\varepsilon}{\partial\rho}\right)_T\right] \tag{3.5}$$

The energy generation term is the heat due to flow of charged particles (ohmic heating). However, this energy generation is often neglected and because the conductivity of typical dielectrics is between 10^{-10} to 10^{-16} S/m. For the present studies with R-134a, the maximum energy generation in the fluid was determined to be 2.1W, which is approximately 4% of the heat load in the test section.

The electric body force equation given in Eq. (3.5) is composed of three components. The first term is the electrophoretic force, which is the force of the electric field acting on the free charges. This free charge may be existing charges within the fluid or injected from the electrodes. The second term in the equation represents the dielectrophoretic force, a force that arises due to the spatial change in the electric field as a result of differences in the permittivity of the dielectric fluid medium. The difference in the permittivity can be attributed to the dielectric permittivity being inhomogenous within the medium or due to multiple phases in the system, as the permittivity differs for different phases. The result is the establishment of a non-uniform electric field in the domain, where the electric field strength acting on the medium is higher in the regions of lower permittivity. This results in a net force driving the dielectric medium towards regions of higher electric field strength (discussed in detail in Section 3.5.1). The third term in the electric body force equation is the electrostrictive term and is caused by the inhomogeneity in the fluid as a result of additives to the dielectric medium and/or differences in pressure/temperature in different regions within the medium. This results in gradients of polarization within the fluid that under an applied electric field may result in a distortion of the medium. Both the dielectrophoretic and electrostrictive forces are classified as polarization forces.

3.3 Dimensionless Analysis

In this section, dimensionless analyses are presented to determine the conditions when EHD will become significant in a fluid flow.

3.3.1 EHD and Masuda Number

The fluid momentum equation with EHD (Eq. (3.2) and (3.5)) is given as

$$\rho\frac{\partial\bar{u}}{\partial t}+\rho(\bar{u}\cdot\nabla)\bar{u}= -\rho\bar{g}\beta(T-T_0)-\nabla P+\mu\nabla^2\bar{u}+\rho_c\bar{E}-\frac{1}{2}E^2\nabla\varepsilon+\nabla\left[\frac{1}{2}\rho E^2\left(\frac{\partial\varepsilon}{\partial\rho}\right)_T\right] \tag{3.6}$$

Equation (3.6) can be non-dimensionalized using the following non-dimensional parameters

$$\boldsymbol{\bar{u}}=\frac{\bar{u}}{U_o},\ \boldsymbol{P}=\frac{P}{\rho_o U_o},\ \tau=\frac{tU_o}{L},\ \tilde{x}=\frac{x}{L},\ \theta=\frac{T}{T_o},$$

$$\eta=\frac{\bar{E}}{E_o},\ \varepsilon_r=\frac{\varepsilon}{\varepsilon_o},\ \tilde{\nabla}=L\nabla$$

Substituting the non-dimensional parameters into equation (3.6), the non-dimensional form of the EHD momentum equation is given as

$$\frac{\rho U_o^2}{L}\left(\frac{\partial \overline{\boldsymbol{u}}}{\partial \tau}\right)+\frac{\rho U_o^2}{L}(\overline{\boldsymbol{u}}\cdot\tilde{\nabla})\overline{\boldsymbol{u}}$$
$$=-\rho\bar{g}\beta(T_o\theta-T_0)-\frac{\rho U_o}{L}\left(\frac{\partial \boldsymbol{P}}{\partial \tilde{x}}\right)+\frac{\mu U_o}{L^2}\left(\frac{\partial^2 \overline{\boldsymbol{u}}}{\partial \tilde{x}^2}\right)+\rho_c\bar{E}$$
$$-\frac{1}{2}E^2\nabla\varepsilon+\nabla\left[\frac{1}{2}\rho E^2\left(\frac{\partial\varepsilon}{\partial\rho}\right)_T\right] \tag{3.7}$$

Dividing equation (3.7) by $\frac{\rho U_o^2}{L}$, the conditions in which the various components of the EHD body force will have a significant effect on the fluid flow can be determined by analyzing each of the various non-dimensional components individually.

Looking at the electrophoretic term (4th term on RHS of Eq. (3.7)), the term can be rearranged as follows

$$\left(\frac{L}{\rho U_o^2}\right)\rho_c\bar{E}=\left(\frac{L}{\rho U_o^2}\right)\frac{\sigma_e}{\mu_e}E_o\eta=\left(\frac{1}{Re^2}\right)\left(\frac{L^3\sigma_e E_o}{\nu^2\mu_e\rho}\right)\eta=\left(\frac{Ehd}{Re^2}\right)\eta \tag{3.8}$$

where the Ehd number can be defined, assuming that the free charge within the fluid is entirely due to charge injection ($\sigma_e E_o=J_o=I_o/A$), as

$$Ehd=\frac{\sigma_e E_o L^3}{\nu^2\mu_e\rho}=\frac{IL^3}{\nu^2\mu_e\rho A} \tag{3.9}$$

and

$$Re=\frac{U_o L}{\nu} \tag{3.10}$$

A similar analysis can be performed on the dielectrophoretic term (5th term on RHS of Eq. (3.7)).

$$\left(\frac{L}{\rho U_o^2}\right)\frac{1}{2}E^2\nabla\varepsilon=\left(\frac{L}{2\rho U_o^2}\right){E_o}^2\varepsilon_o(\nabla\varepsilon_r)\eta^2 \tag{3.11}$$

The gradient of the dielectric constant may be expanded as follows

$$\nabla\varepsilon_r = \left(\frac{\partial\varepsilon}{\partial T}\right)_\rho \nabla T + \left(\frac{\partial\varepsilon}{\partial\rho}\right)_T \nabla\rho \tag{3.12}$$

Substituting Eq. (3.12) into (3.11) and assuming a constant density, $\nabla\rho \approx 0$, the dielectrophoretic term may be rewritten as

$$\begin{aligned}\left(\frac{L}{\rho U_o^2}\right)\frac{1}{2}E^2\nabla\varepsilon &= \left(\frac{Lv^2}{2\rho U_o^2 v^2}\right)E_o{}^2\varepsilon_o\left(\left(\frac{\partial\varepsilon}{\partial T}\right)_\rho \nabla T\right)\eta^2 \\ &= \frac{1}{2}\left(\frac{v^2}{\rho U_o^2 v^2}\right)\left(\frac{L^2}{L^2}\right)E_o{}^2\varepsilon_o\left(\frac{\partial\varepsilon}{\partial T}\right)_\rho T_o\left(\frac{\partial\theta}{\partial\tilde{x}}\right)\eta^2 \\ &= \left(\frac{1}{Re^2}\right)\left(\frac{\varepsilon_o E_o^2 T_o\left(\frac{\partial\varepsilon}{\partial T}\right)_\rho L^2}{2\rho v^2}\right)\eta^2\tilde{\nabla}\theta \\ &= \left(\frac{Md}{Re^2}\right)\eta^2\tilde{\nabla}\theta\end{aligned} \tag{3.13}$$

where

$$Md = \frac{\varepsilon_o E_o^2 T_o\left(\frac{\partial\varepsilon}{\partial T}\right)_\rho L^2}{2\rho v^2} \tag{3.14}$$

The last EHD body force component in Eq. (3.7) is the electrostrictive component. Assuming that the gradient of the dielectric constant may be approximated as [Landau and Lifshitz (1963)]

$$\rho\left(\frac{\partial\varepsilon}{\partial\rho}\right)_T \sim \varepsilon_o\left(\frac{\partial\varepsilon}{\partial T}\right)_\rho T \tag{3.15}$$

The electrostrictive term in the non-dimensional momentum equation may be simplified as follows

$$\begin{aligned}\left(\frac{L}{\rho U_o^2}\right)\nabla\left[\frac{1}{2}\rho E^2\left(\frac{\partial\varepsilon}{\partial\rho}\right)_T\right] &= \left(\frac{L}{\rho U_o^2}\right)\nabla\left[\frac{1}{2}E_o^2\varepsilon_o\left(\frac{\partial\varepsilon}{\partial T}\right)_\rho T_o\theta\eta^2\right]\\ &= \left(\frac{L}{\rho U_o^2}\right)\left(\frac{L^2\nu^2}{L^2\nu^2}\right)\nabla\left[\frac{1}{2}E_o^2\varepsilon_o\left(\frac{\partial\varepsilon}{\partial T}\right)_\rho T_o\theta\eta^2\right]\\ &= \left(\frac{1}{Re^2}\right)L\nabla\left[\frac{\varepsilon_o E_o^2 T_o\left(\frac{\partial\varepsilon}{\partial T}\right)_\rho L^2}{2\rho\nu^2}\theta\eta^2\right]\\ &= \left(\frac{Md}{Re^2}\right)\tilde{\nabla}\theta\eta^2\end{aligned} \tag{3.16}$$

Equations (3.8), (3.13) and (3.16) can be used to predict when the electrophoretic, dielectrophoretic and electrostrictive forces will have an influence on the fluid flow. Two dimensionless numbers arise from the analysis, which are the EHD number (Ehd) and the Masuda number (Md), and they give the ratio between the electrophoretic and dielectrophoretic/electrostrictive force (or polarization force) to the fluid viscous force, respectively. The dimensional analysis performed shows that the electrophoretic force will be significant when the ratio of the dimensionless EHD number over the square of Reynolds number is of the same order of magnitude or greater (i.e. Ehd $\geq$ Re^2) and the dielectrophoretic/electrostrictive force will be significant when the ratio of the dimensionless Masuda number over the square of Reynolds number is of the same order of magnitude or greater (i.e. Md $\geq$ Re^2).

3.3.2 Electrical Stability Parameter

The onset of convection due to EHD can be predicted by knowing the applied voltage. The critical voltage for electroconvection can be determined using a model developed by Atten and Lacroix (1978) to determine the value of the dimensionless parameter T_C,

$$T_C = \frac{\varepsilon|V|}{\mu\mu_e} \tag{3.17}$$

The parameter T_C is the electrical stability parameter and is analogous to the Rayleigh number (Ra) [Paschkewitz (2000)]. The Rayleigh number indicates if heat transfer is mainly dominated by free (natural) convection or by conduction. The parameter T_C is similar to the Rayleigh number but will give the ratio between the electrical and viscous forces and provides insight into the stability of an EHD flow. Atten and Lacroix (1978) determined experimentally that the critical value of T_C for electroconvection is approximately 100.

3.3.3 Dimensionless Parameter V_E

The dimensionless parameter V_E was proposed by Bologa and Didkovesky (1977) and gives the ratio of the electric force to the surface tension. This parameter is given as

$$V_E = \frac{\varepsilon_v {E_v}^2 L}{\sigma} \tag{3.18}$$

The characteristic length, L, in the equation represents the inter-electrode gap. This dimensionless parameter is an integral parameter in the correlations for the prediction of EHD condensation heat transfer (see Section 3.5.4).

3.4 Fundamentals of Single-Phase Electrohydrodynamics

In single-phase flows, the EHD forces (Eq. (3.5)) influencing the fluid flow is simplified. The dielectrophoretic and electrostrictive forces are generally neglected in single-phase flows because these forces are due to a gradient in the dielectric permittivity as a result of phase differences and differences in temperature/pressure respectively. The permittivity can typically be considered homogenous in single-phase flows and therefore only the electrophoretic force will be applicable. The electrophoretic force is the force acting on the free charges within the fluid bulk due to an applied electric field and the motions produced were first described by Avsec and Luntz (1937) as electroconvective eddies (also referred to as electroconvection). The electroconvection phenomenon is dependent on the flow channel geometry, as shown in Figure 3.1 and Figure 3.2.

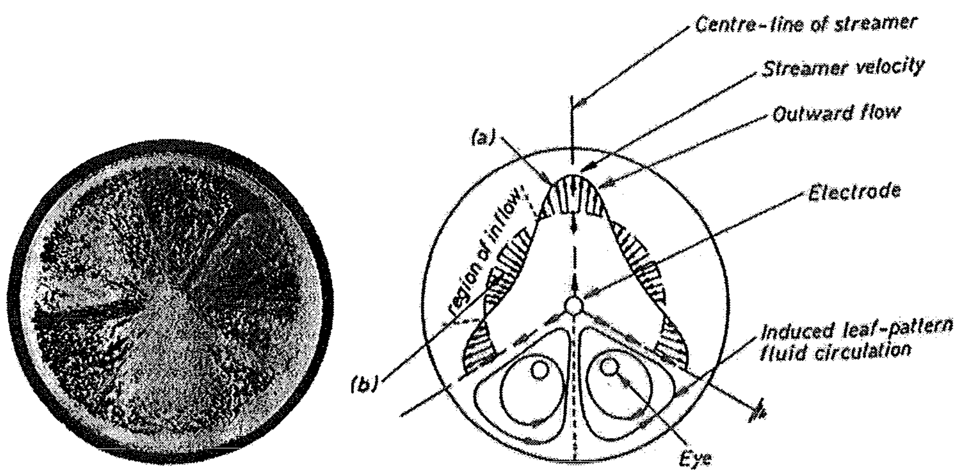

(i) (ii)

Figure 3.1 – (i) Streak photograph and (ii) schematic illustration of the electroconvective leaf pattern in a circular channel for a stationary flow [Fernández and Poulter (1987)]

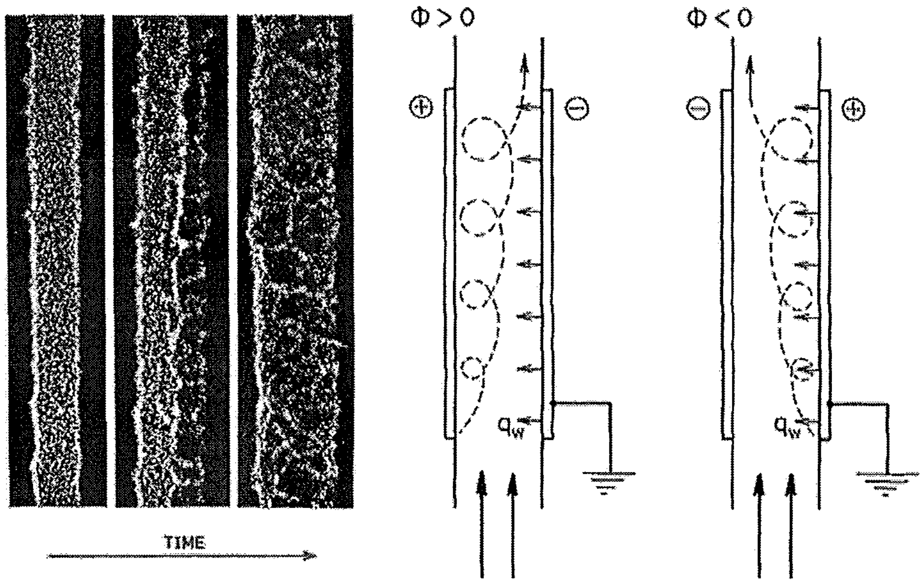

(i) (ii)

Figure 3.2 – (i) Shadowgraph images, with 0.2secs between images, and (ii) schematic illustration of the electroconvective flow pattern for an upward flow between vertical parallel plates [Fujino and Mori (1989)].

Fernández and Poulter (1987) investigated the effect of electroconvection in a circular channel sandwiched between two transparent plates to visualize the flow. High voltage was applied using a concentric wire electrode for various working fluids (transformer oil, carbon tetrachloride, ether, refrigerant 113, toluene, diacetone alcohol, benzene and xylene). For an initially stagnant fluid, a radial flow pattern was observed upon applying high voltage and well-defined "leaf-pattern" circulation zones were present, as shown in Figure 3.1. Experiments were performed for a thin circular slice test section and also for a test section several diameters in lengths. The leaf patterns were observed in both instances, indicating that the motions are predominantly in the radial direction and that the end effects did not have a significant influence on the radial flow pattern observed.

Fernández and Poulter determined that the intensity of the circulation zones increased with the current at a constant voltage, increased with negative polarity voltages and increased at higher temperatures. When an axial flow is imposed, the well-defined leaf patterns are no longer present.

In parallel plate geometries, the electroconvection phenomenon was investigated by Fujino and Mori (1989) with R-113 as the working fluid. Fujino and Mori investigated the effect of voltage polarity and heat flux on electroconvection and the results are shown in Figure 3.2. Using laser shadowgraphy (Figure 3.2(i)), longitudinal rolls were observed to have developed from one electrode wall and increase in size over time. Fujino and Mori hypothesized that the origin of the free charges in the liquid was due to unipolar charge injection at the electrodes (mobility model) and not to the change in conductivity as a result of temperature gradients (conduction model) [See Section 2.2.5 for details on charge injection] and that the charge injected is negative ions from the negative electrode. This hypothesis matched their experimental results as well as numerical models developed by Hopfinger and Gosse (1971) and Suzuki and Sawada (1983). Fujino and Mori observed that the longitudinal rolls developed on the side opposite to the charge injecting electrode as a result of the shear caused by the migration of charge from the injecting electrode to the grounded electrode, as depicted in Figure 3.2. The heat transfer coefficients were experimentally determined and found to be higher at the surface opposite to the charge injection as a result of the electroconvection destabilizing the thermal boundary layer and enhancing the heat transfer in that region. The numerical models by Hopfinger and Gosse showed that the rate of production of turbulent energy is higher at the side opposite to charge injection and the model by Suzuki and Sawada showed that the electroconvective eddies have centers that are offset from the side of charge injection and are closer to the grounded electrode. Both these models are consistent with the findings of Fujino and Mori and support their hypothesis on the mechanisms of charge injection. As the electrophoretic force is the force acting on the free charges due to an applied electric field, the origins of the free charges are significant in predicting the flow characteristics.

3.4.1 Review of Single-Phase EHD Heat Transfer and Pressure Drop

The heat transfer enhancement in single-phase flows using EHD is due to the electroconvection phenomenon discussed in the previous section. As the strength of the electroconvection is dependent on the charge injection and electric field strength, factors such as the working fluid, applied voltage, voltage polarity, and heat flux will have a significant effect on heat transfer and pressure drop. Porter and Smith (1974), Fernández and Poulter (1987) and Cotton (1997) studied the effect of EHD on single-phase flow using different types of oil as the working fluid while Fujino and Mori (1987), (1989) used refrigerant R-113 as the working fluid. In all studies, an increase in applied voltage increases heat transfer as expected because the increase in the electric field strength results in an increase in the electroconvection and charge injection. The effect of applied voltage has a unique effect on the pressure drop. Fujino and Mori (1989) and Cotton (1997) observed that the pressure drop increases with an increasing voltage up to a critical voltage and a further increase in the applied voltage will begin to decrease the pressure drop. The decrease in the pressure drop above a specific threshold is most likely due to the negative electroviscous effect, where an increase in the charge injection due to the applied voltage results in an axially developing layer of charge on the electrodes that stresses the fluid in the direction of the flow [Honda and Atten (1978)]. In the experiments by Porter and Smith (1974) and Fujino and Mori (1989), the effect of heat flux was investigated with conflicting results. Porter and Smith measured higher heat transfer coefficients for a higher heat flux while the experiments by Fujino and Mori showed that the heat transfer was independent of the heat flux. The discrepancy in the results may be attributed to the fact that Porter and Smith used oil as the working fluid and a brass and copper plate for the electrodes while Fujino and Mori used refrigerant and glass plates as the electrode. For the effect of voltage polarity, both Fernández and Poulter (1987) and Fujino and Mori (1989) showed an increase in heat transfer for a negative polarity. This is a result of a greater interaction of the electroconvective eddies with the heat transfer surface in their particular set-up (see Section 3.4). The effect of mass flux was investigated by Cotton (1997) and it was determined that the heat transfer decreases with an increasing mass flux, as expected according to the dimensionless analysis presented in Section 3.3. A summary of the select EHD single-phase experiments is given in Table 3.1.

Table 3.1 – Select EHD studies on single-phase heat transfer.

Source	Heat Transfer Surface	Electrode Geometry	Working Fluid	Comments
Porter and Smith (1974)	Rectangular channel	Brass Upper Plate and Copper Lower Plate	Transformer Oil/Kerosene	DC electric fields. Heat transfer coefficient increases with applied voltage and heat flux.
Fernández and Poulter (1987)	Glass tube with a Metallic Coating	Wire in Tube	Transformer Oil with polystyrene beads as tracers	Radial flow pattern observed in stationary flow. Higher heat transfer results for negative polarity due to higher current.
Fujino and Mori (1987)	Vertical Parallel Plate Channel	Semi-silvered Vertical Glass Plates	R-113	Electrically induced longitudinal rolls observed. No dependency on the heat flux.
Fujino and Mori (1989)	Vertical Parallel Plate Channel	Pyrex Glass with Lead Oxide or Nickel-Plated Bakelite Plate	R-113 (with and without electrolyte solution, ASA-3)	Negative voltages higher heat transfer. Enhancement greater in the Bakelite plate than glass when positive voltage applied and opposite effect with negative voltage.
Cotton (1997)	Annulus	Stainless Steel Rod Electrode and Inner Tube.	Transmission Oil (Type *Glide F*)	Increase in heat transfer with applied voltage. Decreases as the mass flow rate increases. Pressure drop decreases due to EHD.

3.5 Fundamentals of Two-Phase Electrohydrodynamics

Electrohydrodynamics in two-phase flows are more complex than in single-phase flows because in addition to the complexities associated with two-phase flows as described in Section 2.3.2, the dielectrophoretic component in the EHD body force equation (Eq. (3.5)) and the interactions between the free charge and the liquid-vapour interface must be considered along with the electrophoretic component in each of the individual phases. These interactions are discussed in this section.

3.5.1 Dielectrophoretic Force and Liquid Extraction

Liquid extraction is the effect of liquid being pulled towards a high voltage electrode due to EHD induced instabilities at a liquid and gas interface. This phenomenon is illustrated in Figure 3.3. Upon application of an electric field, the neutral molecules in the fluid will become polarized and establish dipoles. Liquid extraction occurs because of the differences in the electrical permittivity between the liquid and vapour phases. In dielectric fluids, the electric fields are generally stronger in a vapour phase and the polarized molecules will become more strongly attracted towards the vapour region. By applying sufficiently strong electric fields to a fluid medium, it is possible that the EHD forces may overcome the other forces governing the flow (such as forces due to gravity, the fluid velocity, the fluid viscosity and surface tension) and liquid extraction will occur. This phenomenon leads to redistribution of the fluid flow (change in flow pattern) and significant increase to the interfacial area. The significance of this effect is that it has a

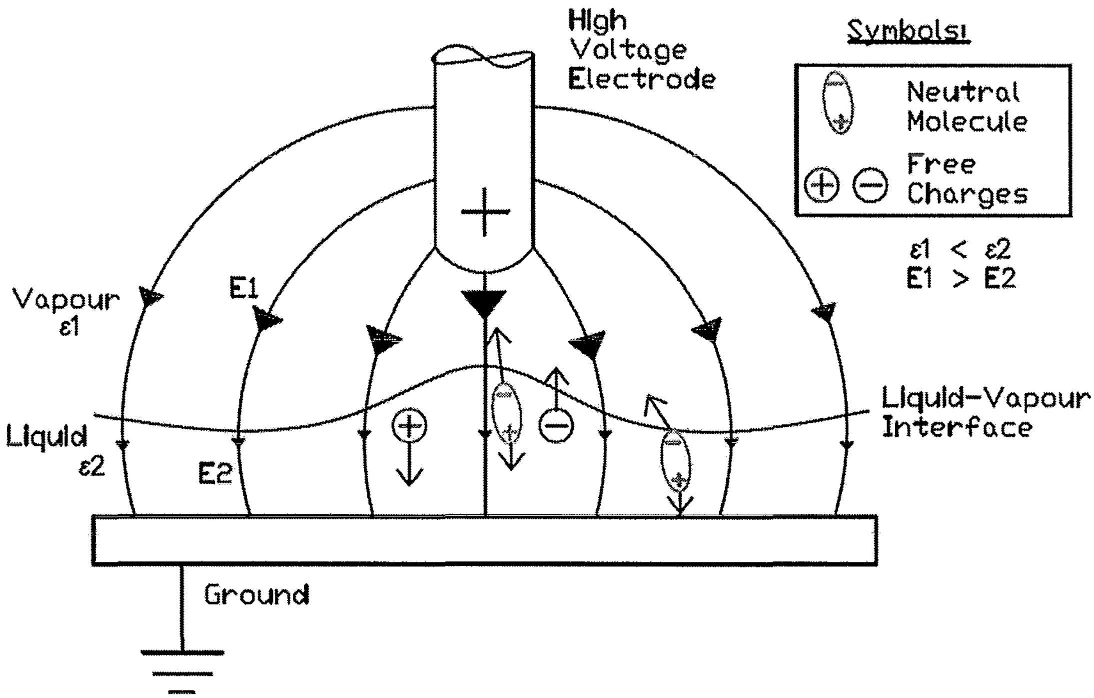

Figure 3.3 – Liquid extraction phenomenon.

large impact on the thermal hydraulic characteristics of a flow, as discussed in Section 2.3.2.2.

3.5.2 Charge Relaxation

The charge relaxation time is a measure of the time for the free charges to relax from the bulk of the dielectric fluid medium to the outer boundary. The relaxation time can be estimated as:

$$\tau_c = \frac{\varepsilon}{\sigma} \tag{3.6}$$

This time is significant as it may be used to determine the components of the EHD forces affecting the medium. For example, the electrophoretic force will have an influence on a dielectric vapour bubble when the charges accumulate at the vapour bubble interface. If the charges were not given enough time to relax to the interface (i.e. when the frequency of the applied electric field is << $1/\tau_c$) than other EHD body forces, such as the dielectrophoretic force, may dominate. The charge relaxation time for refrigerant R-134a is determined to be 1.48s.

3.5.3 Review of Studies on EHD Two-Phase Condensation

There have been various EHD two-phase flow studies performed undergoing both evaporation and condensation. As the focus of the heat transfer experiments in this research is solely on the effect of EHD on internal two-phase condensation, only a detailed review of condensation EHD studies is presented.

Numerous experimental studies have been performed to investigate condensation heat transfer enhancement on horizontal surfaces using EHD and a select list of this research is presented in Table 3.2. For applied DC voltages, Cheung et al. (1999) studied external EHD condensation while Singh et al. (1995), Cotton (2009) and Sadek et al. (2010) studied internal EHD condensation of R-134a on horizontal tubes. Experiments were conducted for different heat flux, electrode gaps, inlet quality (internal condensation), mass flux (internal condensation) and applied electric field strengths for smooth tubes. The EHD effect on complex heat transfer surfaces, such as corrugated tubes, and for different fluid properties was investigated by Gidwani et al. (2002). Three different refrigerants, R-134a, R-404a and R-407c, were studied and the results showed a continuous increase in heat transfer for increasing applied DC voltage up until the point of electrical breakdown of the fluid. A plateau in the heat transfer enhancement for an

Table 3.2 – Select EHD studies on two-phase condensation heat transfer.

Source	Heat Transfer Surface	Electrode Geometry	Working Fluid	Max Enhancement, η	Comments
Choi (1968)	Vertical Tube	Coaxial Tube	R-113	2	In-tube Condensation (laminar film)
Didkoski and Bologa (1981)	Vertical Plate	Vertical Slotted Plate	R-113, Diethyl ether, n-Hexane	20	Film Condensation, both in DC and AC
Yabe et al. (1982)	Vertical Plate	Straight Wire	R-113	2.2	Film Condensation
Joos and Shaddon (1985)	Vertical Tube	Rod	R-113	1.7	In-tube Condensation
Yabe et al. (1987)	Vertical Smooth Tube	Helical Wire	R-113	2.8	External Condensation
Yamashita et al. (1991)	Vertical Smooth Tube Bundle	Helical Wire with Lattice Electrode	$^{a}C_6F_{14}$ and ^{b}R-114	^{a}4 and ^{b}6	External Condensation
Yamashita and Yabe (1995)	Vertical Smooth Tube Bundle	Helical wire with lattice electrode	R-123	5.9	External Condensation
Bologna et al. (1995)	Horizontal Plate	Plate	R-113	1.8	Film Condensation
Kodama et al. (1995)	Vertical Plate	Needle Electrode	R-113	1.9	Film Condensation
Singh et al. (1995)	Horizontal Tube	Various Coaxial Electrodes	R-134a	3.0	In-tube Condensation
Cheung et al. (1999)	Horizontal and Vertical Tube	Helical Electrode	R-134a	7.2	External Condensation
Gidwani et al. (2002)	Horizontal Tube	Rod Electrode	^{a}R-134a, ^{b}R-407c and ^{c}R-404a	^{a}8.3, ^{b}3.9 and ^{c}18.8	In-tube Condensation
Cotton (2009)	Horizontal Tube	Rod Electrode	R-134a	3.0	In-tube Condensation
Sadek et al. (2009)	Horizontal Tube	Rod Electrode	R-134a	2.8	In-tube Condensation

increasing applied voltage was not observed for tube side configurations, which was present in EHD condensation on external surfaces [Gidwani et al. (2002)]. It was also found that the enhancement potential of the fluids differed because of differences in the density, viscosity, electrical permittivity, interfacial surface tension and dielectric constant. This was evident by the different enhancement ratios of the various fluids. The physical mechanisms responsible for the enhancement of heat transfer are summarized by Bologa et al. (1996). These mechanisms include the dispersion of the thin liquid films, breakup and mixing of the different phases, electroconvection and boundary layer turbulence. Al-Ahmadi and Al-Dadah (2002) presented correlations for determining the heat transfer in EHD condensation for tube geometries. Details of these correlations are presented and discussed in Section 3.5.4.

The EHD enhancement of heat transfer in two-phase flows is highly dependent on the flow pattern prior to application of EHD. For enhancement of condensation heat transfer, one of the main mechanisms involved is in the use of EHD to remove the condensate at the heat transfer surface by liquid extraction and dispersion of this liquid by the electric body forces. Higher applied voltages result in a greater electric body force to extract condensate from the heat transfer surface, thereby increasing heat transfer. The EHD enhancement of heat transfer in tube geometries is found to be greatest when the flow pattern is stratified/stratified wavy and gravity has a dominant role in establishing this flow pattern [Gidwani et al. (2002)]. In this flow pattern, the dominant mode of heat transfer is by conduction through the thin condensate film at the upper region of the tube [Dobson and Chato (1998)]. The condensate is thicker in a stratified flow regime because of the low vapour velocity and there is greater ability for the EHD body forces to thin the condensate layer and increase the convection in the layer. The effect of EHD on a stratified/stratified wavy flow pattern can be seen in the EHD two-phase flow pattern map was developed by Cotton et al. (2005), who modified the flow pattern map of Steiner (1993) to account for the EHD forces. The EHD flow pattern map was developed by incorporating the interfacial EHD force at the liquid and vapour interface to the flow pattern transition equation to determine the new flow pattern transition lines. The EHD flow map is shown in Figure 3.4 and a review of the map shows that EHD can be used to transition the flow to either an EHD annular or intermittent type of flow at a lower mass flux than without EHD. The enhancement in heat transfer by using EHD on an initially

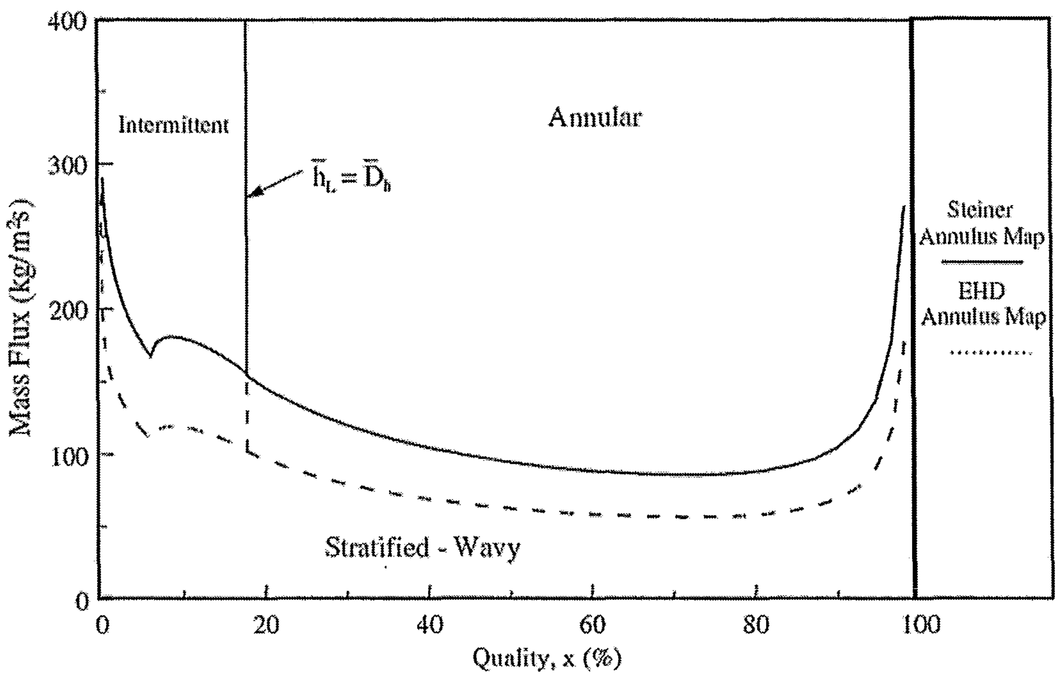

Figure 3.4 – EHD flow pattern map for an annular channel under an 8kV DC voltage [Cotton et al. (2005)]

stratified flow pattern is that the heat transfer coefficient can be increased to a value comparable to that of film condensation [Sadek (2010)]. At a high mass flux the higher vapour shear results in increased turbulence, thinning of the condensate film and increased interfacial mass and momentum transfer between the phases leaving less potential for enhancement. The decrease in the effect of EHD on heat transfer enhancement for an increase in mass flux is expected based on the dimensionless analysis presented in Section 3.3.1. Therefore, the EHD effect has the most prominent effect at low mass fluxes where the flow is gravity driven.

In all the EHD two-phase flows studies with an applied DC voltage, one noticeable effect in using EHD to enhance heat transfer is that the corresponding increase in pressure drop ratio is also observed. An increase in the pressure drop occurs because the increase in interfacial area due to the flow redistribution results in an increase in the frictional component of the pressure drop and also because EHD increases heat transfer. An increase in heat transfer results in a greater mass transfer due to a phase change, resulting in an increase in the momentum component of pressure drop. The effect of a DC voltage on the pressure drop can be observed in the work by Gidwani et al. (2002). Gidwani et al. showed that applying EHD to a two-phase flow of refrigerant R-134a resulted in a maximum heat transfer enhancement of 8.3-fold, however a corresponding pressure drop penalty of 20.8-fold was experienced.

The majority of the research performed for EHD condensation involved the use of DC applied voltages. More recently, Cotton (2009) and Sadek (2009) investigated the effect of AC or pulse waveforms on a two-phase flow of R-134a to achieve a finer control of the EHD enhancement of condensation heat transfer and pressure drop. In the work by Cotton (2009), the results show that a range of control of heat transfer and pressure drop can be established using a combination of DC and AC voltages as the effect of AC waveforms on heat transfer and pressure drop differs from the case of a DC voltage. For example, in the study by Cotton, an average voltage of 6kV showed that the DC case exhibits higher heat transfer while the AC case showed higher pressure drop. Differences in the heat transfer and pressure drop between the DC and AC cases was due to different flow patterns, such as an inverse annular flow in the DC and oscillatory entrained droplet flow pattern in the AC case. In the work by Sadek et al. (2009), the effect of frequency, waveform, DC offset and amplitude was investigated. Sadek et al. determined that the transient flow pattern observed during the initial step input of high voltage differs from the steady state flow pattern. In the transient flow patterns, twisted liquid cone flow structures (discussed and shown in greater detail in Chapter 6) were observed. During the initial application of high voltage, extraction of the liquid from the lower liquid stratum towards the rod electrode occurs due to the EHD body force. Once the liquid encompasses the electrode, the liquid is pushed radially outward in the form of twisted liquid cones. The twisted liquid cone flow structures are of interest because they exhibit characteristics favourable to the enhancement of heat transfer, such as a considerable bulk mixing of the fluid and liquid extraction from the heat transfer surface and into the central core. Sadek et al. observed these flow structures and presented the various time scales on the development and decay of the structures, but did not investigate methods in sustaining these flow structures during the steady state.

3.5.4 EHD Two-Phase Condensation Heat Transfer Correlations

There have been numerous studies on the development of correlations to determine the condensation heat transfer with EHD. Correlations have been proposed by Choi (1968), to determine the heat transfer of an EHD flow where the condensate film was completely removed from the heat transfer surface, by Bologa and Didkovesky (1977) to predict film condensation enhancement using electric fields in polar and non-polar fluids, by Smirnov and Lunev (1978) for an upward condensing flow in a vertical tube for DC and AC electric fields, by Dyakowski et al (1982) for EHD condensation on the outside of vertical plates, by Trommelmans et al. (1985) for EHD condensation on the underside of horizontal plates and by Al-Ahmadi and Al-Dadah (2002) on EHD condensation inside and outside for both horizontal and vertical tubular systems. Only the correlation by Al-Ahmadi and Al-Dadah on horizontal EHD condensation inside tubes is directly applicable to the research in this thesis and will be presented in detail.

Al-Ahmadi and Ad-Dadah (2002) first presented their correlation for predicting the EHD condensation heat transfer inside a horizontal tube in the following form

$$h = \frac{C}{\Delta T^n} \tag{3.19}$$

where ΔT is the temperature difference between the saturated fluid temperature and the heat transfer surface wall temperature. The constants C and n in Eq. (3.19) are determined empirically using the experimental data of Singh (1997). This experimental data consisted of 12 measurements of the EHD condensation heat transfer inside a horizontal tube with an inner diameter of 11.0mm and a coaxial wire 3mm in diameter to apply the EHD.

Eq. (3.19) was later re-written by Al-Ahmadi and Ad-Dadah (2002) to incorporate the various mechanisms involved in an electrohydrodynamic fluid flow and to improve the correlation. In the revised correlation, the authors included the effect of the EHD force and surface tension by incorporating the dimensionless group, V_E (see Section 3.3.3), perturbations in the condensate film where included using a length scale describing the fastest growing wave in a condensate film, λ^*, and the thermal properties, such as the thermal conductivity, specific heat and the modified latent heat enthalpy of evaporation, h'_{lv}, and the inter-electrode gap, L, were also considered. The length scale λ^* defined was defined by Choi (1968) as

$$\lambda^* = \frac{2\pi}{K^*} \tag{3.20}$$

where K^* is the characteristic wave number and given as

$$K^* = \frac{3}{4\sigma_l}\left(1 - \frac{\varepsilon_v}{\varepsilon_l}\right)^2 \varepsilon_v {E_v}^2 \tag{3.21}$$

The modified latent heat of evaporation can be determined as

$$h'_{lv} = h_{lv} + 0.86 c_{p_l} \Delta T \tag{3.22}$$

Therefore, the authors revised Eq. (3.19) to the following form

$$\frac{h_E \lambda^*}{k_l} = Nu_E = A\left[\frac{{V_E}^m h'_{lv}\left({\lambda^*}/{L}\right)^f}{c_{p_l}\Delta T}\right]^{n_1} \tag{3.23}$$

The constants A, f, m and n_1 in Eq. (3.21) were determined to be 30, 0.29, 1.75 and 4.5, respectively, for EHD condensation inside a horizontal tube. This correlation was found to predict the tube side EHD condensation heat transfer within ±30%.

3.6 Summary of Electrohydrodynamics Research

The EHD technique was shown to be capable of enhancing heat transfer in both single-phase and two-phase dielectric fluid flows. In single-phase EHD studies, the enhancement was determined to be due to the electrophoretic force and is dependent on the amount of charge injected into the fluid. The method of charge injection in single-phase flows is currently unclear as different researchers have proposed different methods of charge injection [Fujino and Mori (1989), Porter and Smith (1974)] which may be due to the differences in their experimental set-up. Therefore, further investigation of the method of charge injection in various system configurations is required.

In the two-phase condensation heat transfer studies, the dielectrophoretic force was found to enhance heat transfer by redistributing the liquid and vapour phases within the flow channel by liquid extraction. Studies have been performed for DC, AC and pulse applied voltages and the flow patterns were determined to be different between the various cases. An inverse annular flow pattern is observed for an applied DC voltage, an oscillatory entrained droplet flow pattern was observed for an applied AC voltage and a flow pattern consisting of twisted liquid cone flow structures were observed for an applied pulse voltage. For these three cases, the applied pulse voltage flow pattern is the least understood as the mechanisms involved in the development of the twisted liquid cone structures and a measure of the associated heat transfer and pressure drop performance of this type of flow pattern have not been investigated. In addition, the twisted liquid cones were observed to be a transient flow structure and it is currently unknown if a flow pattern consisting of these structures can be sustained.

Chapter 4 – Experimental Facility and Methodology

4.1 Test Facility Capabilities

The test facility used in the experiments is a state-of-the-art system capable of applying high voltage electric fields to a single or two-phase flow in a horizontal annular channel, measuring the heat transfer performance in the test section, visualizing the flow pattern due to EHD and perform both condensation and evaporation heat transfer studies. Details of the various components in the system, the data reduction and experimental uncertainties are provided in this chapter.

4.2 The EHD Experimental Test Loop

A schematic of the experimental facility is shown in Figure 4.1 and the dielectric fluid used in the study is refrigerant R-134a (Details of the electrical and Thermophysical properties for R-134a can be found in Appendix A). A Pacific Scientific micropump (Model 2217560) is used to circulate the refrigerant in the test loop. The flow rate is measured upstream of the pump using one of the two turbine flow meters; an Omega FTB-502 for the low flow rates (0.1 to 1.0 L/min) and an Omega FTB-101 for high flow rates (1.32 to 13.2 L/min). The inlet condition into the test section is controlled using an electrical resistance heater. The electric heater is comprised of two stainless steel tubes

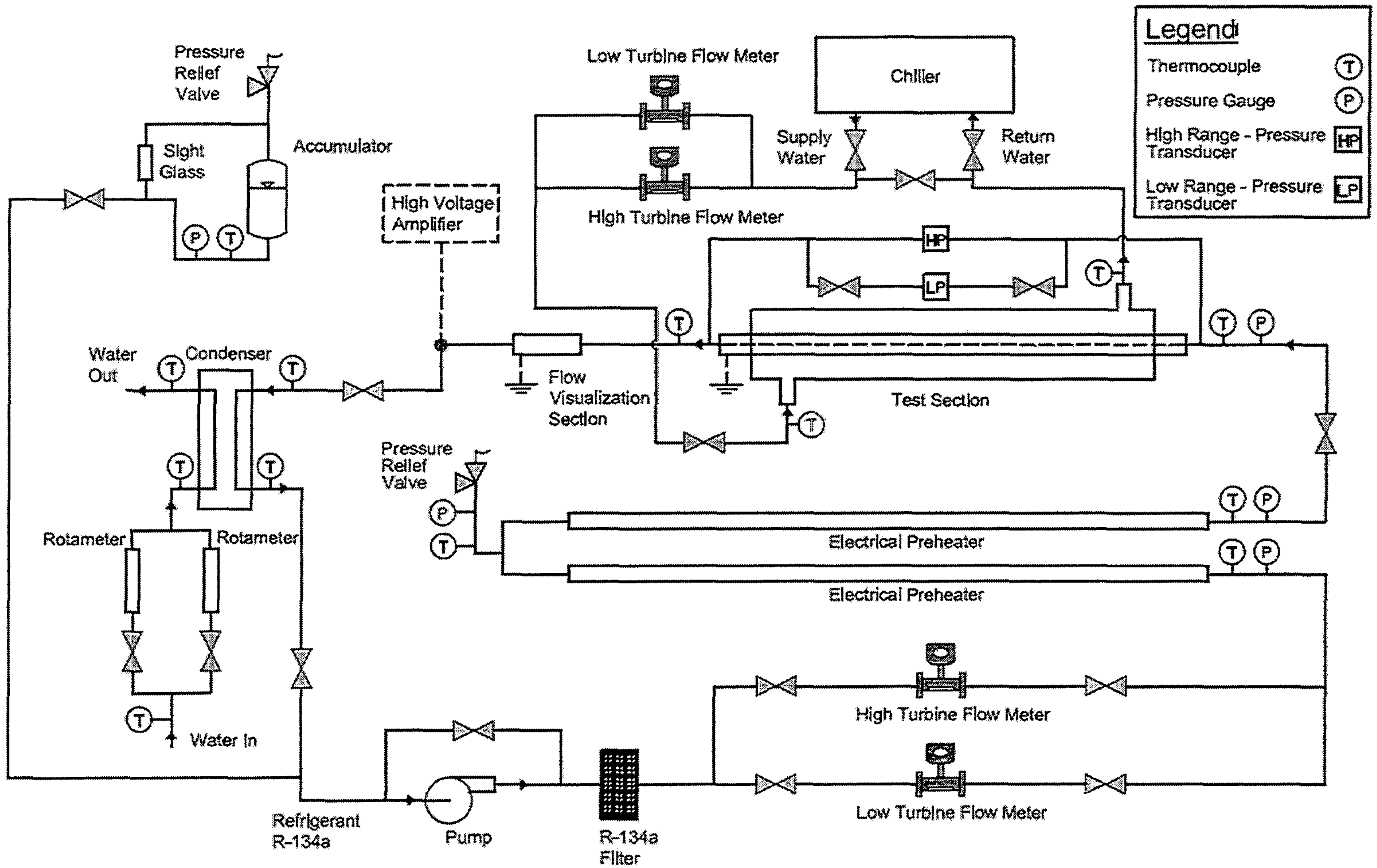

Figure 4.1 – Schematic of experimental test facility

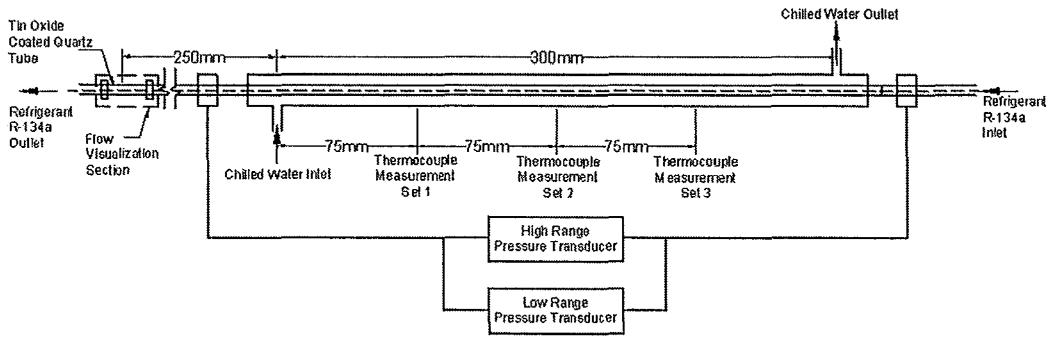

Figure 4.2 – Detail of heat exchanger and flow visualization test section.

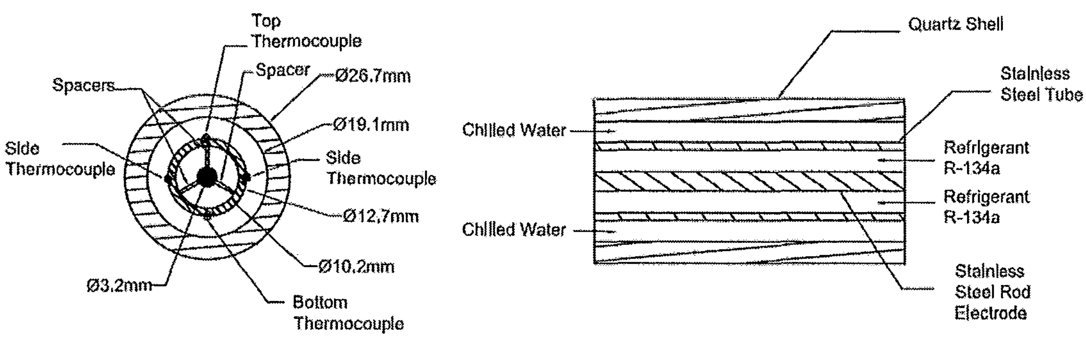

Figure 4.3 – Detail of heat exchange channel and electrode.

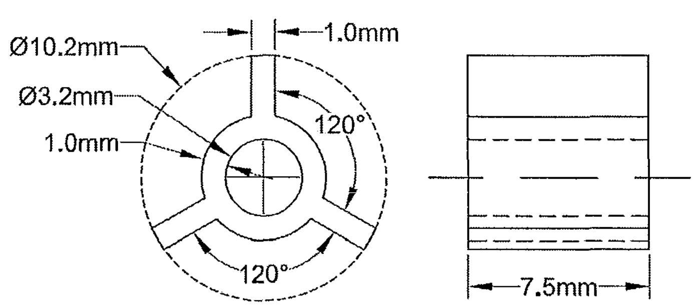

Figure 4.4 – Electrode spacer design.

(1.8m in length each) in series and an electric current is passed through the tubes using a Miller CST 250 power source (max capacity 6.4 kW). This electrically heated section is isolated from the rest of the loop using ceramic fittings and the inlet and outlet temperature and pressure was measured using thermocouples (Type T) and an analog pressure gauge respectively. The temperature measurements along with the voltage-current characteristics are used in determining the flow quality entering the test section (See Section 4.6).

There are two test sections used in the loop, one test section to measure the EHD heat exchange properties of the refrigerant flow and another to visualize the flow pattern redistribution due to EHD. Details of the heat exchange test section are shown in Figure 4.2 and Figure 4.3. The EHD heat exchange section is a counter current shell and tube system with refrigerant flowing through the tube side (stainless steel tube, outer diameter of 12.7mm and inner diameter of 10.2mm) and water flowing through the shell side (clear PVC tube, outer diameter of 26.7mm and inner diameter of 19.1mm). The heat exchange section is 30mm in length and the heat transfer coefficient of the refrigerant flow was determined by measuring the outside tube surface temperature using sets of thermocouples (Type T, 0.5mm diameter), where each thermocouple is embedded in four equally spaced locations circumferentially along the tube, as shown in Figure 4.3, and in three locations along the test section at the locations indicated in Figure 4.2. The inlet and outlet temperatures on the refrigerant side are also measured using thermocouples (Type T, 1.6mm diameter) while the inlet and outlet temperatures on the water side are measured using platinum resistance temperature detector (RTD) probes (6mm diameter) connected to a Omega precision thermometer reader (DP251). The shell side water temperature was controlled using a Lytron RC045 chiller (5.9kW max. cooling capacity) and the flow rate was measured using a McMillan microturbine flow meter (Model 104 Flo-Sensor) for flow rates between 0.2 L/min to 2.0 L/min and an Omega FTB-101 for flow rates between 1.32L/min to 13.2L/min. The pressure drop in the refrigerant side between the test section inlet and outlet is measured using Validyne differential pressure transducers (DP-15) connected to a two channel Validyne signal conditioner. Two transducers are used, one calibrated for low pressure drops (0 to 1.4kPa) and another for high pressure drops (0 to 3.5kPa). The flow exiting the test section is cooled (and condensed in the two-phase flow experiments) using a water jacket. The inlet and outlet temperatures of both the refrigerant and water are measured using thermocouples (Type T, 1.6mm diameter) and the flow rate in the water side is measured using rotameters, one for low flow rates (0 to 3.1L/min) and one for high flow rates (0 to 10.2L/min).

The electric fields are applied to the system using a high voltage amplifier connected to a stainless steel rod electrode (3.2mm diameter) placed concentrically inside the refrigerant tube. High voltage is supplied to the rod electrode using a Trek Model 20/20C high voltage amplifier and the surrounding stainless steel tube is grounded. The rod electrode is supported using electrically non-conducting Delrin spacers (See Figure 4.4) at approximately the same axial locations as the thermocouples placements shown in Figure 4.2. The high voltage parameters, such as peak voltage, average voltage, frequency and voltage rise time were monitored using an Agilent oscilloscope (Model

54621A). The current was measured using an Armaco analog ammeter (working range between 0 to 25μA) in the studies involving a DC voltage.

A flow visualization section is located downstream of the heat exchanger test section to visualize the EHD flow patterns. In this section, a Thermostone transparent quartz tube (outer diameter of 11.8mm and inner diameter of 9.3mm), coated with an electrically conducting film of tin-oxide on the outside diameter, replaces the grounded stainless steel tube in the electrode-tube set-up in the heat exchanger test section. The flow is visualized using a high speed camera (Fastec Troubleshooter) with a recording rate of 2000fps at a resolution of 320x240. The positioning of the high speed camera is adjustable and in the experiments the camera is mounted in two-different orthogonal positions (side profile and from the top-down) to visualize the EHD flow phenomena. The flow visualized in this quartz tube section is expected to differ only slightly from the flow pattern observed inside the heat transfer section which contains a stainless steel tube. The dielectric constant of quartz is 4.2 and since the tube is coated on the outside of the tube, the electric field distribution will differ from a stainless steel tube. A numerical analysis was performed (see Appendix D) to determine the electric field distribution for a glass and stainless steel tube for two hypothetical cases, a stratified case and a stratified case with liquid surrounding the rod electrode. A comparison of the electric field strength showed that a maximum deviation in the electric field strength of 7.5% and 11.4% in the second case. In both cases, the trends in the electric field strength are similar and the difference is an offset in the magnitude of the electric field strength in the vapour region.

Therefore, the flow pattern observed in the quartz section is representative of the flow pattern in the heat exchange section.

4.3 The Data Acquisition and Monitoring System

The data acquisition system consists of a 16-bit National Instruments data acquisition card (NI PCI-6221) with 16 analog inputs. The data acquired from this card is listed in Table 4.1. For the thermocouple temperature measurements, the temperature measurement devices are connected to one of the two terminal blocks with signal conditioners, which are connected to the DAQ card through a DAQ chassis (SCXI-1000). The thermocouples used to measure the surface temperature of the tube in the heat exchange section are connected to a SXCI-1303 terminal block with a SXCI-1125 8-channel signal conditioner to minimize electrical noise because the conditioner is an electrically isolated module. The 8-channel limitation on the signal conditioner requires the data acquisition process to be operated twice to acquire one complete data set containing the temperatures from all 12 surface thermocouples. The thermocouples for the other measurements are connected to a SXCI-1320 terminal block with a SXCI-1102C 32-channel signal conditioner. In all thermocouple measurements, an ice bath, with a reference temperature of $0^{\circ}C$, is used for the cold junction. All experimental measurements in Table 4.1 were monitored in real-time using LabView. For all recorded measurements in LabView, the measurements obtained is the average value of 10000 measurements obtained over a 10s interval.

Table 4.1 – List of DAQ measurements

Refrigerant Measurements	Measurement Device
Surface temperature of outer tube in heat exchange test section.	T-Type Thermocouples (12x)
Inlet and outlet temperature at test section.	T-Type Thermocouples (2x)
Inlet and outlet temperature at electrical preheater.	T-Type Thermocouples (2x)
Inlet and outlet temperature at condenser.	T-Type Thermocouples (2x)
Flow rate (low)	FTB-502 Turbine Flow Meter (1x)
Flow rate (high)	FTB-101 Turbine Flow Meter (1x)
Differential pressure drop.	Validyne DP15 Pressure Transducer (2x)

Water Measurements	Measurement Device
Inlet and outlet temperature in heat exchange test section	Platinum RTD (2x), T-type Thermocouples (2x)
Inlet and outlet temperature at condenser.	T-Type Thermocouples (2x)
Inlet and outlet temperature at electrical preheater.	T-Type Thermocouples (2x)
Flow rate into heat exchange test section (low)	104 Flo-Sensor Microturbine Flow Meter (1x)
Flow rate into heat exchange test section (high)	FTB-101 Turbine Flow Meter (1x)

4.4 Flow Visualization Image Analysis

The imaging software, Photron FASTCAM Viewer 3, was used in the analysis of the flow visualization videos taken using the Fastec high speed camera. A frame-by-frame analysis was performed to identify the exact time of the beginning of the high voltage pulse, in order to time stamp the images at the appropriate phase in the high voltage waveform applied. Each individual image frame was analyzed to determine the frame corresponding to any sudden disturbances in the flow pattern, such as the sudden extraction of liquid towards the central electrode, and this frame indicates the onset of the

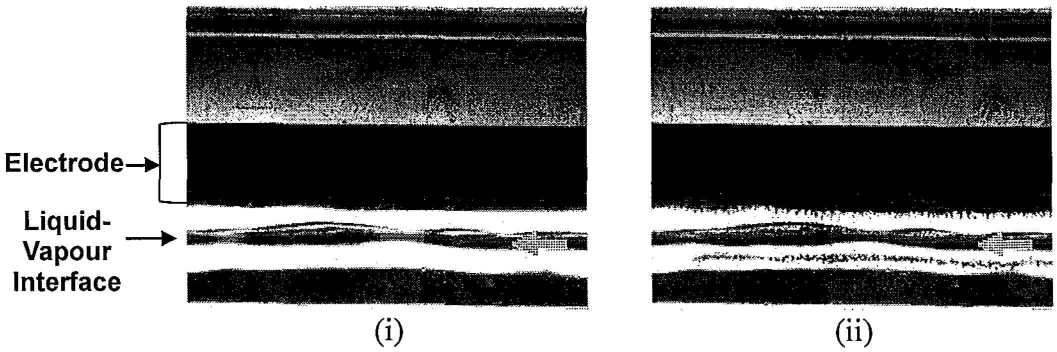

Figure 4.5 – Side profile of the image of the flow pattern (i) the frame immediately prior to application of EHD and (ii) the frame upon application of EHD.

high voltage pulse. An example of this analysis is shown in Figure 4.5, where image (i) shows the frame immediately prior to the start of the high voltage pulse and image (ii) shows the subsequent frame identifying the start of the application of high voltage, which is evident by the liquid extraction onto the electrode. The starting frame of a high voltage pulse is confirmed using a similar analysis to determine the frame in which the high voltage is removed and knowing the pulse waveform applied. The recording rate used in all flow visualization studies is 2000fps and therefore the time between successive frames is 0.5ms. This time also represents the uncertainty in time stamping the images on the pulse waveform.

4.5 Application of EHD

Continuous and pulse width modulated (PWM) high voltage waveforms were applied to both single and two-phase flow of R-134a to investigate the heat transfer and pressure drop characteristics. For the PWM waveforms, waveform parameters such as the duty cycle, pulse repetition frequency and pulse amplitude were carefully controlled to achieve a desired pulse duration and waveform. The duty cycle is defined as the ratio of the pulse duration over the period of the waveform. For example, a duty cycle of 0% is the base case of no EHD and 100% is for an applied DC voltage. The various waveform parameters are schematically shown in Figure 4.6. The duty cycle is also used to determine the effective voltage, which is defined as the average voltage applied over the total pulse cycle, and is given by

$$V_{eff} = V_p \left(\frac{\tau_1}{\tau_2}\right) \tag{4.1}$$

This voltage is only used as a tool to show the effect of voltage duration as the resultant forces during the pulse ON period is a function of the fixed applied voltage. The relation between the duty cycle and effective voltage is shown in Table 4.2. For the PWM waveforms, the rise time of the high voltage was measured using an Agilent oscilloscope. The longest rise time, which is associated with the highest applied voltage, is determined to be 0.06ms, as shown in Figure 4.7. The rise time will have a negligible effect on the results as the time is 0.2% of the shortest pulse duration (29ms) used in the studies.

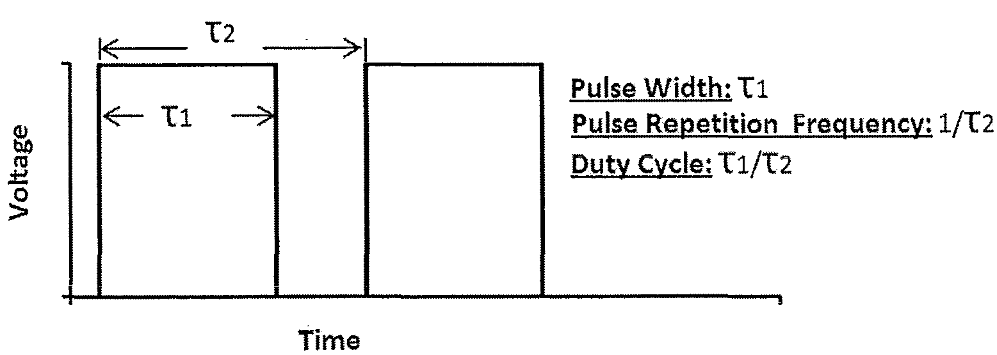

Figure 4.6 – Schematic of pulse waveform parameters

Table 4.2 – Effective voltage for each cycle duty for a pulse amplitude of 8kV.

Duty Cycle (%)	Effective Voltage (kV)
0	0.00
10	0.81
30	2.42
40	3.23
50	4.04
60	4.84
70	5.65
90	7.26
100	8.00

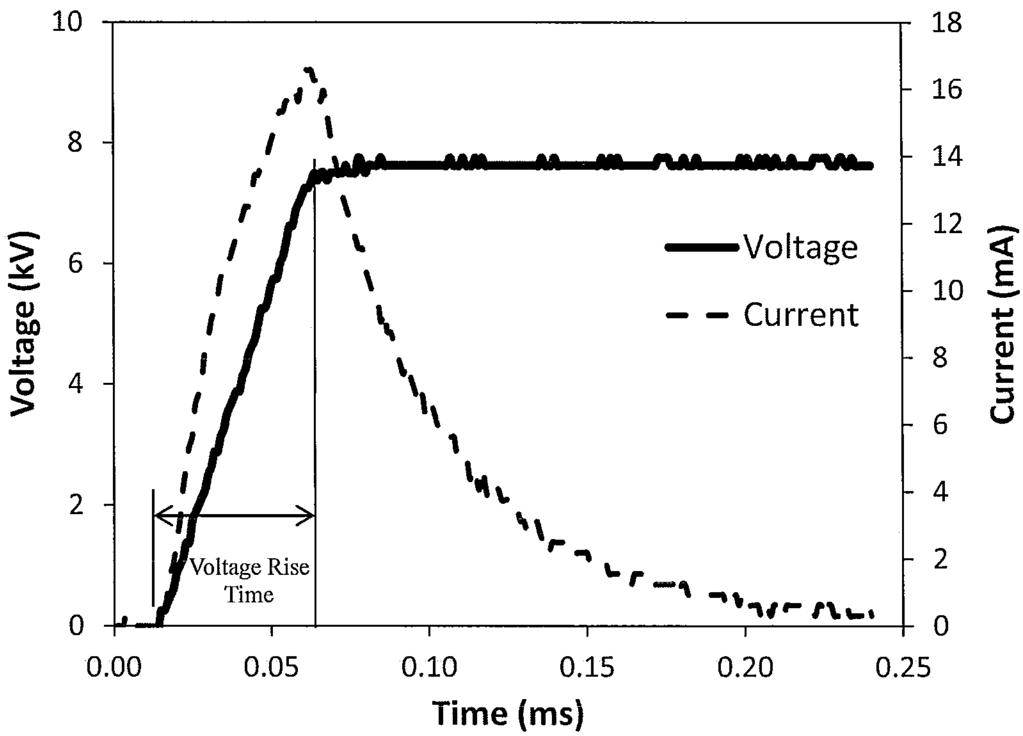

Figure 4.7 – Voltage and current characteristics for a 8kV step input.

Figure 4.7 also shows the current characteristics for a 8kV step input. Here the rise in the current is due to the change in the electric field (displacement current) and the current is observed to decrease over time to a constant value when maintaining the 8kV voltage. The constant value represents the conduction component of the total current and this component is measured to be in the order of microamps. The voltage-current rise time characteristics for a -8kV applied voltage is similar to the positive case except that the voltage and current is negative.

4.6 Data Reduction and Uncertainty

4.6.1 Heat Transfer Coefficient

The heat transfer coefficient in the heat exchange test section was determined by performing an energy balance between the refrigerant and water sides,

$$q''_W = q''_R \tag{4.2}$$

The heat extracted by the water side is determined by using the inlet and outlet water temperatures as

$$q''_W = \dot{m}_W c_{P,W} \Delta T_W \tag{4.3}$$

This heat extracted is assumed to be equal to the heat lost by the refrigerant side and this assumption results in a maximum error of 5%. The error was determined by comparing the heat extracted using Eq. (4.3) to the heat extracted in a single phase refrigerant flow using

$$q''_R = \dot{m}_R c_{P,R} \Delta T_R \tag{4.4}$$

The single phase experiment is conducted at approximately the same operating temperatures as the two-phase condensation experiments. The convective heat transfer of the two-phase refrigerant flow is computed as

$$q''_R = h_{avg}A_s\left(T_{R,Sat} - T_{S,avg}\right) \tag{4.5}$$

where the surface temperature is an average of all 12 thermocouple measurements along the test section. The average heat transfer coefficient is determined by substituting equation Eq. (4.2) and (4.3) into Eq. (4.5) to give

$$h_{avg} = \frac{\dot{m}_W c_{P,W} \Delta T_W}{A_s\left(T_{R,Sat} - T_{S,avg}\right)} \tag{4.6}$$

4.6.2 Heat Transfer Enhancement and Pressure Drop Ratios

The enhancement of heat transfer coefficient due to EHD, η_h, is determined by relating the heat transfer coefficient with EHD enhancement over the heat transfer coefficient in the absence of EHD and is given as

$$\eta_h = \frac{h}{h_o} \tag{4.7}$$

and similarly the pressure drop ratio, η_P, can be determined as

$$\eta_P = \frac{\Delta P}{\Delta P_o} \tag{4.8}$$

4.6.3 Two-Phase Flow Inlet/Outlet Conditions

The inlet vapour quality at the test section is determined by equating the heat added by the electrical heater to the temperature and latent heat increase of the refrigerant flow

$$q''_{elec} = q''_{R,T} + q''_{R,lv} \tag{4.9}$$

The heat added by the electrical heater and the temperature and latent heat increase of the refrigerant flow is given in Eq. (4.10), (4.11) and (4.12), respectively.

$$q''_{elec} = VI \tag{4.10}$$

$$q''_{R,T} = \dot{m}_R c_{P,R}\left(T_{R,sat} - T_{R,sub}\right) \tag{4.11}$$

$$q''_{R,lv} = \dot{m}_R h_{lv,R} x_R \tag{4.12}$$

Combining Eq. (4.9)-(4.12) and rearranging gives the inlet vapour quality

$$x_{R,in} = \frac{VI - \dot{m}_R c_{P,R}\left(T_{R,sat} - T_{R,sub}\right)}{\dot{m}_R h_{lv,R}} \tag{4.13}$$

The quality at the inlet can be determined by considering the heat removed from the refrigerant in the test section, Eq. (4.3). The outlet quality is given as

$$x_{R,out} = \frac{VI - \dot{m}_R c_{P,R}\left(T_{R,sat} - T_{R,sub}\right) - \dot{m}_W c_{P,W} \Delta T_W}{\dot{m}_R h_{lv,R}} \tag{4.14}$$

In all experiments, the change in quality between the test section inlet and outlet is less than 7%. This was accomplished by controlling the heat transfer in the shell-side of the heat exchanger. This criterion was used to ensure a minimal change in the flow pattern through the test section in the studies.

The experimental uncertainties are computed according to [Kline and McClintock (1953)] and given in Table 4.3. Details of the uncertainty calculations are provided in Appendix B. In addition, an energy balance of the entire system was also performed and this analysis is provided in Appendix C.

Table 4.3 – Experimental uncertainties.

Measurement	**Max. Uncertainty**
Temperature	± 0.22°C
Mass Flow Rate	± 4×10^{-5} kg/s
Pressure Drop	± 11 Pa (0 to 1.4kPa) ± 13 Pa (1.4 to 3.5kPa)
Calculated Quantities	**Max. Uncertainty**
Heat Flux	± 8.5%
Heat Transfer Coefficient	± 24%
Quality	± 4%

Chapter 5 – EHD in Single-Phase Flows

5.1 Single-Phase Electrohydrodynamics

The electrophoretic force is dependent on the free charges within the fluid and the origin of these charges is important in predicting the behaviour of the electroconvection phenomenon. As mentioned in Section 2.2.5, the charge injection phenomenon in dielectric fluid flows is still not well understood and at high electric field strengths the current is non-ohmic. Electrohydrodynamics in single-phase flows is less complex than two-phase flows because for an incompressible flow with small temperature gradients within the fluid, only the electrophoretic force component of the three EHD body force components must be considered. In this chapter, electric fields are applied to a single-phase flow to determine to determine the voltage-current characteristics, the charge injection characteristics and heat transfer enhancement potential. These results will provide an understanding of the importance of the electrophoretic force and charge injection on the flow redistribution, heat transfer enhancement and changes to the pressure drop when analyzing the two-phase EHD flows presented in Chapter 6.

5.2 Voltage-Current Characteristics in Single-Phase Flow

The current through a single-phase flow was measured for a range of potentials between -8kV to 8kV applied to the concentric rod electrode. The voltage-current results are shown in Figure 5.1 and the current is observed to be higher for a negative applied

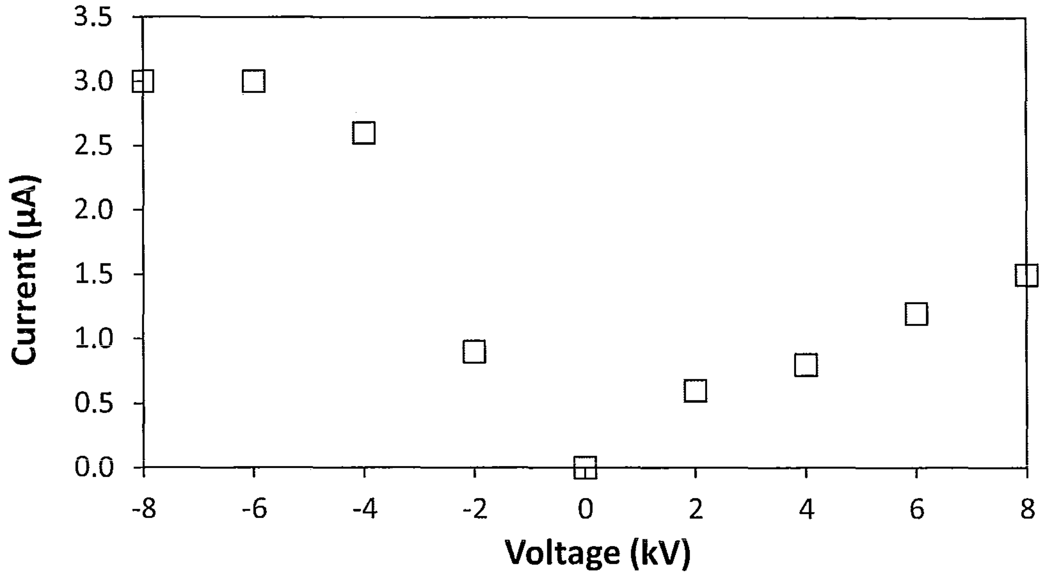

Figure 5.1 – Voltage-Current characteristics for a single-phase flow ($Re_l \approx 1740$) for applied positive and negative polarity DC voltages.

voltage. No heat was applied to the system during the tests and therefore the current is due to the mobility component of charge injection. In the tests, a flow was imposed (Re = 1740) such that charge accumulation at the interfaces would not be a concern. There are two possible explanations for the differences in the current due to polarity and each is dependent on the mechanism of the injection. In both explanations it is assumed that the charge injected is unipolar, which is often the case in dielectric liquids [Atten and Castellanos (1995) and Grassi (2005)]. The first possibility is that the charge injected is always negative charges from the negative electrode. For example if a negative voltage is applied to the electrode, negative charge will be injected from the electrode and if a positive voltage is applied to the electrode, negative charge will be injected from the outer tube. This prediction is generally valid as the charge injection is usually electrons injected at the cathode [Coelho (1979)]. This injection behaviour was also experimentally observed by Fujino and Mori (1989), as discussed previously in Section 3.4. As the electric field strength is highest at the inner electrode and decreases with increasing radius, as derived in Eq. (2.14), there will be a greater amount of charge injected when a negative high voltage is applied to the rod electrode and this will account for the differences in the current observed for negative and positive polarities. The second possible case for charge injection is that injection will always occur at the concentric rod electrode. For a positive high voltage to the electrode, positive charges will be injected and for a negative high voltage, negative charges will be injected. Although it is more common for negative charges to be injected from the negative electrode, this case may occur because the region of highest electric field strength is at the inner electrode. The differences in the observed current will be due to the differences in the ion mobility of positive and negative charges. The ion mobility in liquid R-134a can be approximated by relating it to the viscosity [Melcher (1981)]. The ion mobilities can be approximated as

$$\mu_{o+}=1.5\text{x}10^{-11}/\mu_l \tag{5.1}$$

and

$$\mu_{o-}=3.0\text{x}10^{-11}/\mu_l \tag{5.2}$$

The equations show that the negative ion mobility is two times larger than the positive mobility, thus possibly accounting for the differences in the observed currents. The ion mobility of the negative ions is calculated as $1.36\text{x}10^{-8}\text{m}^2/\text{Vs}$ and compares well with the value of $1.7\text{x}10^{-8}\text{m}^2/\text{Vs}$ for R-113 that was experimentally determined by Fujino and Mori (1989). The method of charge injection is important as the thermal boundary layer is more disturbed in the side opposite of charge injection, as mentioned in Section 3.4.

5.3 EHD Enhancement of Single-Phase Heat Transfer

The effect of applied voltage, voltage polarity and duty cycle on heat transfer enhancement was experimentally determined. Figure 5.2 shows the effect of applied voltage and Figure 5.3 shows the effect of the voltage polarity and duty cycle (also presented in terms of an average applied voltage) with a fixed pulse width of 58ms.

5.3.1 Effect of Applied Voltage and Polarity

The heat transfer results show that the there is a voltage threshold in which there is a spike in the heat transfer enhancement, as shown in Figure 5.2. The critical voltage for the onset of electroconvection can be predicted using Eq. (3.17). Using the electrical

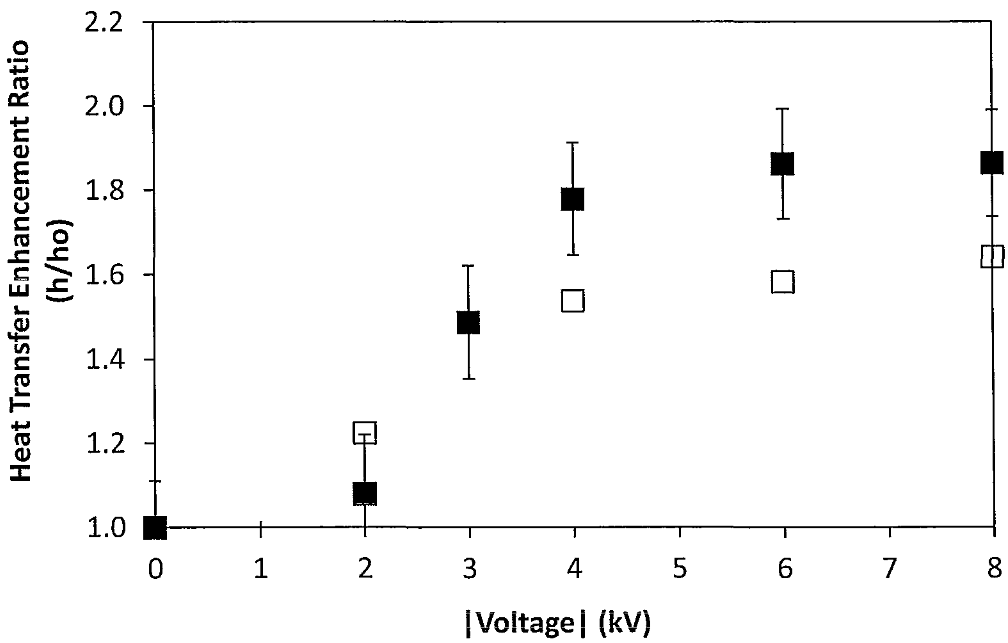

Figure 5.2 – Effect of applied voltage on the heat transfer enhancement ratio in a single-phase flow (Re ≈ 1760) for a □ positive and ■ negative applied voltage.

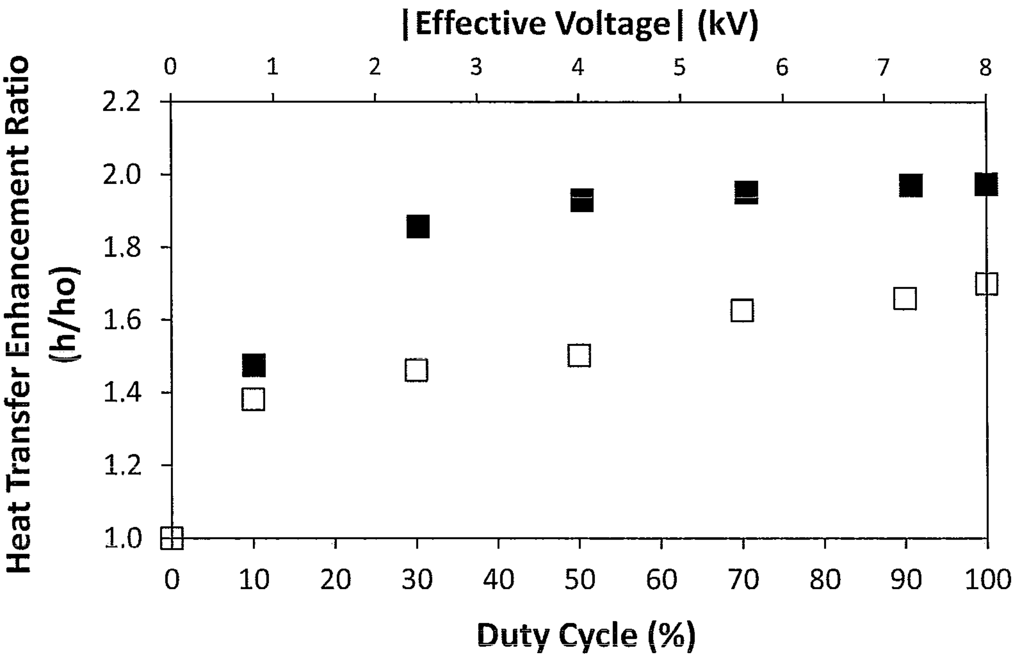

Figure 5.3 – Effect of duty cycle or effective voltage on the heat transfer enhancement ratio in a single-phase flow (Re ≈ 1760) for pulse amplitudes of □ 8kV and ■ -8kV and a fixed pulse width of 58ms.

stability parameter equation, the critical voltage is determined to be 36V and therefore in all the voltage cases presented in Figure 5.2, the voltage will be sufficient in causing electroconvection. The effect of electroconvection on a convective flow can be examined by determining the EHD number (Ehd) and comparing it to Re^2. A comparison between Ehd and Re^2 is given in Table 5.1. The dimensionless analysis shows that at ~4kV, the ratio between Ehd/Re^2 is the same order of magnitude. Therefore, the increase in the heat transfer coefficient is due to the electroconvection becoming dominant over the fluid viscous forces. The heat transfer can be enhanced approximately 2x using a negative polarity and approximately 1.6x using a positive polarity. This substantial increase may

Table 5.1 – EHD and Reynolds number for different applied voltages.

a) Positive voltages

Applied Voltage (kV)	Current (μA)	Reynolds Number	EHD Number	Ehd/Re^2
0	0	1681	0	0
2	0.6	1725	1.63×10^6	0.55
4	0.8	1734	2.17×10^6	0.72
6	1.2	1691	3.27×10^6	1.14
8	1.5	1820	4.08×10^6	1.23

b) Negative voltages

Applied Voltage (kV)	Current (μA)	Reynolds Number	EHD Number	Ehd/Re^2
0	0	1681	0	0
-2	0.9	1725	2.45×10^6	0.84
-4	2.6	1734	7.15×10^6	2.34
-6	3.0	1691	8.28×10^6	2.55
-8	3.0	1820	8.29×10^6	2.76

be a result of the laminar flow (Re $\approx$ 1760) being close to the transition point to a turbulent flow (Re ~ 2100) and the EHD forces may cause an instability that trips the flow to a transitional turbulent flow or that the EHD secondary motions enhance the flow similarly to that of turbulent motions. Current limitations in the flow meter range prevent further experimentation with lower Reynolds number flow.

The differences in heat transfer enhancement for positive and negative polarity is dependent on the method of charge injection considered (See Section 5.2). If we assume that only negative charges are injected, a greater amount of charge will be injected if the negative voltage is applied to the central electrode than if positive voltage is applied. Greater charge injection will occur in the regions of high electric field strength and the electric field strength is highest in the regions close to the central electrode, which was determined in Section 2.2.3. This explains the higher current observed in the case of negative polarity. Also as the electrophoretic force is dependent on the charge density, this will have a direct effect on the strength of the electroconvection and the enhancement of heat transfer. In addition, the increase in heat transfer enhancement also occurs for negative voltage at the central electrode because the thermal boundary layer on the side opposite to that of the charge injecting electrode is more greatly disturbed, as previously discussed in Section 3.4. Therefore, all the experimental findings are consistent with this charge injection model. This charge injection model is schematically shown in Figure 5.4.

The second method of charge injection is that charge injection only occurs at the central rod electrode and the charges are of the same polarity as the applied voltage. In this case, the difference in the observed current is a result of the differences in the estimated ion mobility of negative ($1.36\text{x}10^{-8}m^2/Vs$) and positive ions ($6.8\text{x}10^{-9}m^2/Vs$). However, one drawback of this charge injection model is that lower ion mobility results in a greater transfer of momentum to the fluid and therefore a greater secondary motion [Paschkewitz (2000)]. The fact that negative polarity exhibits higher heat transfer enhancement contradicts this theory and is one indication that this is not the method of charge injection in the experiments.

5.3.2 Effect of Duty Cycle and Polarity

Figure 5.3 shows the impact of increasing duty cycles on the heat transfer enhancement in single-phase flows. A positive and negative 8kV pulse was used in the experiments and the heat transfer enhancement plateaus for duty cycles greater than 30%.

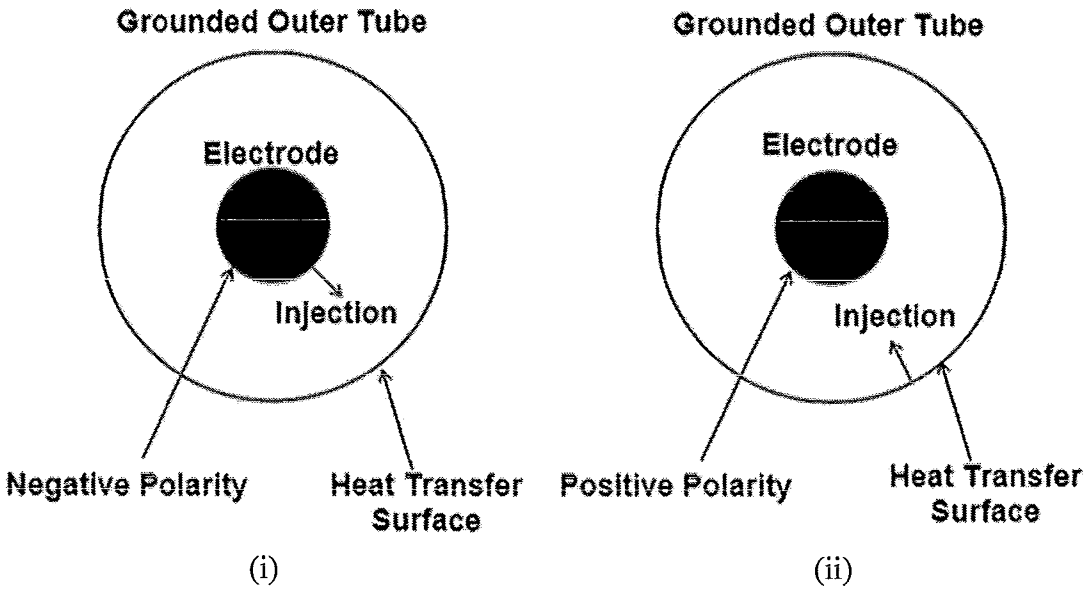

Figure 5.4 – Charge injection model in a tube with a concentric rod electrode for a (i) negative applied voltage and (ii) positive applied voltage assuming unipolar negative charge injection.

Once again, a higher enhancement was observed for with negative polarity. Figure 5.5 shows a comparison of the results in Figure 5.2 and Figure 5.3. In this figure, the effect of applying a continuous DC voltage versus a pulsed voltage for various duty cycles, presented as an effective voltage (see Section 4.5), is shown. The results show that the method of applying the high voltage has an effect on the heat transfer enhancement. For example, applying a +2kV DC voltage to the flow results in an enhancement of approximately 1.2x and applying a +8kV pulse at a duty cycle of 10% (V_{eff} = 0.8kV) results in an enhancement of approximately 1.4x. These results show the importance of the pulse amplitude on heat transfer enhancement and that the application of the EHD in pulses may yield results similar to that of a continuous application of EHD for lower effective voltages.

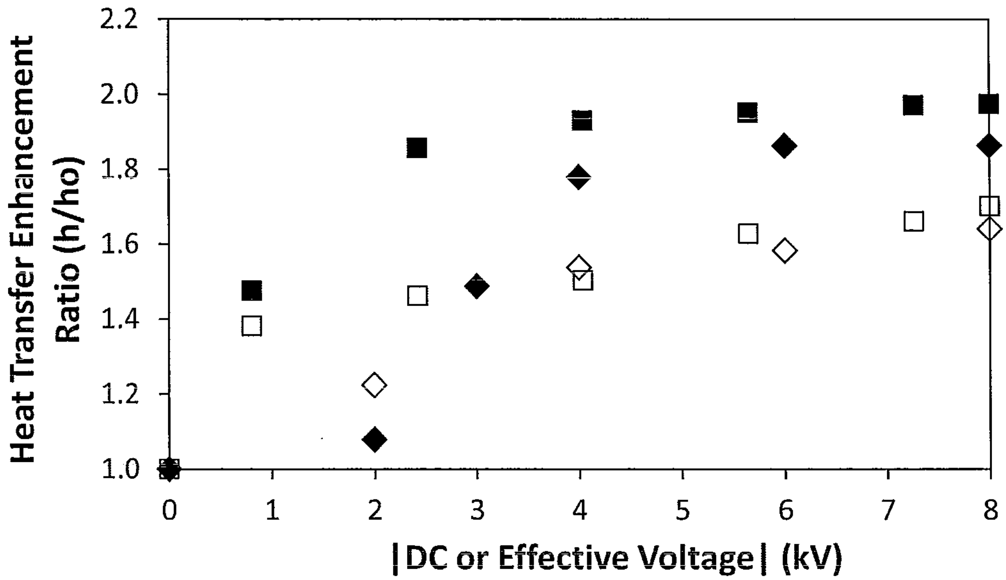

Figure 5.5 – Comparison of the heat transfer enhancement in a single-phase flow (Re ≈ 1760) between a continuous ◊ positive and ♦ negative polarity DC voltage and a pulse voltage of □ 8kV and ■ -8kV with a fixed pulse width of 58ms.

5.4 Summary of Single-Phase EHD Results

The effect of the voltage amplitude and polarity on the charge injection and heat transfer enhancement was experimentally determined. The results show that the charge injection mechanism in this particular heat exchange system is the injection of negative charge from the negative electrode. An understanding of the charge injection method in this particular geometry will be essential in understanding the physical mechanisms of the various flow structures that may be produced when EHD is applied to a two-phase flow.

Chapter 6 – Two-Phase Flow Redistribution using EHD

6.1 Two-Phase EHD Flow Redistribution

The use of EHD to redistribute the liquid and vapour phases in a two-phase flow is complex because the transient EHD flow patterns differ from those at steady state. As mentioned in Chapter 2 and Chapter 3, the heat transfer and pressure drop is highly dependent on the distribution of the liquid and vapour phases in the flow and an understanding of all the various EHD flow patterns is therefore a requirement in the design of an EHD heat exchanger. In this chapter, the various flow structures that may be developed as a result of EHD for a range of mass flux and quality will be investigated. In addition, a study into sustaining these flow structures during steady state using pulse width modulated high voltage waveforms is also presented and discussed. In all mass flux and quality combinations investigated, the initial flow pattern in the absence of EHD is a stratified/stratified wavy flow where gravity has a dominant role in establishing this flow pattern. The EHD effect was investigated for an initially stratified/stratified wavy flow pattern because the heat transfer enhancement using electric fields was determined to be the greatest for gravity dominated flows [Gidwani et al. (2002)].

6.2 EHD Flow Structures

In this section, the various flow structures that are observed at the flow visualization test section by applying high voltage to the flow using various pulse waveforms are presented. There are three types of EHD flow structures observed, which are twisted liquid cones, twisted liquid columns and entrained droplets.

6.2.1 The Twisted Liquid Cone EHD Flow Structure

An investigation into the twisted liquid cone transient flow pattern was first presented by Sadek (2009), who visualized the effect of a +8kV step input on a stratified wavy flow. Sadek visually observed the development of these twisted liquid cone flow structures and their decay over time. Experiments were performed to reproduce these flow structures and images of the twisted liquid cones, captured using a high speed camera, are shown in Figure 6.1. Figure 6.1 shows that during the initial application of high voltage, extraction of the liquid from the lower liquid stratum towards the rod electrode occurs due to the EHD body force. Once the liquid encompasses the electrode, the liquid is pushed radially outward in the form of twisted liquid cones. The rejection of liquid is due to the changes in the electric field strength distribution once the liquid completely surrounds the electrode [Cotton (2003)] and also on the charge distribution within the liquid phase. These liquid cones are present in all radial directions, as shown in Figure 6.1(f), where they are observed to bridge the gap between the electrode and tube wall at the channel sides. The twisted liquid cone is a transient phenomenon as they decay over time and are not observed during the 8kV steady-state flow pattern, as shown

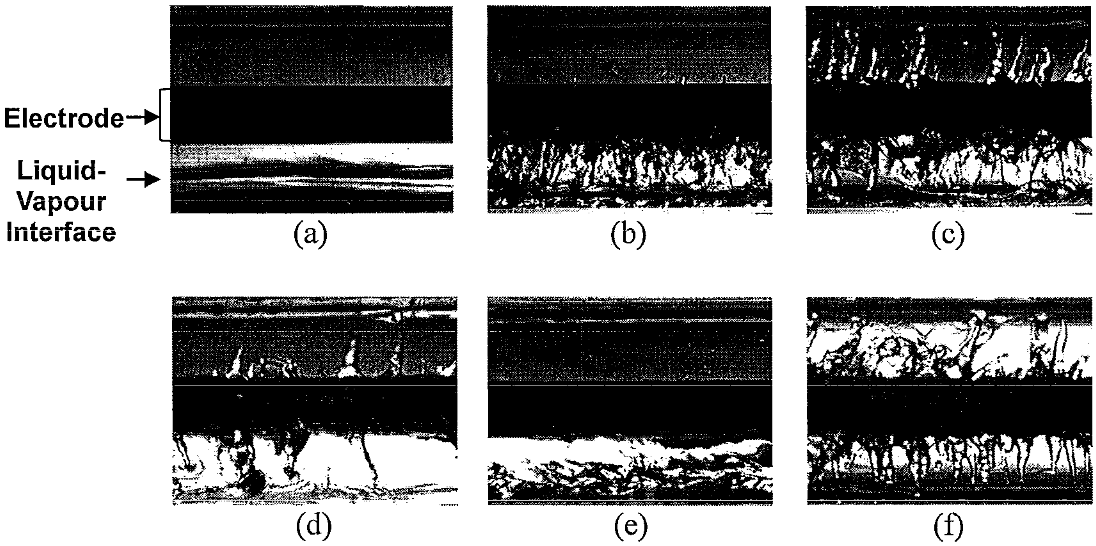

Figure 6.1 – Side profile images of a) the flow pattern in the absence of EHD, of the twisted liquid cones after applying a +8kV pulse for b) 29ms, c) 58ms, d) 115ms, e) 520ms and f) top-down view of the twisted liquid cones after 58ms.

in Figure 6.1(e). The twisted liquid cone flow structures are of interest because they exhibit characteristics favourable to the enhancement of heat transfer, such as a considerable bulk mixing of the fluid, liquid extraction from the heat transfer surface and into the central core, and an increase in the interfacial area.

The development of the twisted liquid cone structures is dependent on both the electrophoretic and polarization forces. The electrophoretic force is important because the flow patterns with a positive applied voltage differ from a negative applied voltage (negative voltage flow patterns discussed in Section 6.2.2). If the polarization forces dominate over the electrophoretic force then there would be no difference in the flow patterns due to polarity. A hypothesis in the development of the twisted liquid cones from a stratified two-phase flow is proposed based upon the experimental findings and assuming the charge injection method discussed in Section 5.2 for single-phase EHD flows, where charge injected is always negative ions from the negative electrode. The steps in the development of the twisted liquid cones are as follows

i. ***Step 1: Liquid Extraction***
- Positive high voltage is applied to the central rod electrode
- Liquid from the lower liquid stratum is extracted towards the electrode due to higher electric field (dielectrophoretic force) (See Appendix D)
- Negative charge injection into liquid bulk from outer tube

ii. ***Step 2: Liquid Surrounds Electrode***
- Liquid completely surrounds electrode
- Negative charges accumulate on electrode surface as the liquid contacts the rod electrode

iii. ***Step 3: Liquid Repulsion***
- Liquid repulsed from electrode towards outer tube due to higher electric field in vapour region (dielectrophoretic force) (See Appendix D)
- Negative charges opposes repulsion due to attraction towards positive polarity electrode (electrophoretic force)
- Twisted liquid cone flow structures bridge gap between electrode and tube

iv. ***Step 4: Steady State***
- Balance between dielectrophoretic and electrophoretic forces is achieved
- Lower liquid stratum decreased in thickness, electrode is surrounded by liquid (inverse annular flow)
- Twisted liquid cones no longer present
- Occasional bridging of liquid from bottom stratum to electrode due to charge accumulation in the lower stratum

The various steps in the development are shown in Figure 6.2. In Step 1, the liquid is extracted towards the electrode because of the higher electric field strength in the vapour region near the electrode and in Step 3, the electric field strength is higher outside the liquid surrounding the electrode and the liquid will be repulsed off the electrode. The electric field strengths for these two flow distributions were determined by a numerical analysis (Appendix D). The method of charge injection is important as the liquid conical shape is a result of the electrophoretic force restraining the flow onto the electrode.

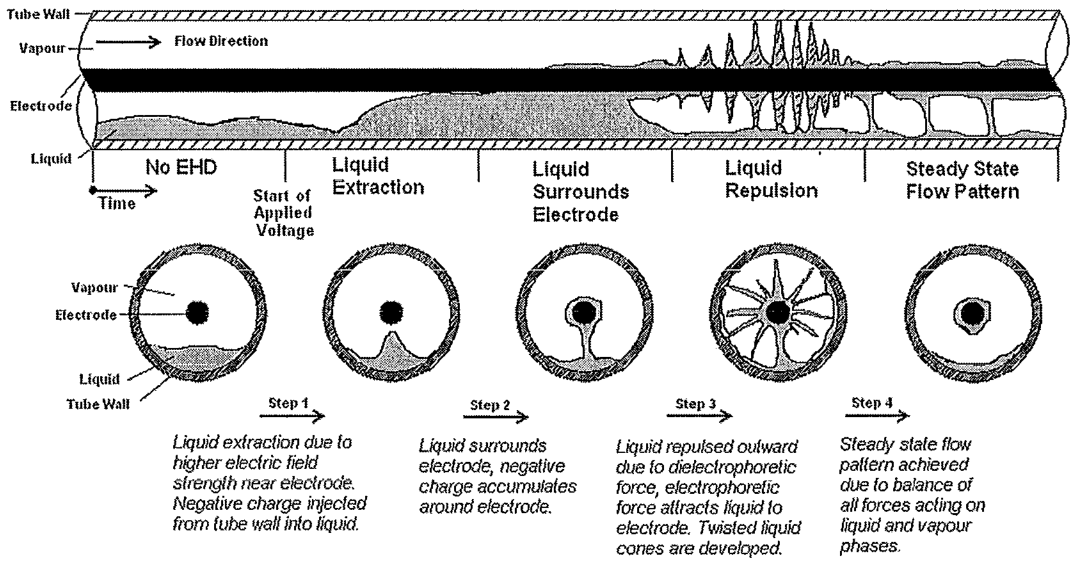

Figure 6.2 – Illustrative representation of the various steps in the development and decay of the twisted liquid cone flow structures.

6.2.1.1 Effect of Pulse Width and Duty Cycle on Sustaining Twisted Liquid Cones

Pulse width modulated waveforms were applied to attempt to sustain the twisted liquid flow patterns during the pulse ON period since the flow structures decay during continuous application of high voltage. The experiments were performed for a range of duty cycles to determine the suitable pulse OFF period, or relaxation time, required to sustain the transient flow patterns during the pulse ON period. The pulse width used in this investigation is 58ms, since the transient analysis in Section 6.2.1 showed that at this time the density of twisted liquid cones is the highest and this time is also sufficient for the twisted liquid cones to fully develop and bridge the gap between the electrode and tube wall.

Representative images of the flow patterns at the applied voltage of +8kV, mass flux of 55kg/m^{2}s, average quality of 50% and for various duty cycles is presented in Figure 6.3. For each image set in Figure 6.3, the applied pulse waveform is shown and the instance in which each image is taken is labeled on this waveform. The images for Figure 6.3(i)-(iii) are labeled as the percentage of the total period of the waveform, where the start of the waveform (0%) is the instance the pulse is applied. The images in Figure 6.3(iv) are labeled according to the time between images, since a continuous voltage is applied. At a duty cycle of 10% the liquid is extracted from the liquid stratum towards the electrode and the twisted liquid cones develop off the electrode (Figure 6.3(i)(c)). As the duty cycle increases above 10% there is a decrease in the number of twisted liquid cones. This decrease was originally believed to be a result of an insufficient pulse OFF period where the flow does not return to its initial condition of a stratified/stratified wavy flow (Figure 6.3(a)). Figure 6.3(a) shows the presence of entrained droplets in the lower core of the channel and the flow pattern is not stratified. It is later shown in Section 6.2.3 that the development and decay of the twisted liquid cone flow structures is entirely dependent on the charge distribution within the flow and independent of the initial flow distribution. The pulse OFF period allows for the charge to relax from either the electrode surfaces or the liquid-vapour interfaces and also any charge accumulated in the phases will be swept away with the flow. From the experimental observations, the pulse OFF time required such that the twisted liquid cones are observed during the pulse ON period is estimated from the flow visualization images to be 520ms. This pulse OFF time is less

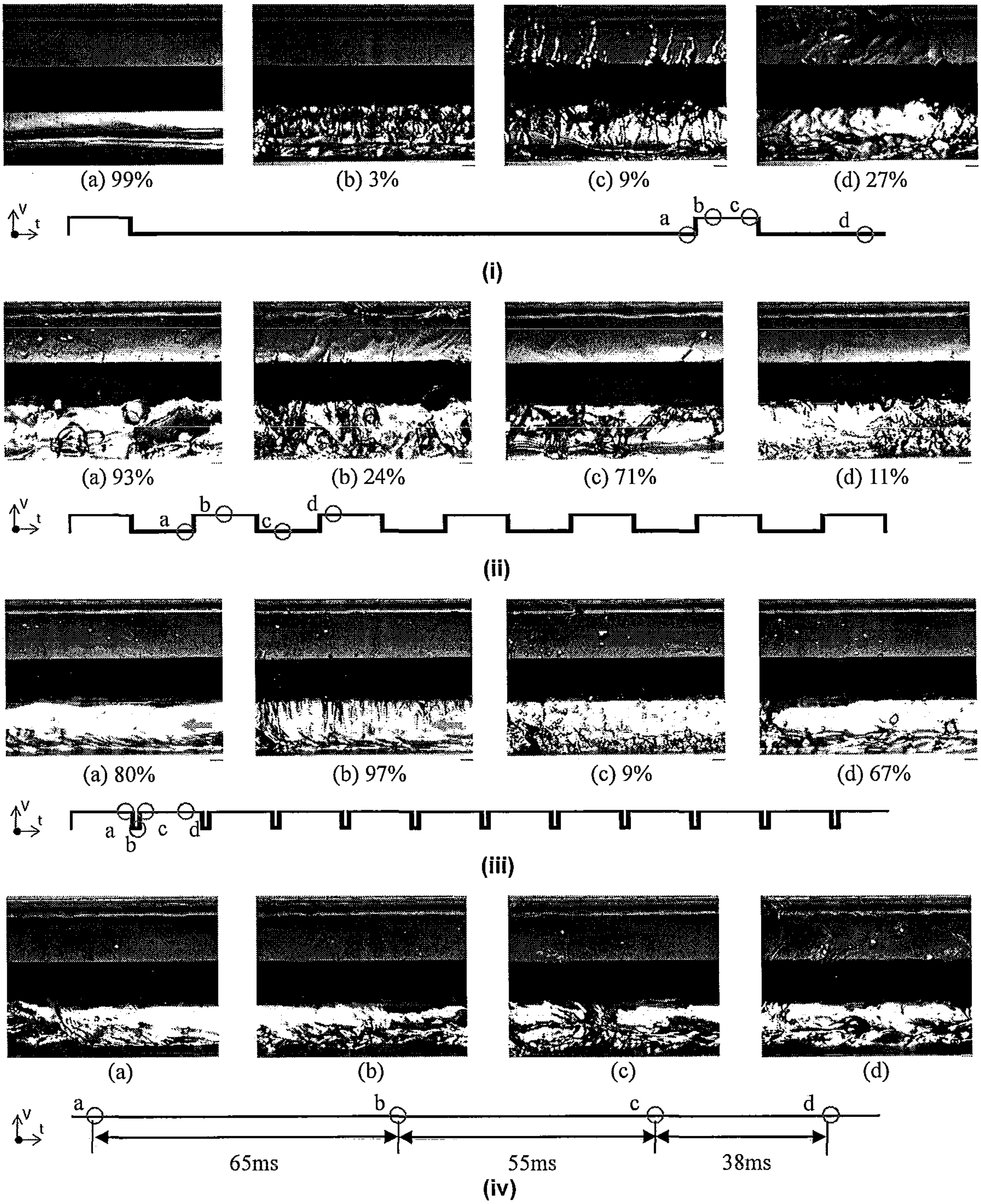

Figure 6.3 – Side profile images of the flow pattern for a pulse width of 58ms, average quality of 50% and a duty cycle of (i) 10%, (ii) 50%, (iii) 90% and (iv) 100% (DC) for a applied voltage of +8kV.

than the charge relaxation time (1.48s) determined in Section 3.5.2. The charge relaxation time does not consider the convection of a fluid and may be the reason that a pulse OFF time of 520ms was determined to be sufficient for the charge to relax from the interfaces in this investigation.

For duty cycles greater than 40%, although very few twisted liquid cones are observed, liquid extraction onto the concentric electrode still occurs due to the EHD forces. For duty cycles between 50-70%, large liquid droplets entrained beneath the electrode are observed (Figure 6.3(ii)(a)). The presence of entrained droplets indicates that the area below the electrode is vapour and that the liquid stratum below the electrode has decreased in thickness. For very high duty cycles such as 90% and 100%, large entrained droplets and twisted liquid cones are not present. A wavy liquid interface is observed on the lower section of the electrode as seen in Figure 6.3(iii)(a)(d) and Figure 6.3(iv)(b)(d). This suggests that the liquid has been extracted towards the electrode and that the electrode is completely surrounded by liquid (ie. inverse annular flow). This is confirmed in Figure 6.3(iii)(b) where the pulse is off and liquid is observed to be dripping down from the electrode. The pulse off period is short enough at a duty cycle of 90% that this liquid is quickly re-extracted towards the electrode and liquid droplets are formed from the tips of the dripping liquid during this sudden re-application of the pulse. These droplets are smaller in diameter than the droplets observed at lower duty cycles. A summary of the distinct flow pattern features for the high voltage pulses at a pulse width of 58ms and at a mass flux of 45 or 55kg/m^{2}s is presented in Table 6.1

Table 6.1 – Flow pattern features for a mass flux of $45kg/m^2s$ or $55kg/m^2s$ and average quality of 50%.

Duty Cycle	EHD Induced Flow Pattern Features
10%	- Large number of twisted liquid cones develop off center electrode during application of high voltage - Off period sufficient for flow to return to the initial stratified flow
30-40%	- Less twisted liquid cones than at 10% duty cycle - Twisted liquid cones are more frequent than 10% duty cycle due to shorter OFF period - Occasional large entrained droplets below concentric electrode
50-60%	- Less twisted liquid cones than those observed at lower duty cycles - Large entrained droplets observed below concentric electrode
70%	- Occasional large entrained droplet below concentric electrode
90%	- No twisted liquid cones - Small droplets ejected from center electrode during pulse OFF period
100% (DC)	- No twisted liquid cones - Small entrained droplets observed - Wavy liquid interface surrounding concentric electrode

The pulse width is an important parameter because it determines the flow pattern. For example, in Figure 6.3(i)(c), the twisted liquid cones were observed to have fully developed near the end of the 58ms pulse width. The effect of a pulse width of 29ms and 115ms on the flow pattern is shown in Figure 6.4. For a pulse width of 29ms, the twisted liquid cones do not have sufficient time to fully develop. This is apparent in Figure 6.4(i)(d), where the liquid is still being extracted towards the electrode near the end of the pulse. At a pulse width of 115ms, the twisted liquid cones are active for a longer period of time when compared to the 58ms case previously discussed, as shown in Figure 6.4(ii). A comparison of images (c) and (d) in Figure 6.4(ii) shows that the number of twisted liquid cones begins to decrease the longer the pulse is applied, which is expected because the twisted liquid cones are not observed for a continuous DC voltage. The twisted liquid cones completely decay approximately 365ms after application of the pulse voltage.

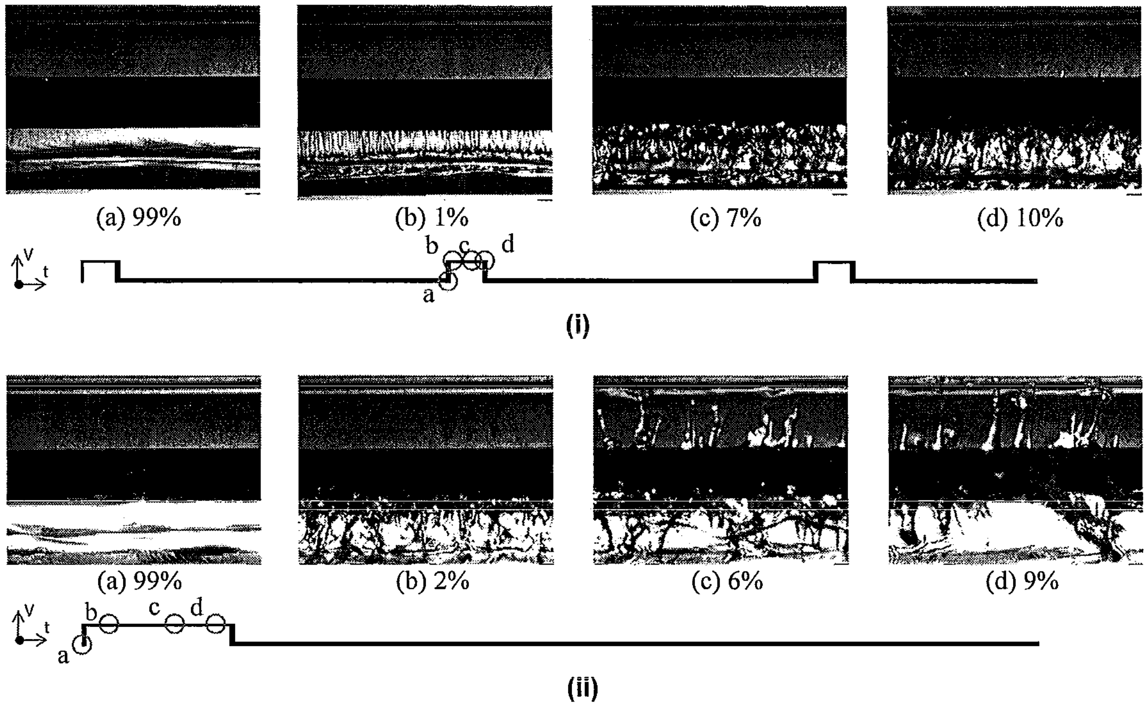

Figure 6.4 – Side profile images of the flow pattern for a average quality of 50%, duty cycle of 10%, mass flux of 55kg/m^{2}s and a pulse width of (i) 29ms, and (ii) 115ms.

The phase redistributions described in Table 6.1 differs when the mass flux is increased and the effect of EHD is less pronounced. For example, at a mass flux of 110kg/m^{2}s, the flow structures that are developed due to EHD are very quickly broken up by the high liquid and vapour velocity and the liquid is then washed towards the outer tube, as shown in Figure 6.5. In this case, the increase in the liquid-vapour shear has an influence on the EHD flow pattern. The influence of electric body forces on a two-phase flow to the inertia of the flow for different flow rates can be estimated by comparing the dimensionless Masuda number, Eq. (3.14), to the square of the Reynolds number, Eq. (3.10)), where EHD is significant when Md ≥ Re^2. The electric field strength used to solve Eq. (3.14) is estimated from numerical simulations [Appendix D] and the

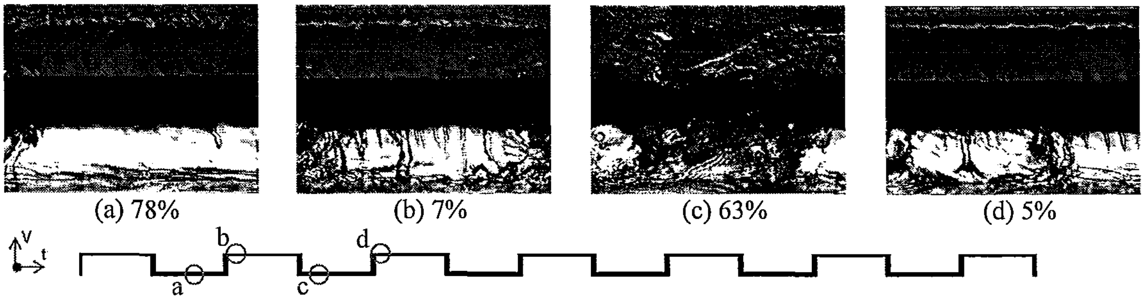

Figure 6.5 – Side profile images of the flow pattern for a pulse width of 58ms, average quality of 50%, duty cycle of 50% and a mass flux of 110kg/m^{2}s.

characteristic length is taken as the distance between the electrode and grounded tube. The Masuda number for an 8kV pulse is 1.0x10^8 and the Reynolds number is 1745, 2135 and 4272 for a mass flux of 45, 55 and 110kg/m^{2}s, respectively. The results show that for a mass flux of 45 or 55kg/m^{2}s, Md > Re^2 and for a mass flux of 110kg/m^{2}s, Md ~ Re^2. This indicates that the electric body forces dominate at a mass flux of 45 or 55kg/m^{2}s and inertia becomes as important as the electric body forces at a mass flux of 110kg/m^{2}s.

6.2.2 The Twisted Liquid Column Flow Structure

Twisted liquid column flow structures are shown in Figure 6.6 and are observed in place of the twisted liquid cone flow structures during the application of a negative polarity step voltage. These liquid columns differ from the liquid cones as they are thicker and appear to have a more uniform cross-section (Figure 6.6(a)) as opposed to the more conical structure of the liquid cones (Figure 6.1). The majority of the flow structures are in the lower portion of the tube, with some twisted liquid columns at the sides of the tube, as shown in Figure 6.6(b). The decrease in the number of flow structures at the upper portion of the tube may be a result of the increase gravitational

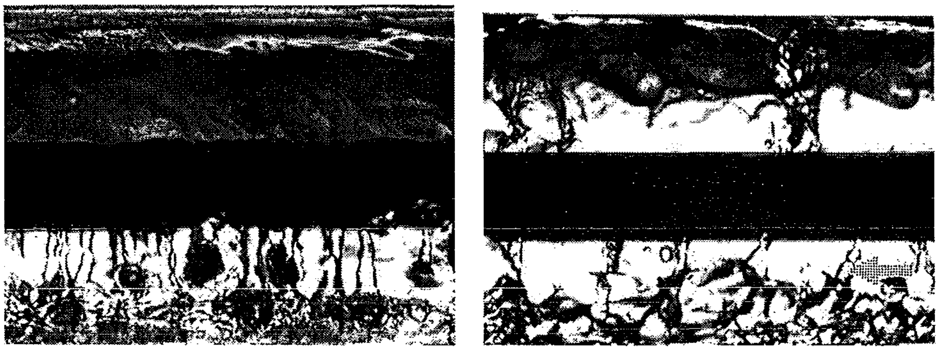

(a) (b)

Figure 6.6 – a) Side-view images of the twisted liquid columns after applying a -8kV pulse for 58ms and b) top-down view of the twisted liquid columns after 58ms.

forces on the flow structures as the column structures are larger than the liquid cones. In addition, as the twisted liquid columns appear to have a larger cross-sectional area than the twisted liquid cones, fewer flow structures are expected because of mass conservation of the liquid. The twisted liquid column flow structures are also a transient phenomenon as they are not observed during steady state.

A hypothesis in the development of the twisted liquid columns from a stratified two-phase flow is once again proposed based upon the experimental findings and assuming that the presence of charge is due to injection of negative ions from the negative electrode. The steps in the development of the twisted liquid columns can be described as

i. ***<u>Step 1</u>: Liquid Extraction***
- Negative high voltage is applied to the central rod electrode
- Liquid extraction to electrode due to higher electric field (dielectrophoretic force) (See Appendix D)

ii. ***<u>Step 2</u>: Liquid Reaches Electrode***
- Liquid surrounds electrode
- Negative charge injection into liquid surrounding electrode

iii. ***Step 3: Liquid Repulsion***

Liquid repulsed from electrode towards outer tube due to higher electric field in vapour region, negative charges assist repulsion due to electrophoretic force (See Appendix D)

- Twisted liquid column flow structures that bridge gap between electrode and tube later observed

iv. ***Step 4: Steady State***

- Balance between dielectrophoretic and electrophoretic forces is achieved
- Lower liquid stratum decreased in thickness, electrode is surrounded by liquid (inverse annular flow)
- Twisted liquid columns no longer present
- Occasional bridging of liquid from bottom stratum to electrode due to charge accumulation on the rod electrode

The various steps in the development of the twisted liquid columns are shown in Figure 6.7.

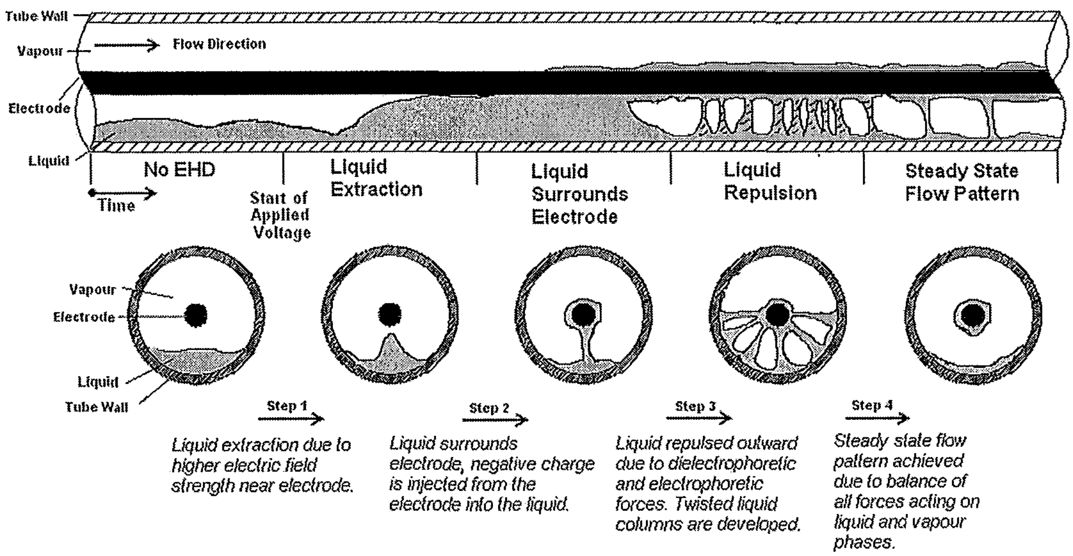

Figure 6.7 – Illustrative representation of the various steps in the development and decay of the twisted liquid column flow structures.

A review of the development of the twisted liquid columns and cones (Section 6.2.1) show that the main difference in the flow structures is due to charge injection. In the case of applying a negative voltage to the rod electrode, negative charge injection at the rod electrode assists in the repulsion of the liquid resulting in a liquid column. A result of the additional repulsion is a greater wetting of the tube walls. Applying a positive voltage to the rod electrode results in negative charge injection at the outer tube and an attraction of the liquid to the rod electrode. The consistency of the findings suggests that the method of charge injection assumed in this application is correct.

6.2.2.1 Effect of Duty Cycle on Sustaining Twisted Liquid Columns

A similar analysis using negative pulse width modulated waveforms was performed to determine the effect on the development of twisted liquid columns. The effect of using a negative applied pulse voltage for a range of duty cycles is shown in Figure 6.8. A -8kV pulse with a pulse width of 58ms was applied in all cases. At the low duty cycle, the presence of twisted liquid columns is observed, as shown in Figure 6.8(i)(c) and (ii)(c). As the duty cycle increases, the number of twisted liquid columns decreases and the inverse annular flow is once again present, as shown in Figure 6.8(iii) & (v).

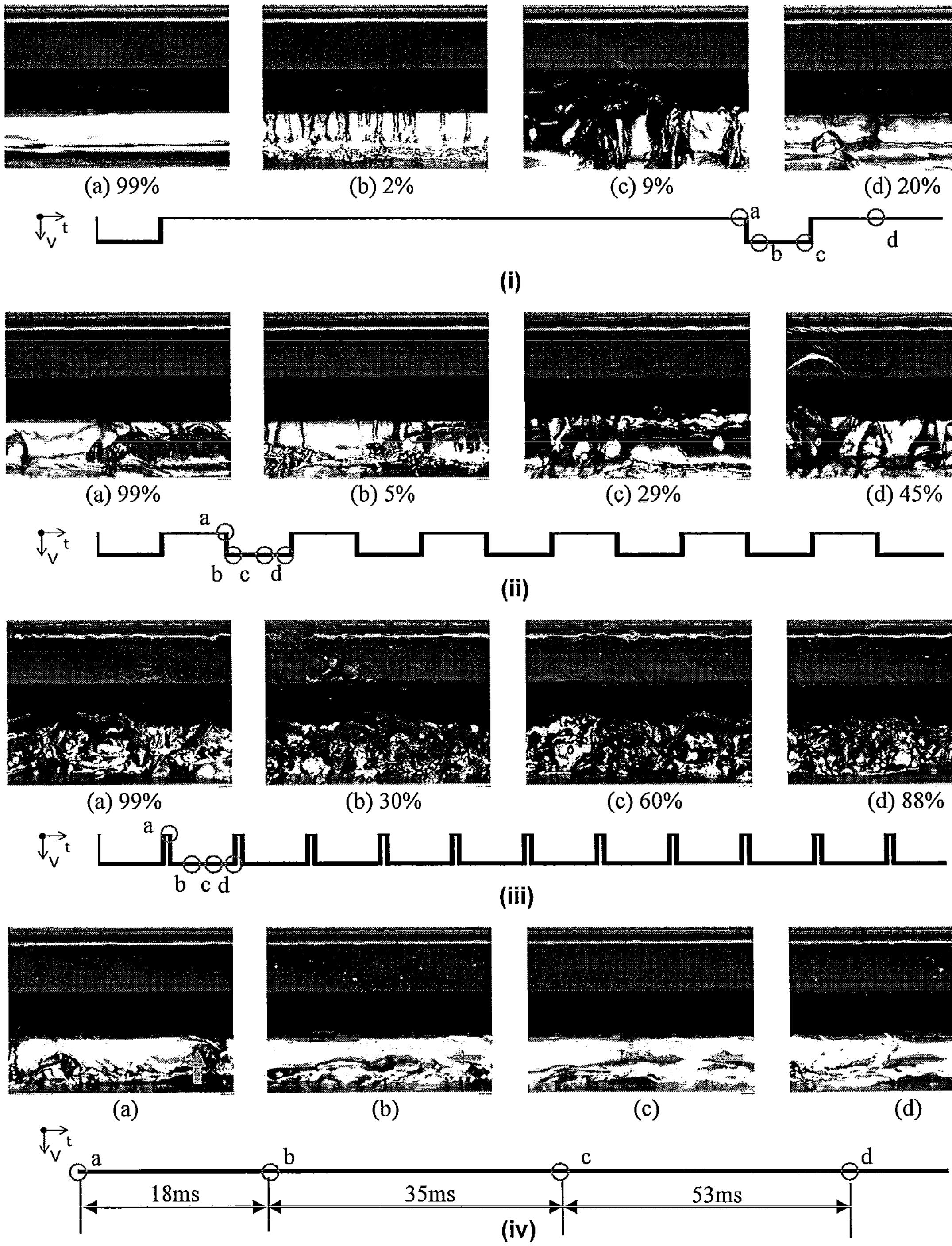

Figure 6.8 – Side profile images of the flow pattern for a pulse width of 58ms, average quality of 50% and a duty cycle of (i) 10%, (ii) 50%, (iii) 90% and (iv) 100% (DC) for a applied voltage of -8kV.

6.2.3 Twisted Liquid Cone and Column Flow Pattern

The use of single polarity pulse width modulated waveforms to sustain twisted liquid cone or column flow structures during the pulse ON period was successful for duty cycles below 50%. At higher duty cycles, the pulse OFF period is insufficient for the development of the liquid flow structures during the pulse ON period. The development of the twisted liquid cones or columns was determined previously to be dependent on the charge distribution and charge injection mechanism. In this section, an investigation into the use of both positive and negative pulses in a pulse width modulated waveform is investigated to determine its effect on the flow structures. These results will elicit the importance of the charge distribution on the development of the flow structures, as a switch in the polarity of the pulse should disrupt the charge distribution/accumulation and charge injection mechanism.

6.2.3.1 Effect of a Positive and Negative Pulses on Twisted Liquid Cones and Column Flow Structures

The effect of applying a 58ms positive pulse for 50% of the total period of the waveform followed immediately a negative pulse at a range of different pulse widths is shown in Figure 6.9, Figure 6.10 and Figure 6.11. In the figures, the pulses applied are +8kV and -8kV and the waveforms shown are for one period.

The application of a negative pulse immediately after a positive pulse shows that the twisted liquid cone structures are present during the positive pulse duration during steady state. Therefore, the development of the twisted liquid cones is highly dependent on the charge distribution within the fluid domain and not on the distribution of the liquid

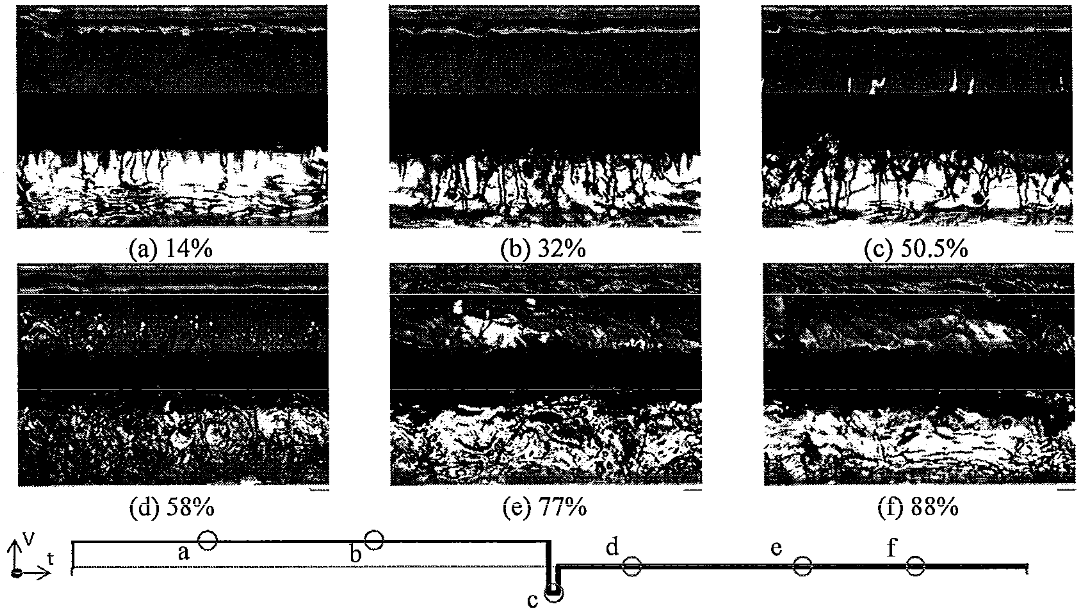

Figure 6.9 – Side profile images of the flow pattern for mass flux of 55kg/m^{2}s, average quality of 50% and a 50% positive pulse (pulse width of 58ms) followed by a 1% negative pulse (pulse width of 1.16ms).

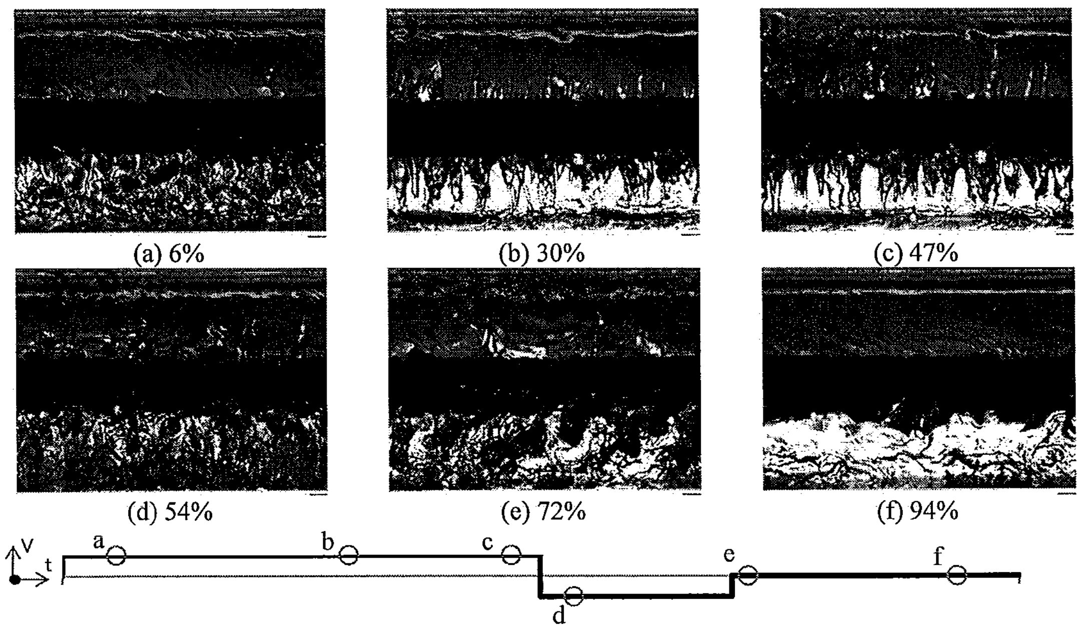

Figure 6.10 – Side profile images of the flow pattern for mass flux of 55kg/m^{2}s, average quality of 50% and a 50% positive pulse (pulse width of 58ms) followed by a 20% negative pulse (pulse width of 23.2ms).

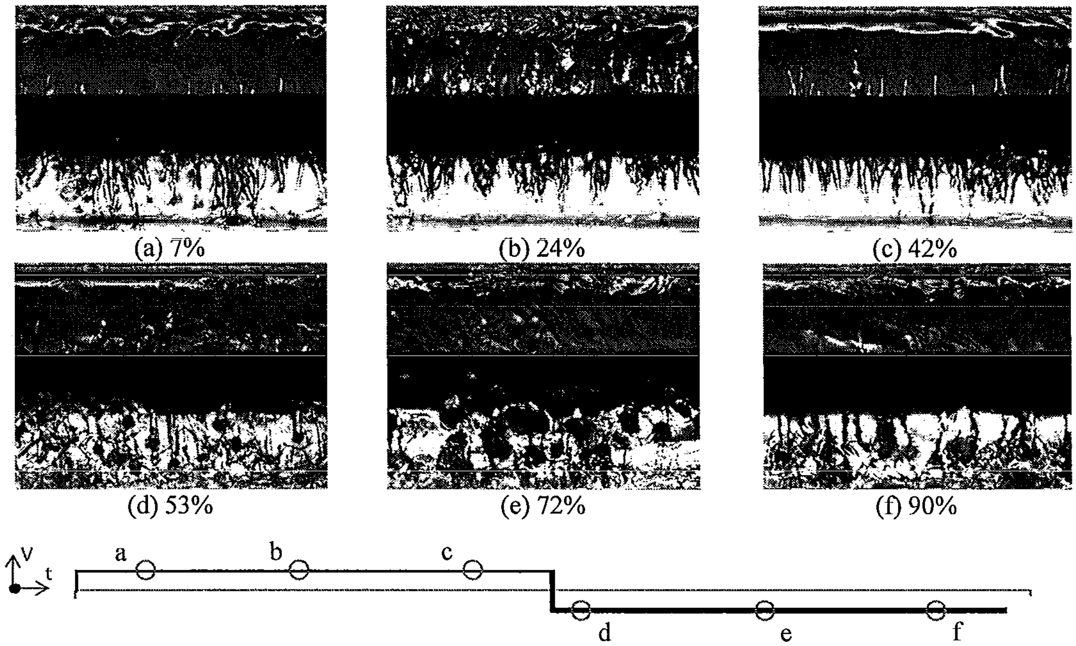

Figure 6.11 – Side profile images of the flow pattern for mass flux of 55kg/m^{2}s, average quality of 50% and a 50% positive pulse (pulse width of 58ms) followed by a 50% negative pulse (pulse width of 58ms).

and vapour phases before application of the positive high voltage. This is shown in Figure 6.11(f), where the flow is not stratified/stratified wavy before the application of the positive high voltage and twisted liquid cones are still observed after the positive high voltage is applied.

The application of negative pulse following a positive pulse results in the liquid phase surrounding the concentric electrode (i.e. twisted liquid cones) to be repulsed radially towards the outer tube, as shown in images (d) in Figure 6.9, Figure 6.10 and Figure 6.11. During the application of a negative pulse, the twisted liquid cones at the top section of the electrode are repulsed towards the top of the tube and are separated from the electrode (images (d) and (e) in Figure 6.11, Figure 6.10 and Figure 6.11). The twisted liquid cones on the side and bottom of the electrode are repulsed towards the outer tube but remain attached to the electrode becoming twisted liquid columns. A major difference between the observed flow patterns using both positive and negative pulses is that there appears to be a considerable wetting of the tube during the switch from a positive to negative pulse (especially at the sides of the tube), as shown in (e) and (f) in Figure 6.9, Figure 6.10 and Figure 6.11.

The number of twisted liquid cones developed during the positive pulse is determined by the negative high voltage pulse width. Comparing the flow patterns observed in Figure 6.9, Figure 6.10 and Figure 6.11, a larger negative pulse width results in more twisted liquid cones being developed during the positive pulse. This analysis also reveals that a pulse OFF period is not required to sustain the twisted liquid cone flow structures during the pulse ON period, as development of the EHD flow structures is dependent on the charge distribution and not on the initial distribution of the liquid and vapour phases. The results for a negative pulse followed by a positive pulse showed similar results, where the twisted liquid columns were sustained during the negative pulse and twisted liquid cones were observed during the positive pulse.

6.2.4 Enhanced Production of Entrained Droplets

The application of EHD also results in the enhanced production of entrained droplets in a two-phase flow, as seen in the work by Cotton (2009). An entrained droplet flow pattern is of interest because it is expected to result in an increase in heat transfer because of the decrease in the liquid thickness on the heat transfer surface by removing and entraining liquid into the vapour core. In Section 6.2.1, liquid droplets were observed at duty cycles between 30 to 90% with a 58ms pulse width, where large droplets were observed at the lower duty cycles and small droplets at the higher duty cycles. These results indicate that more frequent step changes in the voltage results in a greater production of entrained droplets. Therefore, it is expected that with smaller pulse widths, there will be a greater production of entrained droplets. The effect of applying small pulse widths is investigated in this section for various duty cycles to see the effect on the production of entrained droplets.

When small pulse widths (approx. 3-15ms range) were applied to a two-phase flow, a unique entrained droplet flow pattern is produced. This is shown in Figure 6.12 where the flow is extracted towards the central electrode and then liquid cones begin to develop from the electrode surface. Since the pulse width selected is small, the pulse is insufficient for the twisted liquid cones to develop. Immediately after the pulse ends, the tips of the twisted liquid cones separate and form droplets that become entrained in the vapour core. The separation of the tips into droplets is due to the dominance of surface tension once the EHD forces are removed. The method of droplet production was also observed in water [Raisin et al. (2010)] where high voltage pulses were applied to a liquid meniscus to stretch the fluid and upon removal of the voltage a liquid droplet was produced. The production of the entrained droplets can be described as a bursting process during the initial application of EHD, as the droplets appear to be bursting off from the twisted liquid cones. These droplets later coalesce to form larger droplets, as shown in the steady state entrained droplet flow pattern (Figure 6.13). The steady state flow pattern also shows that the majority of the droplets are in the lower portion of the channel, suspended in the vapour core. This is the flow pattern observed and described by Cotton (2009) as the oscillatory entrained droplet flow pattern. The droplets oscillate as they are being stretched due to the EHD forces during the pulse ON period, as shown in Figure 6.13(c).

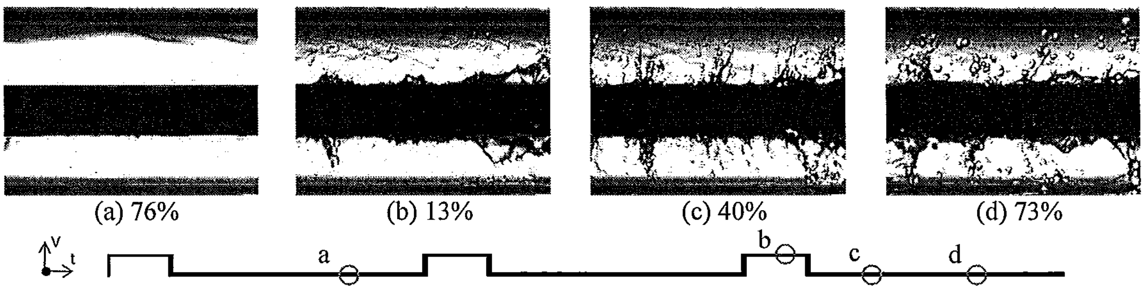

Figure 6.12 – Images from the top down of the production of entrained droplets during the initial application of a 3ms +8kV pulse at a duty cycle of 20%, mass flux of 45kg/m^{2}s and average quality of 50%.

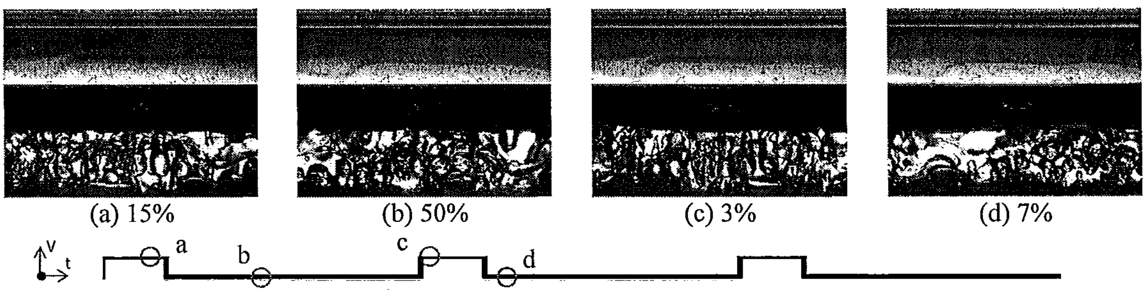

Figure 6.13 – Side profile images of the steady state entrained droplet flow pattern due to EHD for a 3ms +8kV pulse at a duty cycle of 20%, mass flux of 45kg/m^{2}s and average quality of 50%.

6.2.5 Effect of Duty Cycle on the EHD Entrained Droplet Flow Pattern

The effect of applying different duty cycles on the entrained droplet flow pattern is shown in Figure 6.14. This figures presents flow visualization images for duty cycles of 20%, 50% and 80%. At low duty cycles, Figure 6.14(a) shows that there is the largest number of entrained droplets. Figure 6.14(b) shows that as the duty cycle increases to 50%, the number of entrained droplets decreases, however the size of the droplets increases drastically due to the coalescence of smaller droplets. EHD has been proven to be capable of enhancing the coalescence of droplets [Raisin et al. (2009)] and this phenomenon is known as electrocoalescence. A further increase of the duty cycle to 80% results in the droplets once again decreasing in size and there is also a greater disturbance of the liquid in the lower stratum, as seen in Figure 6.14(c). The decrease in the droplet size at the 80% duty cycle can be attributed to the increase in time the EHD forces are active. During the EHD "ON" period, any existing bubbles become stretched vertically due to the EHD forces and at the high duty cycle these droplets may break up into multiple droplets.

(a) Duty Cycle 20% (b) Duty Cycle 50% (c) Duty Cycle 80%

Figure 6.14 – Side profile images of the steady state entrained droplet flow pattern due to EHD for a mass flux of 45kg/m^{2}s, quality of 50%, frequency of 60Hz and duty cycle of a) 20%, b) 50% and c) 80%.

6.3 Summary of Two-Phase Flow Redistribution using EHD

The results show that five different EHD flow patterns (twisted liquid cone, twisted liquid column, twisted liquid cone and column, entrained droplet and inverse annular flow) can be developed using various PWM waveforms. Details on the design of PWM waveforms to sustain the different EHD flow patterns during the pulse ON period of the waveforms were determined through a flow visualization study and an understanding of the physical mechanisms involved in the development of the various EHD flow structures. The importance of understanding the development of the EHD flow patterns is that the heat transfer and pressure drop performance of a two-phase flow depends on the flow distribution (See Section 2.3.2). Therefore it is expected that the various flow patterns presented in this chapter will all have different heat transfer and pressure drop characteristics. An understanding of these various flow patterns provides another means of enhancing or controlling the heat transfer and pressure drop performance in a heat exchanger using EHD. The heat transfer and pressure drop characteristics of the various EHD flow patterns is presented in the next chapter.

Chapter 7 – Effect of EHD on Convective Condensation Heat Transfer and Pressure Drop

7.1 EHD Flow Pattern Heat Transfer and Pressure Drop Characteristics

The heat transfer and pressure drop characteristics of the EHD flow patterns is expected to differ from a two-phase flow without EHD because of the redistribution of the liquid and vapour phases and the influence on the heat transfer surface. In this chapter, the effect of the twisted liquid cone, twisted liquid column, twisted liquid cone and column, entrained liquid droplet and inverse annular flow patterns on heat transfer and pressure drop are presented.

7.2 Heat Transfer and Pressure Drop Performance of Twisted Liquid Cones and Inverse Annular Flow

The heat transfer and pressure drop performance of each of the twisted liquid cone flow structures cannot be measured directly because they are transient in nature and therefore the various pulse waveforms and parameters presented in Chapter 6 are once again applied to the flow to indirectly determine the effect on heat transfer and pressure drop. The heat transfer and pressure drop measured is an average of the heat transfer and pressure drop of the pulse ON and pulse OFF flow patterns because the response time of the 0.5mm diameter thermocouples (approximately 300ms) [Omega (2004)] is insufficient to capture the heat transfer of the pulse ON period since the largest pulse width investigated is 115ms. For the case of a duty cycle of 100% (DC case), the heat transfer and pressure drop measured corresponds to an inverse annular flow pattern.

7.2.1 Effect of a Pulse Width and Duty Cycle on Heat Transfer and Pressure Drop for a Positive PWM Waveform

The heat transfer and pressure drop results for a mass flux of 55kg/m^{2}s, average quality of 50% and three different pulse widths are presented in Figure 7.1 and Figure 7.2. The error bars presented in Figure 7.1(i) are relatively large and there is a maximum uncertainty of 24% at a duty cycle of 100%. However, in all the experiments random data points were repeated (approx. 2 points per experiment condition) and in the case of a 100% duty cycle, this data point was repeated 4 times. The maximum discrepancy in the heat transfer results from the repeatability studies was within ±3.5%. In addition, in obtaining the experimental data for a range of duty cycle, the data points for each duty cycle were not taken in a linear manner. Therefore, the results suggest that the trends with the applied voltage shown are consistent and that hysteresis effects are negligible.

There is an increase in heat transfer for each duty cycle as the pulse width is increased from 29ms to 115ms. The effective voltage at each duty cycle (see Table 4.2) is equal for each of the different pulse widths and the enhancement of heat transfer is

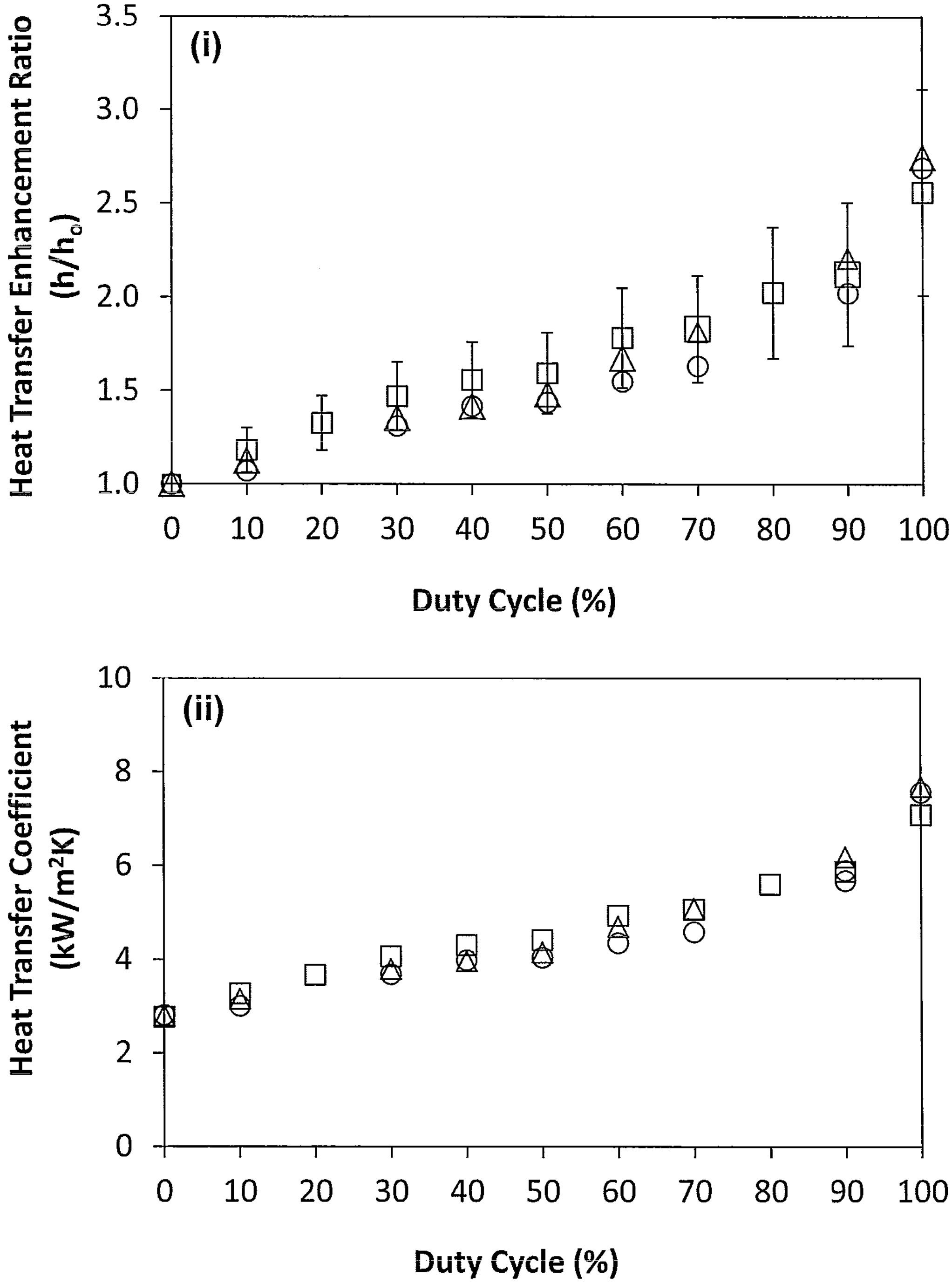

Figure 7.1 – Effect of duty cycle on the (i) heat transfer enhancement ratio and (ii) heat transfer coefficient for a mass flux of 55kg/m^{2}s, average quality of 50% and pulse width of ○29, Δ58 and □115ms.

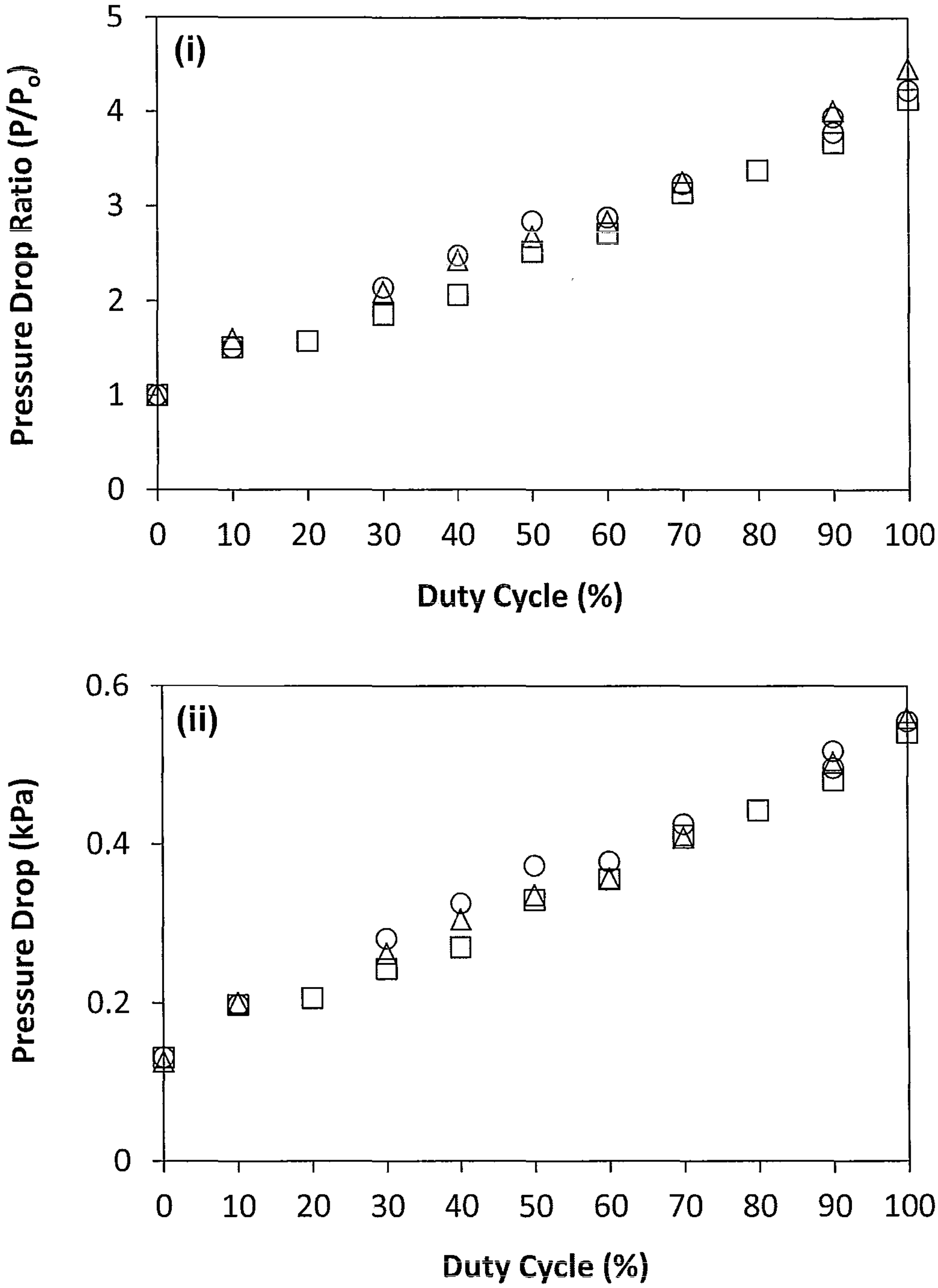

Figure 7.2 – Effect of duty cycle on the (i) pressure drop ratio and (ii) pressure drop for a mass flux of 55kg/m^{2}s, average quality of 50% and pulse width of ○29, Δ58 and □115ms.

attributed to the effect of the different pulse widths in sustaining the EHD flow structures. A larger pulse width results in a longer period that the EHD flow pattern is active and the number of transition cycles between pulse ON and OFF is also reduced. Fewer pulse cycles result in less time that the flow is transitioning from its initial flow pattern of a stratified/stratified wavy flow (or some intermediate flow pattern if the pulse OFF period is insufficient) to the EHD flow pattern, thereby improving performance by increasing the duration the higher heat transfer flow pattern is active.

The EHD transient flow patterns have a higher heat transfer than the initial stratified/stratified wavy flow pattern. This is because the redistribution of liquid due to EHD increases the condensation heat transfer coefficient by reducing the thermal resistance due to the liquid between the vapour and the heat transfer surface. This is shown in Figure 7.3, where the temperature at the bottom, sides and top of the tube is compared to the saturation temperature of the bulk refrigerant flow. According to Eq. (4.6), a greater temperature difference between the wall temperatures and the bulk refrigerant flow results in a higher thermal resistance. The results show that for the base case of no EHD (duty cycle 0%), the thermal resistance is highest at the bottom wall and lowest at the top wall. This is the expected heat transfer behaviour for a gravity driven flow (see Section 2.3.2.2). When EHD is applied, the thermal resistance is observed to decrease at both the bottom of the tube and also slightly at the top of the tube. The decrease is due to the flow redistribution and the extraction of liquid from the lower layer and into the central core because of the production of twisted liquid cones at low duty cycles (< 50%), the production of entrained droplets at moderate duty cycles (40-70%)

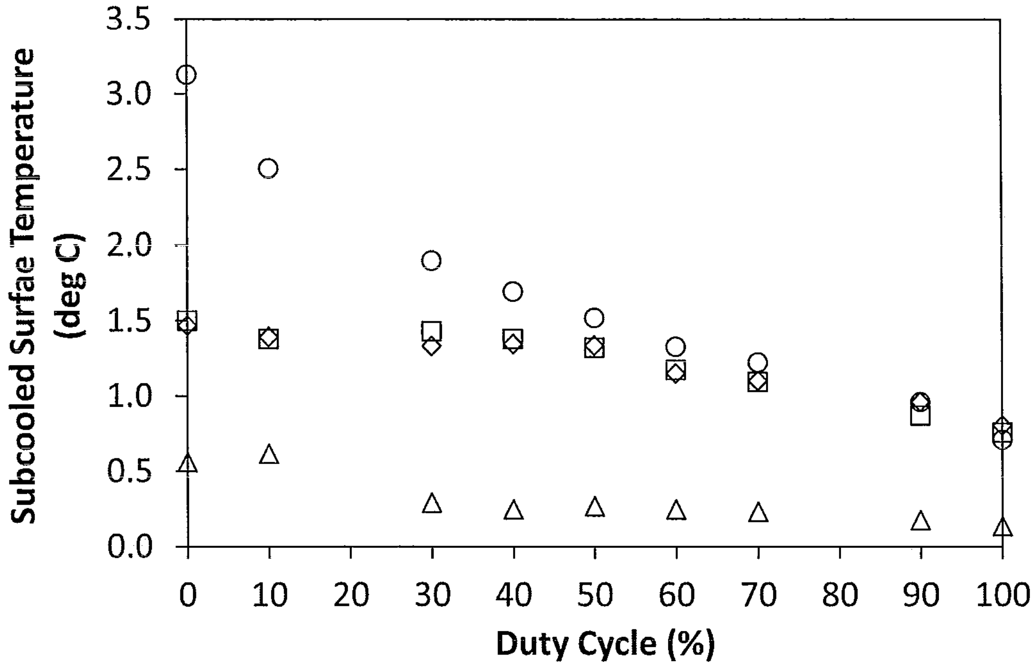

Figure 7.3 – Comparison between the tube wall and refrigerant bulk saturation temperatures for a mass flux of 55kg/m^{2}s, average quality of 50%, +8kV pulse, 58ms pulse width and a range of duty cycles.
Location of wall temperature measurements: Δ top and □, ◊ sides and ○bottom.

and liquid extraction onto the central electrode (inverse annular flow) at high duty cycles (> 90%). Measurements of the liquid extracted from the heat transfer surface into the central core were attempted using an ultrasonic technique. Limited success was found with this technique for the current experimental set-up and details of the analysis are presented in Appendix E.

An increase in the pressure drop was also observed because of the EHD flow structures. EHD flow structures, such as twisted liquid cones and entrained droplets, and liquid extraction onto the electrode result in a larger interfacial area, which thereby increases the shear between the liquid and vapour and the liquid and channel surfaces.

The results show that the pressure drop increases marginally for smaller pulse widths. The pressure drop increase at smaller pulse widths is once again attributed to the more frequent transitions between the EHD flow patterns and the flow patterns without EHD, resulting in more interactions between the liquid-vapour and liquid-electrode surfaces.

The effect of the different EHD transient flow patterns on the condensation heat transfer performance of a 50% quality flow at different mass fluxes is shown in Figure 7.4. At the lower mass flux (45 and 55kg/m^{2}s) the initially stratified flow is gravity dominated and at the higher mass flux (110kg/m^{2}s) the initial flow pattern is stratified wavy and the liquid and vapour shear will become more important. For a fixed pulse width of 58ms, the enhancement of heat transfer is largest when the mass flux is low. This is expected at a lower mass flux because the influence of the electric body forces will be greater in relation to the inertia of the fluid. At a higher mass flux (110kg/m^{2}s) the inertia of the fluid breaks up the EHD flow structures, causing an additional wetting of the channel. This results in an increase in the thermal resistance at the heat transfer surface.

The EHD flow structures cannot be sustained at a mass flux of 110kg/m^{2}s and the heat transfer enhancement mechanisms associated with the structures are not realized. This is reflected in the marginal increase in the heat transfer coefficient, as shown in Figure 7.4(ii). In comparing the results for a mass flux of 45kg/m^{2}s and 55kg/m^{2}s, the heat transfer enhancement is higher at 55kg/m^{2}s. The increase in velocity from 45kg/m^{2}s to 55kg/m^{2}s would increase the convective heat transfer in the system and this velocity increase is not large enough to cause a breakup of the EHD flow structures.

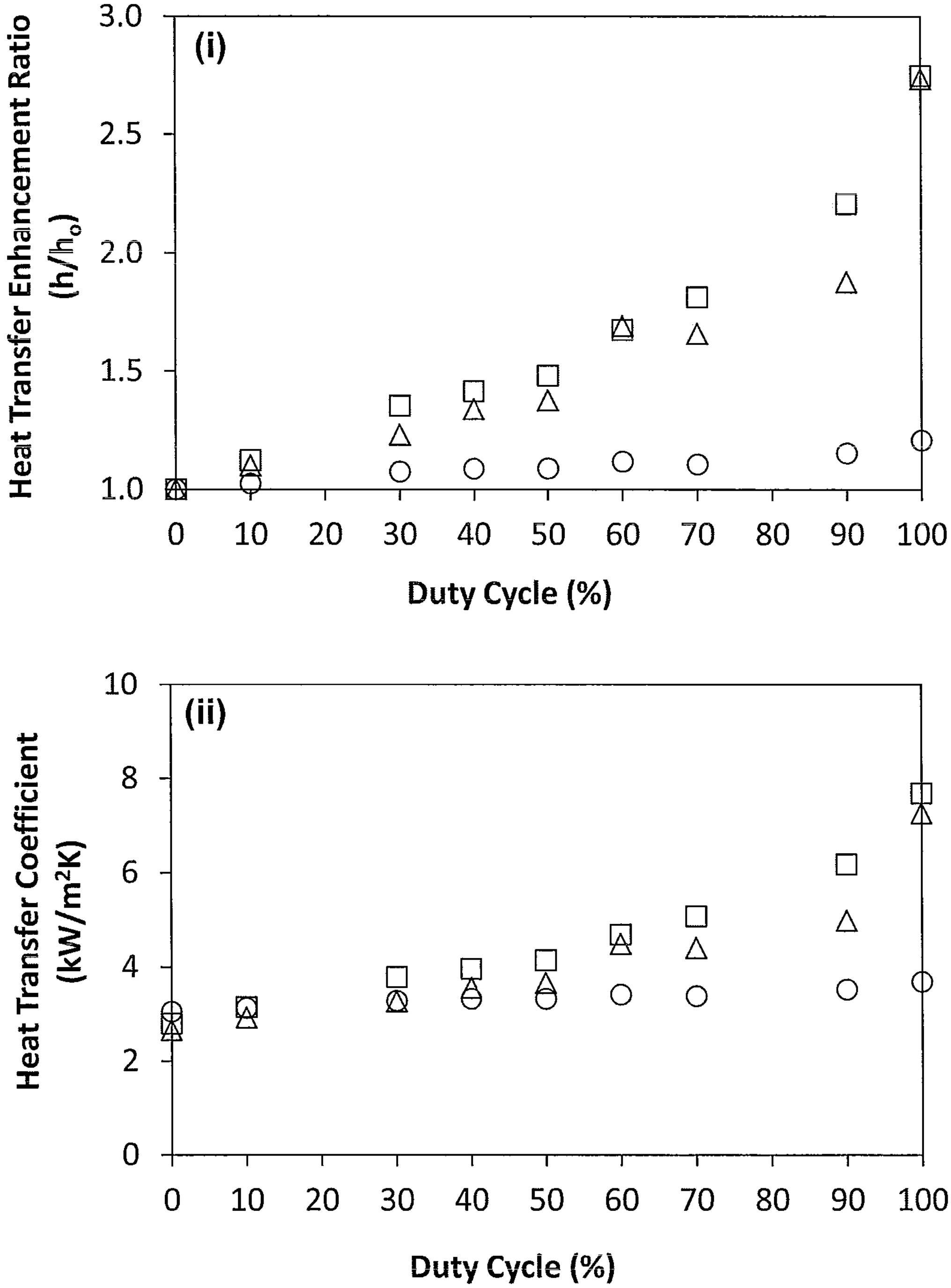

Figure 7.4 – Effect of duty cycle on the (i) heat transfer enhancement ratio and (ii) heat transfer coefficient for a pulse width of 58ms, average quality of 50% and mass flux of Δ45, □55 and ○110 kg/m^{2}s.

In each of the different cases, the enhancement increases with the duty cycle even though the EHD transient flow structures are more pronounced at the lower duty cycles (< 40%). For example, at a duty cycle of 10% (Figure 6.3(i)(a)-(d)), a large number of twisted liquid cones is seen to develop from the central electrode, resulting in the extraction of the liquid thermal resistance from the heat transfer surface and into the central core. At a duty cycle of 70%, less twisted liquid cones are observed; however, the results show that the heat transfer enhancement at a 70% duty cycle is much greater than the enhancement at a 10% duty cycle. The greater enhancement is due to a higher effective voltage at a 70% duty cycle than at a 10% duty cycle and the EHD effect is active for a longer period at high duty cycles. These results show that the overall enhancement may be greater if a flow pattern with a lower heat transfer performance is maintained longer than a flow pattern that may exhibit higher heat transfer enhancement over a shorter time period. An attempt to predict the heat transfer at a duty cycle of 100% using the correlation presented in Section 3.5.4 was performed. The electric field strength used in the correlation was taken from the numerical analysis for a stratified flow (see Appendix D) and the results showed that the correlation is inadequate in the current studies as it greatly overestimates (2x) the expected heat transfer enhancement.

The effect of EHD on the pressure drop for the three different mass fluxes is shown in Figure 7.5. The results show that the pressure drop ratio is greatest at the lower mass fluxes and increases with duty cycle. The influence of EHD on the pressure drop is less pronounced at a higher mass flux because the EHD effect decreases with an increase in the fluid velocity (see Section 3.3) while the influence of the fluid velocity on the

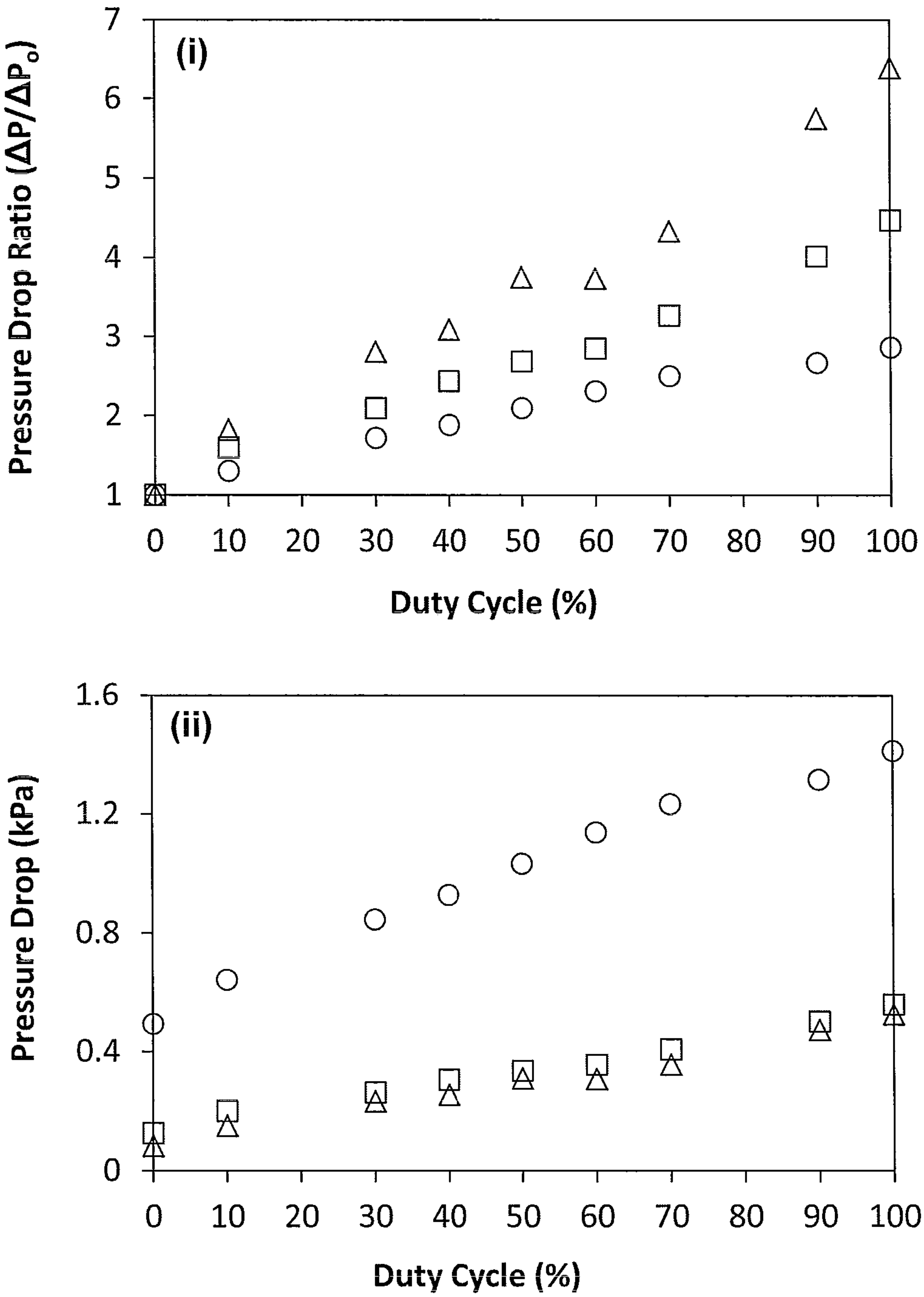

Figure 7.5 – Effect of duty cycle on the (i) pressure drop ratio and (ii) pressure drop for a pulse width of 58ms, average quality of 50% and mass flux of Δ45, □55 and ○110 kg/m^{2}s.

pressure drop increases ($\Delta P \alpha u^2$). An increase in the pressure drop is also observed with an increase in the duty cycle because the EHD flow pattern is sustained for a longer period of time. A review of the EHD heat transfer and pressure drop results for different mass fluxes shows the benefits of using the EHD technique for heat transfer enhancement. For example, at a duty cycle of 70% in Figure 7.4(ii) and Figure 7.5(ii), the results show that the heat transfer enhancement is 30% higher at a mass flux of 45kg/m^{2}s than at a mass flux of 110kg/m^{2}s while the pressure drop at a mass flux of 45kg/m^{2}s is lower than the pressure drop at both a 70% duty cycle and for the case of no EHD at a mass flux of 110kg/m^{2}s. In typical heat exchangers, the heat transfer is controlled by controlling the flow rate of the heat transfer fluid in the system, where an increase in the flow rate increases heat transfer while also imposing a pressure drop penalty. The EHD technique provides an alternative means to increase heat transfer while imposing a significantly lower pressure drop penalty than in the case for an increasing mass flux.

The heat transfer enhancement of the various EHD flow structures observed at different duty cycles is difficult to measure because they are only present in the transient when the EHD is applied in pulses, with different structures due to different applied effective voltages. A comparison of the heat transfer enhancement of the different EHD flow structures at the various duty cycles can be estimated by dividing the enhancement ratio by the effective voltage and the results are shown in Figure 7.6. The heat transfer enhancement per applied effective voltage decreases for an increasing duty cycle. The EHD flow structures were more prominent at low duty cycles and Figure 7.6 shows that they result in the largest enhancement of heat transfer. This large enhancement was not

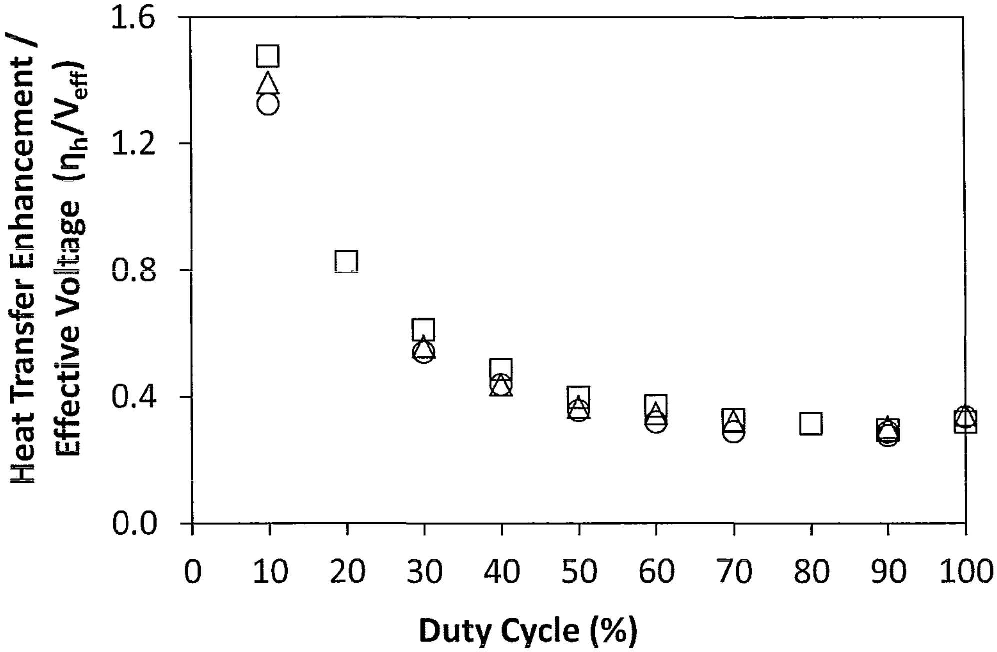

Figure 7.6 – Heat transfer enhancement per applied effective voltage for different duty cycles for the case of a mass flux of 55kg/m^{2}s, average quality of 50% and pulse width of ○29, Δ58 and □115ms.

obvious in Figure 7.1 and Figure 7.4 because the heat transfer enhancement was an average between the heat transfer of the EHD flow pattern during the pulse ON period and the flow pattern in the absence of EHD during the pulse OFF period.

7.3 Heat Transfer and Pressure Drop Performance of Twisted Liquid Columns

Similar to the analysis of the twisted liquid cones, the heat transfer performance of the twisted liquid columns is measured indirectly because of its transient nature.

7.3.1 Effect of Duty Cycle on Heat Transfer and Pressure Drop for a Negative PWM Waveform

The heat transfer and pressure drop characteristics for negative pulse width modulated waveforms are similar to that of a positive pulse. A comparison between the heat transfer and pressure drop results for a mass flux of 55kg/m^{2}s, average quality of 50%, pulse width of 58ms and a range of duty cycles is shown in Figure 7.7 and Figure 7.8 respectively. One notable difference in the results is that the enhancement of heat transfer is slightly higher for a positive applied voltage than a negative applied voltage at the higher duty cycles. This is a result of the greater wetting of the heat transfer surface using a negative applied voltage, which is due to the additional repulsion of the liquid due to charge injection at the center electrode. As discussed in Chapter 6, a negative polarity

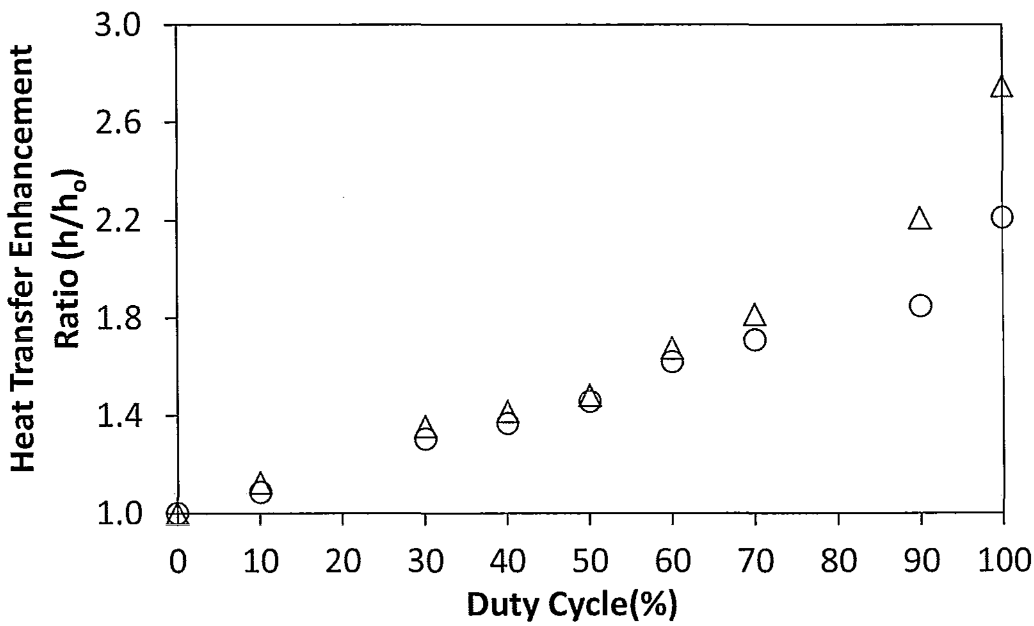

Figure 7.7 – Heat transfer enhancement for a mass flux of 55kg/m^{2}s, average quality of 50% and different for an applied voltage of o-8kV and Δ+8kV.

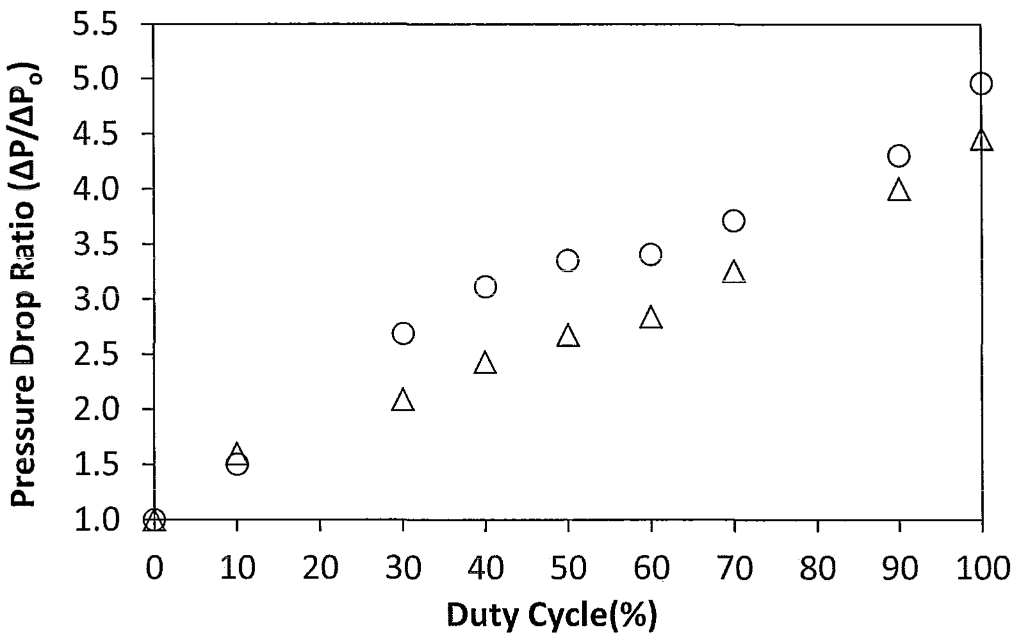

Figure 7.8 – Pressure drop ratio for a mass flux of 55kg/m^{2}s, average quality of 50% and different for an applied voltage of o-8kV and Δ+8kV.

pulse results in the rejection of liquid from the rod electrode due to the dielectrophoretic and electrophoretic force. For a positive polarity pulse, the rejection of liquid is due to the dielectrophoretic force while the negative charges are attracted the liquid towards the electrode due to the electrophoretic force. More liquid repulsed towards the outer tube will result in a greater thermal resistance at the heat transfer surface. Therefore, it is expected that negative polarity flow patterns will exhibit lower heat transfer than a positive polarity flow pattern. This additional wetting is also reflected in the higher increase in pressure drop for a negative applied voltage because of the greater frictional shear between the liquid and the tube surface.

A comparison of the wall temperatures and refrigerant bulk saturation temperature as a function of duty cycle for a negative applied pulse waveform is shown in Figure 7.9.

The trends in the subcooled temperatures for negative waveforms is similar to the positive waveforms (Figure 7.3) indicating that the twisted liquid columns enhance heat transfer and affect the pressure drop in a similar manner.

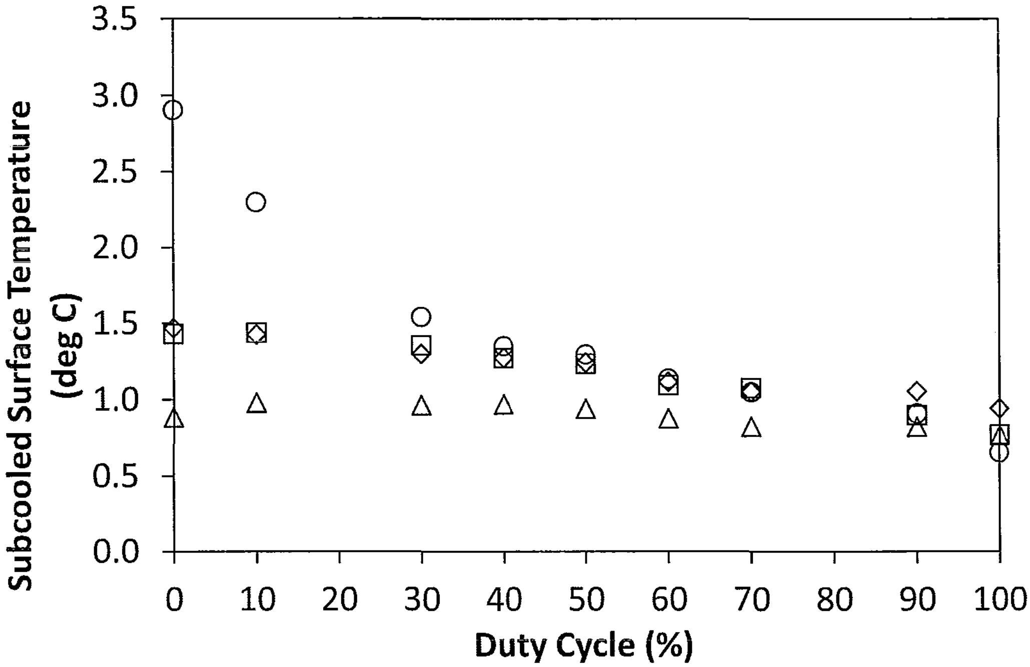

Figure 7.9 – Comparison between the tube wall and refrigerant bulk saturation temperatures for a mass flux of 55kg/m^{2}s, average quality of 50%, -8kV pulse, 58ms pulse width and a range of duty cycles.
Location of wall temperature measurements: Δ top and □, ◊ sides and ○bottom.

7.4 Heat Transfer and Pressure Drop Performance of a Twisted Liquid Cone and Column Flow Pattern

7.4.1 Effect of Positive and Negative Pulses on Heat Transfer and Pressure Drop

The effect of using a pulse waveform with positive and negative pulses on the heat transfer and pressure drop is presented in Figure 7.10 and Figure 7.11. The legend in Figure 7.10 and Figure 7.11 describes the percent time the positive pulse is applied, followed by the time the negative pulse is applied and then the time when no high voltage is applied for a total waveform period of 115ms. For example, in Figure 7.10, the case of +50%, -1%, 49% off represents a +8kV pulse applied for 58ms, followed by a -8kV pulse for 1.15ms and then no application of high voltage for 55.85ms. Figure 7.10 indicates that the heat transfer enhancement ratio decreases as the percent ON time of the negative voltage increases, as indicated by either comparing the results in the cases where the effective voltage is less than 8kV and in comparing the various cases for an effective voltage of 8kV in Figure 7.10. In the cases for an effective voltage of 8kV, increasing the positive high voltage pulse width will increase the heat transfer for a condensation process.

The decrease in the heat transfer by applying a negative voltage following a positive pulse can be determined by measuring the subcooled wall temperatures. Figure 7.12 shows the subcooled wall temperature for the cases with an 8kV pulse applied for 50% of the total waveform period, followed by a -8kV pulse for a varying duration for the remaining 50% of the period. The results show that the subcooled wall temperatures

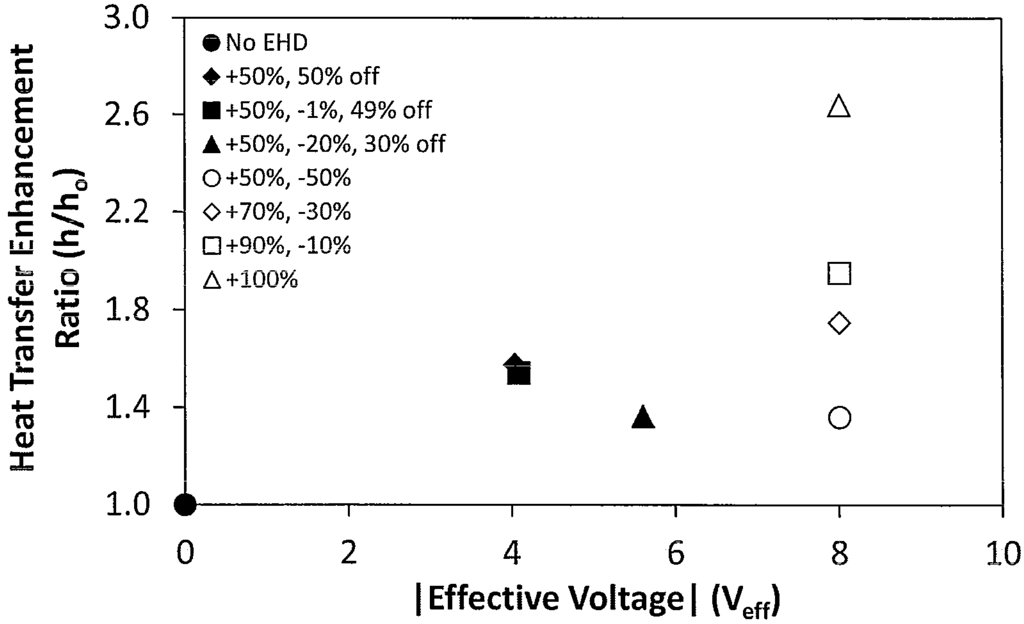

Figure 7.10 – Effect of different pulse conditions on the heat transfer enhancement for a mass flux of 55kg/m^{2}s, average quality of 50% and different effective voltages

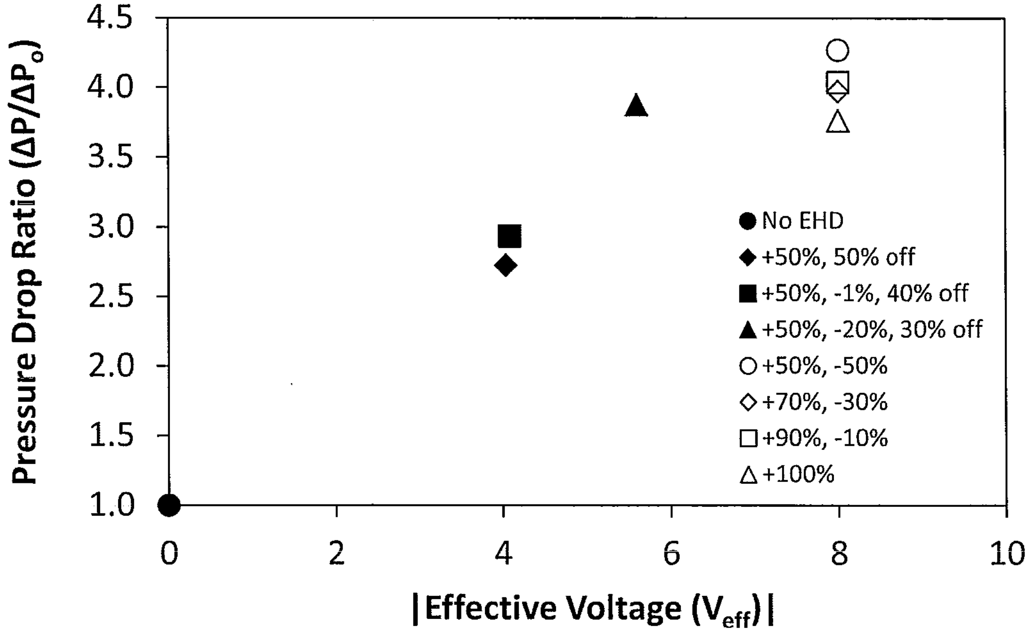

Figure 7.11 – Effect of different pulse conditions on the pressure drop ratio for a mass flux of 55kg/m^{2}s, average quality of 50% and different effective voltages.

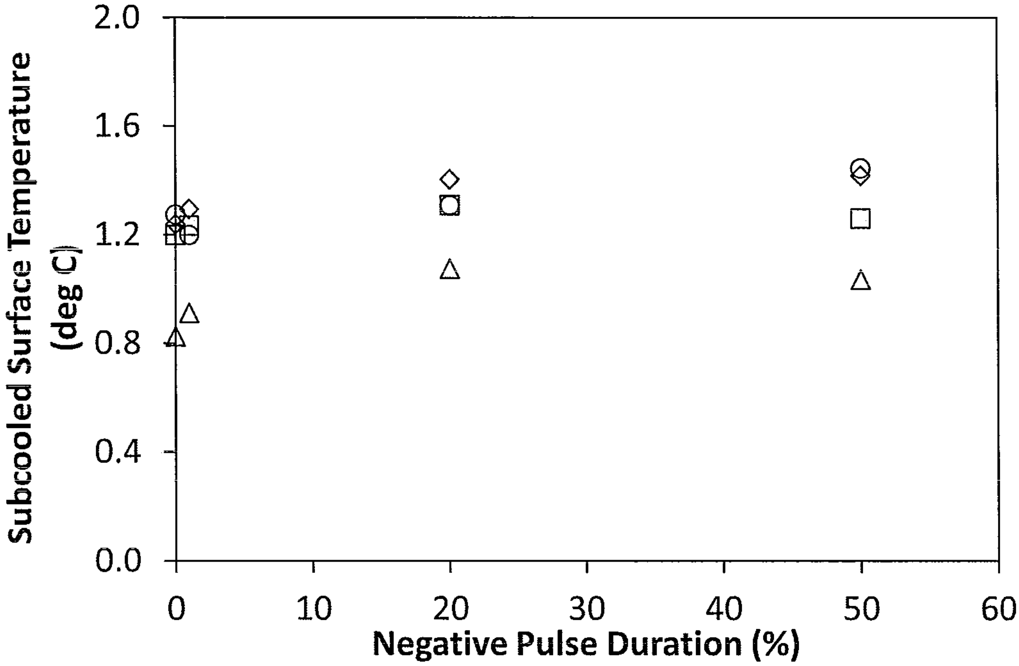

Figure 7.12 – Comparison between the tube wall and refrigerant bulk saturation temperatures for a mass flux of 55kg/m^{2}s, average quality of 50%, fixed +8kV pulse, 58ms pulse width and a -8kV pulse with varying pulse durations. Location of wall temperature measurements: Δ top and □, ◊ sides and ○bottom.

of the tube increases with an increase in the duration of the applied negative pulse. The change in the subcooled temperatures is attributed to the rejection of the liquid cones towards the heat transfer surface and the development of the liquid columns during the change from a positive to negative polarity. The number of twisted liquid cone flow structures was observed to be higher during the positive pulse duration when the negative pulse duration component of the waveform is increased, as determined in Section 6.2.3. The greater density of liquid cones around the electrode during the transition from the positive to negative pulse results in a greater wetting in all regions of the tube during the ensuing repulsion of liquid and thus the thermal resistance increases. Although the twisted liquid cones and twisted liquid columns are sustained during the entire positive and negative pulse duration, the increase in the thermal resistance during the transition between pulse polarities results in an overall lower heat transfer enhancement.

An increase in the negative pulse width following a 50% positive pulse was determined to increase the pressure drop. The increase in pressure drop is a result of sustaining the twisted liquid cones and columns during the positive and negative pulse and because the number of twisted cones increases when the negative pulse width increases, a corresponding increase in pressure drop is also observed. This is also shown in Figure 7.11, where the pressure drop is highest for a larger negative pulse width in the case with an effective voltage of 8kV.

7.5 Heat Transfer and Pressure Drop Performance of an EHD Entrained Droplet Flow Pattern

7.5.1 Effect of Entrained Droplets on Heat Transfer and Pressure Drop

The effect of creating entrained droplets using EHD on the heat transfer performance is shown in Figure 7.13. In this figure, the heat transfer results for an entrained droplet flow pattern (pulse repetition frequency of 60Hz) are compared to the results using a 58ms pulse width (results from Figure 7.4). The results show that the heat transfer enhancement is similar between the two cases, where heat transfer increases with duty cycle. The pressure drop ratio between the entrained droplet flow pattern and a flow pattern with a 58ms pulse width waveform is also compared and shown in Figure 7.14.

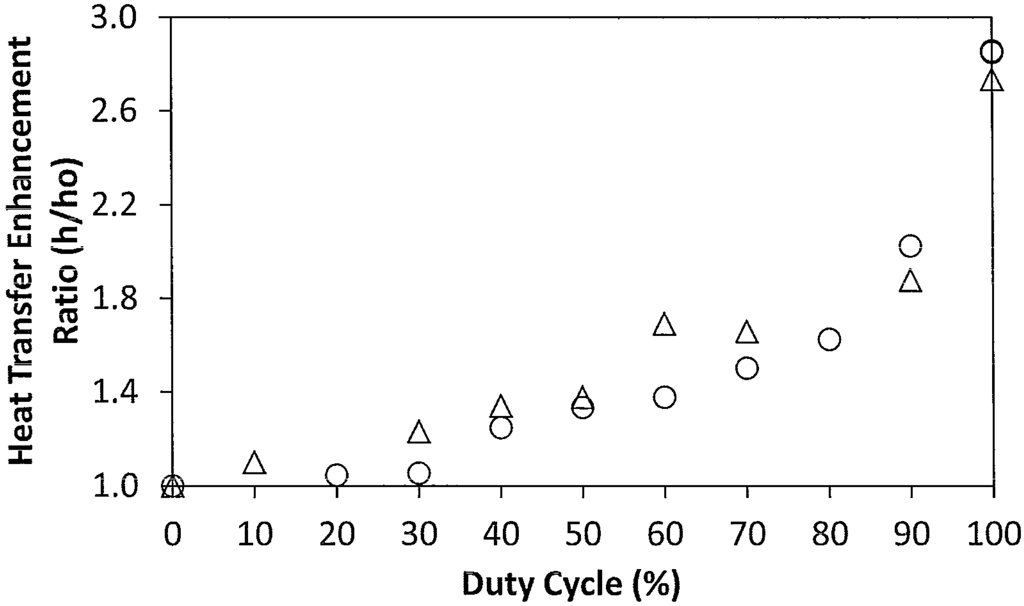

Figure 7.13 – Effect of duty cycle on the heat transfer enhancement ratio for a mass flux of 45kg/m^{2}s and average quality of 50% for a ○ entrained droplet flow pattern and a Δ 58ms pulse width flow pattern.

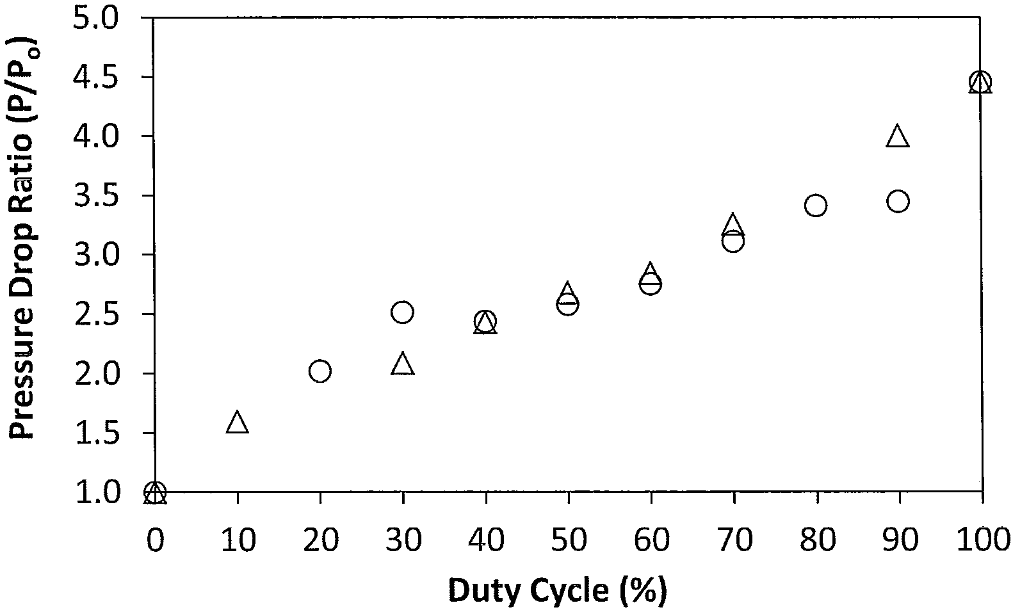

Figure 7.14 – Effect of duty cycle on the pressure drop ratio for a mass flux of 45kg/m^{2}s and average quality of 50% for a ○ entrained droplet flow pattern and a Δ 58ms pulse width flow pattern.

The similar trends in both heat transfer and pressure drop indicate that the entrained droplet flow pattern has the same effect on heat transfer and pressure drop as the 58ms pulse width waveforms. There appears to be no clear advantage in sustaining one flow pattern over the other as the heat transfer enhancement using a 58ms pulse width is only marginally higher and the pressure drop increase is nearly identical in both cases.

A review of the subcooled surface temperatures (Figure 7.15) shows a decrease at all thermocouple locations with an increase in duty cycles. In the case of a fixed positive or negative 58ms pulse width for various duty cycles (Figure 7.3 and Figure 7.9), the surface temperature at the bottom and sides collapse to the same temperature at duty cycles above 40%. This differs in the entrained droplet case, where there is a notable

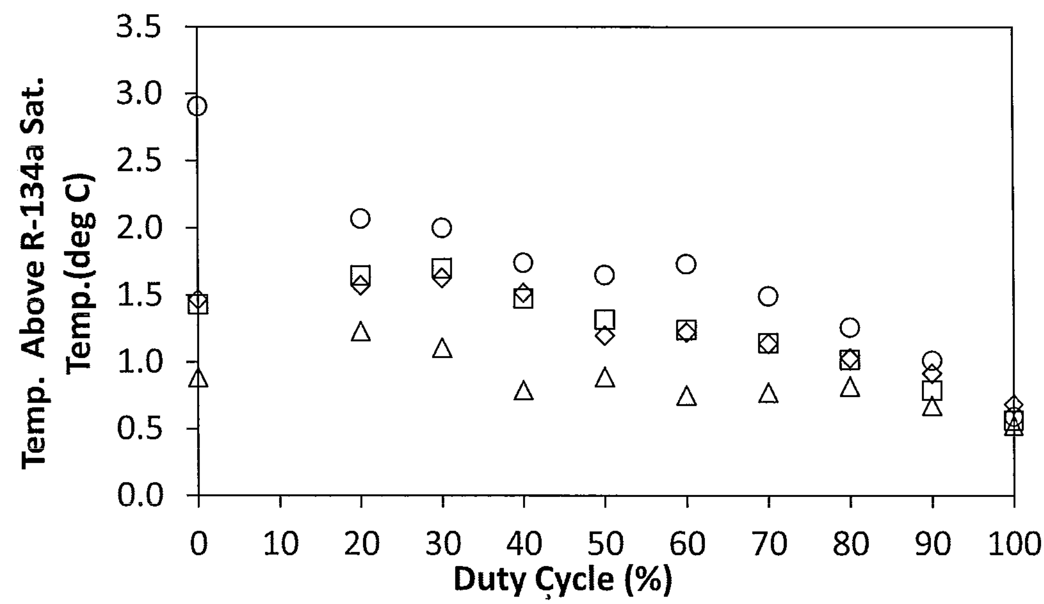

Figure 7.15 – Comparison between the tube wall and refrigerant bulk saturation temperatures for a mass flux of 45kg/m^{2}s, average quality of 50%, +8kV pulse and pulse repetition frequency of 60Hz.
Location of wall temperature measurements: Δ top and □, ◊ sides and ○bottom.

temperature difference (approx. 0.5°C) between the top and side measurement locations until the very high duty cycles (> 90%) where the temperatures collapse. This indicates that the flow pattern differs between the two cases differs as the flow pattern and explains the slightly higher enhancement of heat transfer in the 58ms pulse width case.

7.6 Summary of Two-Phase EHD Condensation Heat Transfer and Pressure Drop

7.6.1 Enhancement and Control of Condensation Heat Transfer and Pressure Drop

The heat transfer and pressure drop results for the various two-phase flow patterns presented in this chapter shows that a wide range of control of the condensation heat transfer and pressure drop may be achieved using the EHD technique. For example, a comparison of the heat transfer enhancement in Figure 7.10 and the pressure drop ratios in Figure 7.11 show that at an effective voltage of 8kV, the heat transfer can be enhanced in a range between 1.35-fold to 2.65-fold, while maintaining a relatively constant 4-fold increase pressure drop ratio. These results show that heat transfer can be independently controlled at a fixed pressure drop by using a positive and negative PWM waveform with a varying bias between the positive and negative pulse width. A summary of all the heat transfer and pressure drop results determined for a mass flux between 45 to 55kg/m^{2}s and quality of 50% is shown in Figure 7.16. Figure 7.16 shows that at any particular heat transfer enhancement ratio there are a multiple of corresponding pressure drop ratios. The different combinations of heat transfer and pressure drop are dependent on the PWM waveform applied. Different flow patterns were observed for different PWM waveforms and as heat transfer and pressure drop are highly dependent on the flow pattern, this results in the different heat transfer and pressure drop combinations seen in Figure 7.16. These results show the potential in using EHD as a mechanism to control heat transfer and pressure drop and that to optimize the heat transfer and pressure drop, an understanding of the effect of EHD on the flow distribution is required.

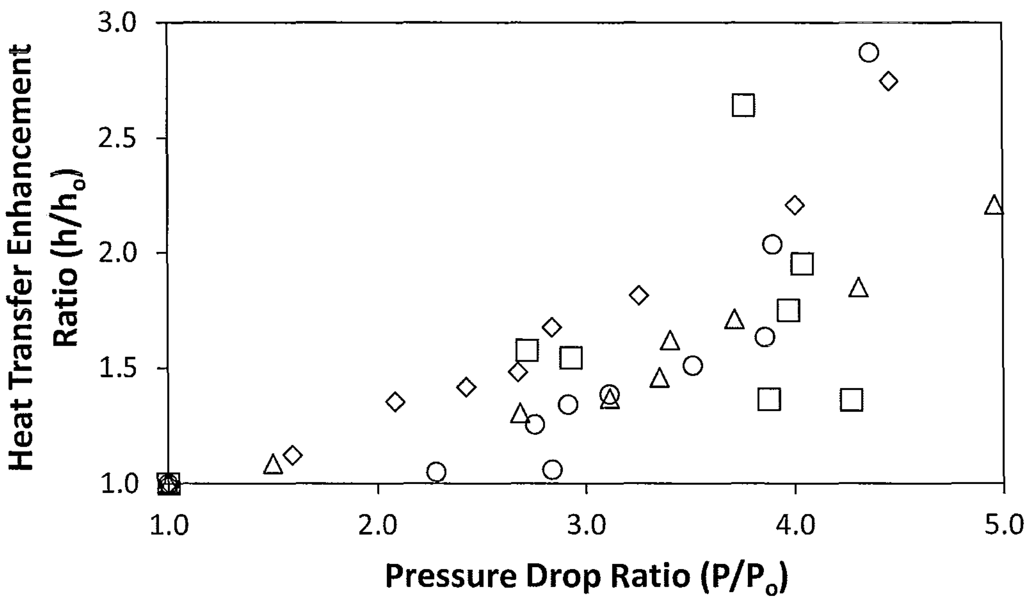

Figure 7.16 – Heat transfer enhancement and pressure drop ratios combinations for ◊ +8kV, 58ms pulse width , ∆ -8kV, 58ms pulse width, □ twisted liquid cone/column and ○ entrained droplet flow patterns.

Chapter 8 – Conclusions and Recommendations

8.1 Research Summary and Conclusions

The objectives of the research were to investigate the EHD phenomenon on a dielectric fluid flow, determine the sustainability of EHD specific transient flow patterns, such as a twisted liquid cone, twisted liquid column or entrained droplet flow patterns, in two-phase applications and determine the corresponding impact of the EHD flow patterns on the heat transfer and pressure drop performance. The motivation for this research is that a complete understanding of the effect of EHD on heat transfer and pressure drop is required if the technique is to be used as a method of augmenting and controlling heat transfer in a heat exchange system. The potential benefits in implementing EHD in heat exchange systems include an improvement in the system efficiency, reduction in the physical size of the system and the ability to adapt to meet various system demands.

The test facility used in this investigation is a single-pass, counter-current, shell and tube heat exchanger with a stainless steel rod fitted concentrically inside the tube to apply the EHD. The working fluids used in the experiments are refrigerant R-134a in the tube side and chilled water on the shell side. This test facility consisted of two test sections, a section to measure the heat transfer and pressure drop performance and a section to visualize the flow pattern using a high speed camera. The research objectives were accomplished by performing a series of single-phase and two-phase flow experiments. The single-phase liquid experiments were performed to understand the charge injection and electroconvection phenomenon that occur due to the application of high voltage in this shell and tube heat exchange configuration. Two-phase flow experiments were then performed to determine the various transient EHD flow patterns, develop a means to sustain the flow patterns, and evaluate the heat transfer and pressure drop characteristics of each of the different flow patterns.

In the single-phase studies, the effect of the voltage amplitude and polarity on the charge injection and heat transfer enhancement was experimentally determined. Current measurements indicate that an applied negative polarity voltage at the center electrode resulted in a greater charge injection (i.e. higher current) than a positive applied voltage at the electrode. The heat transfer results for different voltage amplitudes, voltage polarities and duty cycle shows that the enhancement is higher with a negative applied polarity and increases with effective voltage to a maximum of approximately 2-fold. A spike in the heat transfer enhancement is observed in the DC case for applied voltages $\geq$ 4kV and this was predicted using a dimensionless analysis comparing the EHD forces to the inertia forces ($Ehd/Re^2 > 1$). Based on the current measurement, heat transfer measurements and a review of the experimental findings in literature, it was determined that the mechanisms of charge injection in this annular test section is negative charges will always be injected from the negative electrode. The understanding of the charge injection method in this particular geometry was found to be essential in understanding the physical mechanisms of the various flow structures that may be produced when EHD is applied to a two-phase flow and in sustaining the various flow patterns.

The two-phase flow investigations can be separated into two parts, 1) characterization of the various EHD flow patterns and 2) measurement of the heat transfer and pressure drop characteristics of the various EHD flow patterns. In the first part of the two-phase investigations, experiments were performed to observe and to sustain five different flow patterns using ±8kV PWM waveforms. These flow patterns are classified as a twisted liquid cone, twisted liquid column, twisted liquid cone and column, entrained droplet flow pattern and inverse annular flow. The results of the investigations performed in developing and sustaining these flow patterns using various PWM waveforms are summarized according to the polarity of the applied voltage.

1(i) Positive Pulse Waveforms:

A flow pattern consisting of twisted liquid cones was observed using positive PWM waveforms. Flow visualization shows that twisted liquid cone flow structures are present in the low duty cycle range (< 40%) and at higher duty cycles (> 40%) entrained droplets are produced. For very high duty cycles (> 90%) an inverse annular flow pattern was observed where liquid is extracted from the lower liquid stratum and completely surrounds the electrode. The time required for the twisted liquid cones to fully develop is estimated to be approximately 58ms and the pulse OFF time required such that the twisted liquid cones are developed during the pulse ON period is determined to be approximately 520ms. This pulse OFF period is much larger than the time that the twisted liquid cones are present during the pulse ON period. At a mass flux of 45 or 55kg/m^{2}s, the twisted liquid cones decayed over time and were non-existent after approximately 365ms. At a mass flux of 110kg/m^{2}s, the twisted liquid cones could not be sustained due to the higher velocities.

A flow pattern consisting of entrained droplets in the vapour core was observed when small pulse widths (3-15ms) of positive high voltage were applied. The size of the droplets was determined to increase with duty cycle due to electrocoalescence and the majority of the droplets are entrained in the lower vapour core. An entrained droplet flow pattern was present for both low and high duty cycles.

1(ii) Negative Pulse Waveforms:

A flow pattern consisting of twisted liquid column flow structures was observed using negative PWM waveforms. These flow structures were observed in place of the twisted liquid cones that were present in the positive pulse waveform case. The twisted liquid columns are predominantly observed at the bottom and sides of the tube. The differences between the flow structures was determined to be due to the mechanisms of charge injection in this particular geometry, where negative charges are always injected from the negative electrode.

1(iii) Positive and Negative Pulse Waveforms:

The twisted liquid cone or column flow structures were sustained during the positive or negative pulse ON periods, respectively, for duty cycles greater than 40%

using pulse waveforms containing positive and negative pulses. The switch in pulse polarity was found to be sufficient in disrupting the charge distribution/accumulation at the interfaces and the result was that the twisted liquid cones or columns were always observed during the positive or negative pulse, respectively. This study revealed that the development of the twisted liquid cones or columns is dependent on the charge distribution/accumulation in the fluid.

In the second part of the two-phase investigations, the effect of applying the various PWM waveforms used in sustaining the EHD flow patterns on the condensation heat transfer and pressure drop characteristics was determined. The results of the investigation are once again summarized according to the polarity of the applied voltage.

2(i) Positive Pulse Waveforms:

The enhancement of heat transfer and pressure drop was determined for three different pulse widths (29, 58, 115ms) and mass flux (45, 55, 110kg/m^{2}s) for a range of duty cycles between 0 to 100%. The heat transfer enhancement and pressure drop ratio increased with duty cycle and pulse width. Higher pulse widths sustain the EHD flow structures (twisted liquid cones at duty cycles $\leq$ 40% and entrained droplets at duty cycles > 40%) for a longer time period and higher duty cycles result in a greater effective voltage applied to the flow. An increase in the effective voltage increases the heat transfer because it is a measure of the overall voltage applied per pulse cycle. An increase in mass flux results in a decrease in heat transfer and an increase in pressure drop. At a high mass flux, the inertial forces in the flow begin to dominate over the EHD forces, as predicted by the dimensionless analysis.

The maximum increase in the heat transfer coefficient using only positive PWM waveforms was determined to be 2.7-fold with corresponding increase in the pressure drop of 4.5-fold. The maximum increase occurred at a duty cycle of 100% where an inverse annular flow pattern was present. Although this case showed the highest heat transfer enhancement, an analysis to determine the heat transfer enhancement per effective voltage showed that the low duty cycle flow patterns had the highest heat transfer enhancement potential (1.4-fold enhancement per effective voltage (kV)). The large enhancement potential is due to the presence of the twisted liquid cone flow structures, which were present in the low duty cycles. However the heat transfer performance of these structures could not be utilized with the positive PWM waveforms because of its transient nature and the requirement for a large pulse OFF period (approx. 520ms) such that the structures are present during the pulse ON period.

2(ii) Negative Pulse Waveforms:

The heat transfer and pressure drop was measured for the case of a mass flux of 55kg/m^{2}s, quality of 50% and a range of duty cycles between 0 and 100%. The results show that the enhancement of heat transfer is lower when a negative pulse is used instead of positive pulse, while the pressure drop increases with a negative pulse. This was determined to be a result of a greater wetting of the heat transfer surface with a negative polarity pulse, which increases the thermal resistance at the heat transfer surface and also the frictional pressure drop.

2(iii) Positive and Negative Pulse Waveforms:

The results show that pulse waveforms containing both positive and negative pulses exhibit lower heat transfer and higher in the pressure drop compared with a single polarity waveform with the same effective voltage. The switch of the pulse from positive polarity to negative polarity results in the repulsion of the fluid around the electrode and leads to a significant wetting of the heat transfer surface. The heat transfer results indicate that the increase in heat transfer by using positive and negative polarity pulses to sustain the twisted liquid cones and columns is offset by the severe decrease in heat transfer due to the additional wetting of the heat transfer surface during the polarity switch.

An evaluation of the heat transfer and pressure drop results obtained by sustaining various EHD flow patterns shows that a wide range of heat transfer and pressure drop conditions can be achieved (see Figure 7.16). The thesis research demonstrates the potential of utilizing EHD as an effective means to control and enhance heat transfer in a heat exchange system and also the importance of understanding the effect of EHD phenomenon on two-phase flow redistribution.

To conclude this thesis, the key contributions of the investigations performed are as follows:

- The mechanism of charge injection in an annular geometry with a high voltage inner rod electrode and grounded outer tube was determined
- The mechanisms involved in the production of various EHD flow structures such as twisted liquid cones, twisted liquid columns and entrained droplets were determined (i.e. charge injection, electric field distribution)
- The effect of pulse waveform parameters such as pulse width, pulse amplitude and duty cycle on the development and sustainability of 5 different EHD flow patterns was investigated
- The heat transfer and pressure drop characteristics of 5 different EHD flow patterns were determined.
- The use of the EHD technique as a means to control and enhance heat transfer was demonstrated

8.2 Recommendations for Future Work

The work presented in this research shows that by understanding the mechanisms involved in manipulating two-phase flow patterns using EHD, significantly different heat transfer and pressure drop combinations may be achieved. Some of the recommendations for in the continuation of this work are as follows:

- Evaluate the effect of EHD for other various vapour qualities. In condensation heat transfer, the quality changes along the heat exchange section. An understanding of the effect of quality on EHD flow patterns will provide a better understanding of the validity of this flow pattern approach for enhancing/controlling heat transfer in a heat exchange system.

- Evaluate the effect of the PWM waveforms for evaporation heat transfer. The results using positive and negative pulses in a waveform results in a decrease in heat transfer enhancement because of significant wetting of the heat transfer surface. This effect would be very beneficial in evaporation heat transfer.
- Evaluate the effect of applying a gradual change between polarities in the PWM waveforms containing both positive and negative polarity pulses to improve the heat transfer and pressure drop performance. A gradual change between the positive and negative pulses may reduce the amount of repulsion of liquid towards the outer tube surface during the transition between pulses polarities, which was found to be detrimental to the condensation heat transfer performance.
- Evaluate the mechanisms involved in the inverse annular flow pattern. This flow pattern is observed after the flow has reached steady state and is believed to be a result of the flow distributing itself to minimize the potential energy in the system. An energy minimization analysis is recommended to be performed to validate the observed inverse annular flow pattern.
- Evaluate the potential in using EHD to control/enhance heat transfer and pressure drop in other heat exchange geometries, such as plate style heat exchangers which are widely used in industry.

Appendix A – Thermophysical and Electrical Properties of Refrigerant R-134a

A.1 Thermophysical Properties of R-134a

The thermophysical properties for R-134a were determined using correlations taken from Dupont (2005). The various correlations are given in Table A1.

Table A1 – Thermophysical properties of refrigerant R-134a. [Dupont (2005)]

Property	State	Correlation	R^2
Pressure (kPa)	Saturated	$P_s = -184.53 + 474.73exp\left(\frac{T_s}{42.96}\right)$	0.9999968
Density (kg/m^3)	Subcooled Liquid	$\rho_l = 1290.68 - 2.317T^{1.1173}$	0.999979
Specific Heat (kJ/kgK)	Subcooled Liquid	$c_{p_l} = 1.1527 + 0.1824exp\left(\frac{-T}{62.569}\right)$	0.9999528
Viscosity (μPas)	Subcooled Liquid	$\mu_l = 18.382 + 268.55exp\left(\frac{-T}{77.425}\right)$	0.9999945
Thermal Conductivity (mW/mK)	Subcooled Liquid	$k_l = 93.443 - 0.4648T^{0.99816}$	0.9999426
Density (kg/m^3)	Saturated Liquid	$\rho_{l,s} = (38.378 - 0.1414P^{0.5})^2$	0.9999959
	Saturated Vapour	$\rho_{v,s} = -371.336 + 372.316exp\left(\frac{P}{8230.56}\right)$	0.9999995
Specific Heat (kJ/kgK)	Saturated Liquid	$c_{p_{l,s}} = 1.5364 + \left[0.00482\frac{P}{ln(P)}\right]$	0.9999293
	Saturated Vapour	$ln(c_{p_{v,s}}) = -0.304973 + 0.0018896P^{0.5}ln(P)$	0.9999316
Viscosity (μPas)	Saturated Liquid	$\mu_{l,s} = [32.299 - 2.87848ln(P)]^2$	0.9999916
	Saturated Vapour	$\mu_{v,s} = (2.9554 - 0.02081P^{0.5})^2$	0.9999128
Thermal Conductivity (mW/mK)	Saturated Liquid	$k_{l,s} = 1/[0.008661 + 2.11 \times 10^{-5}P^{0.5}ln(P)]$	0.9999232
	Saturated Vapour	$k_{v,s} = 1/[0.17917 - 0.01662ln(P)]$	0.9999789

A.2 Electrical Properties of R-134a

The dielectric constant and volume resistivity of refrigerant R-134a for the experimental conditions is 9.51 and 17700MΩ-m respectively [ASHRAE (2001)]. The voltage required for electrical breakdown (or arcing) of R-134a was experimentally determined [Cotton (2000)] to occur at applied DC voltages of 10kV. However, under a phase change process, arcing was occasionally observed by Cotton (2000) to occur at 9kV.

Appendix B– Uncertainty Analysis

The uncertainty of the various experimental measurements and calculated parameters are provided in this section. The uncertainty analyses are performed in accordance to the guidelines outlined by Kline and McClintock (1953). The overall uncertainty of a particular measure can be determined as

$$\delta T = \sqrt{\sum_{i=1}^{n} (\delta_i)^2} \tag{B1}$$

where δ_i is the various identified uncertainties in a particular measurement. The various uncertainties that are used in the determination of the overall uncertainty may be due to the inherent uncertainty of the measurement device and in the set-up of the measurement system.

B.1 Uncertainty of Temperature Measurements

As outlined in Chapter 2, two different temperature measurement devices (RTD and thermocouple). The uncertainty of a RTD and thermocouple measurement systems can then be determined in the following sections.

B.1.1 Uncertainty of temperature measurement using a RTD

The various uncertainties of the RTD system include

i) The manufacturer's stated uncertainty of the platinum RTD probe (±0.01°C).

ii) The resolution of the Omega DP-251 RTD reader (±0.01°C).

iii) The drift in the accuracy of the RTD probe since the last calibration (5 years prior) of the device (±0.0075°C per year over 5 years -> ±0.0375°C) [Drnovsek et al. (1998)].

Using Eq. (B1), the uncertainty of the RTD temperature readings is determined to be

$$\delta T_{RTD} = \sqrt{(0.01)^2 + (0.01)^2 + (0.0375)^2} = \pm 0.04^{\circ}\mathrm{C} \tag{B2}$$

B.1.2 Uncertainty of temperature measurement using a thermocouple

The various uncertainties of the thermocouple system include

i) Uncertainty of RTD used in the calibration of thermocouple. This includes the uncertainty of the RTD, RTD reader resolution and drift of RTD (±0.01°C, ±0.01°C and ±0.0375°C).

ii) Uncertainty of the thermocouple after calibrated with an RTD (±0.01°C).

iii) Uncertainty in the cold junction. This includes uncertainty in the ice bath temperature and the probe used in measuring this temperature ($\sqrt{(0.01)^2 + (0.01)^2} = \pm 0.0141^{\circ}\mathrm{C}$).

iv) Uncertainty of the data acquisition system (DAQ) (±0.195°C)

v) Uncertainty of the repeatability of the measurements. Using the standard deviation that corresponds to a 95% confidence level for 1000 readings, the uncertainty is approximately ±0.1°C.

The uncertainty of the thermocouple temperature readings is determined to be

$$\delta T_{TC} = [(0.01)^2 + (0.01)^2 + (0.0375)^2 + (0.01)^2 + (0.0141)^2 + (0.2)^2 + (0.1)^2]^{0.5} = \pm 0.22^{\circ}\mathrm{C} \tag{B3}$$

B.2 Uncertainty of Pressure Drop Measurements

The pressure drop was measured using a differential pressure transducer (Validyne DP-15) connected to a two channel Validyne signal conditioner. Two transducers are used, one calibrated for low pressure drops (0 to 1.4kPa) and another for high pressure drops (0 to 3.5kPa). The various uncertainties of the pressure drop measurements include

i) Uncertainty of the transducer (±0.25% of full scale range).

ii) The resolution of the reader used for pressure calibration (±10Pa)

The uncertainty of the pressure drop readings for the two different pressure ranges is determined to be

$$\delta \Delta P_{low} = \sqrt{(0.0025 \times 1400)^2 + (10)^2} = \pm 11\mathrm{Pa} \tag{B4}$$

$$\delta \Delta P_{high} = \sqrt{(0.0025 \times 3500)^2 + (10)^2} = \pm 13\mathrm{Pa} \tag{B5}$$

where the designation *low* refers to the pressure range of 0 to 1.4kPa and the designation *high* refers to a range of 1.4 to 3.5kPa.

B.3 Uncertainty of Mass Flow Rates

The mass flow rate of refrigerant in the tube side and water in the shell side is measured using two turbine flow meters. An Omega flow meter (FTB-502) was used to measure the refrigerant flow and a McMillan microturbine (104 Flo-Sensor) flow meter was used to measure the water flow.

B.3.1 Uncertainty of refrigerant mass flow rate

The maximum uncertainty of the refrigerant mass flow rate measurement include

i) Manufacturer specified uncertainty of the flow meter (±0.55 kg/s).

ii) Manufacturer specified repeatability of measurement (±0.275 kg/s)

Therefore, the maximum uncertainty is

$$\delta \dot{m}_R = \sqrt{(0.55)^2 + (0.275)^2} = \pm 0.61 \text{ kg/s} \tag{B6}$$

B.3.2 Uncertainty of water mass flow rate

The various uncertainties of the water mass flow rate measurement include

i) Manufacturer specified uncertainty of the flow meter (±0.00004 kg/s).

ii) Manufacturer specified repeatability of measurement (±0.000008 kg/s)

Therefore, the maximum uncertainty is

$$\delta \dot{m}_R = \sqrt{(0.00004)^2 + (0.000008)^2} = \pm 4.0\text{x}10^{-5} \text{ kg/s} \tag{B7}$$

B.4 Uncertainty of the Calculated Refrigerant Heat Flux

According to Eq. (4.4), the heat flux is dependent on the water mass flux and temperature difference. The uncertainty of the mass flux and temperature difference was determined previously and therefore the uncertainty of the heat flux can be calculated as

$$\delta q'' = q''\sqrt{\left(\frac{\delta \dot{m}_w}{\dot{m}_w}\right)^2 + \left(\frac{\delta \Delta T_{RTD}}{\Delta T_{RTD}}\right)^2} \tag{B8}$$

The maximum uncertainty of the heat flux in the experiments is determined to be 4%.

B.5 Uncertainty of the Calculated Heat Transfer Coefficient

The heat transfer coefficient is calculated according to (4.6) and is dependent on the surface ($T_{s,avg}$) and refrigerant bulk (T_{sat}) temperatures thermocouple measured using thermocouples and the heat flux. The uncertainties for both a thermocouple measurement and heat flux are presented previously and therefore the uncertainty of the heat transfer coefficient can be calculated as

$$\delta h = h\sqrt{\left(\frac{\delta q''}{q''}\right)^2 + \left(\frac{\delta\left(T_{sat} - T_{s,avg}\right)}{T_{sat} - T_{s,avg}}\right)^2} \tag{B9}$$

The maximum uncertainty of the heat flux in the experiments is determined to be ±24%.

B.6 Uncertainty of the Calculated Inlet Vapour Quality

The inlet vapour quality is determined by measuring the temperature of the subcooled single-phase flow and determining the energy added to the flow by the electrical preheater to achieve the desired inlet quality. The various uncertainties of the calculated vapour quality include

i) Uncertainty of the temperature measurement (±0.22°C).

ii) Uncertainty of the mass flow rate (±4.0x10^{-5}kg/s)

iii) Uncertainty of the electrical preheater. The power supplied to the fluid is equal to the electrical power, which is determined by measuring the voltage and current. The uncertainty of the voltage and current is ±0.1V and ±0.1A respectively, which is the resolution of the multimeter used. The uncertainty of the electrical preheater is then determined ($\sqrt{(0.1)^2 + (0.1)^2}$ = ±0.141W).

iv) Uncertainty in the heat added by the surroundings (approx. ambient temperature range of 22-23°C), which is determined from an energy balance (maximum uncertainty of ±3% of electrical heat added).

The uncertainty of the vapour quality can be calculated as

$$\delta x = x\sqrt{\left(\frac{\delta T_{sub}}{T_{sub}}\right)^2 + \left(\frac{\delta \dot{m}_R}{\dot{m}_R}\right)^2 + \left(\frac{\delta q_{elec}''}{q_{elec}''}\right)^2 + (0.003)^2} \quad \text{(B10)}$$

The maximum uncertainty of the inlet vapour quality is ±4%

Appendix C– System Energy Balance

An energy balance of the EHD test facility (Figure 4.1) was performed to ensure the accuracy of the experimental measurements. The energy balance for the major heat exchange sections (preheater, heat exchange test section and condenser) is presented and discussed.

C.1 Energy Balance of Preheater

An energy balance of the preheater was performed by equating the heat added by the electrical heater to the temperature increase of a single-phase refrigerant flow. The heat added by the electrical heater is equal to the measured power input to the heater [Eq. (4.10)] and the heat gained by the fluid is determined as

$$q''_{R,T} = \dot{m}_R c_{P,R}\left(T_{elec,out} - T_{elec,in}\right) \tag{C1}$$

The preheater energy balance is given in Table C1.

Table C1 – Preheater energy balance results.

Case	Electrical Heater Power Input (W)	Refrigerant Heat Gain (W)	Difference in Heat Balance (W)	Difference in Heat Balance (%)
1	7.4	11.8	0.81	9.9
2	28.4	26.2	-1.10	-4.0
3	29.0	37.7	0.68	2.3
4	67.2	71.9	1.64	2.4
5	89.6	95.2	6.22	6.5

In the energy balance, the maximum electrical heater power input is limited to 90W because a higher input would result in a two-phase flow.

After the preheater outlet, the flow must pass travel approximately 30cm before entering the heat exchange test section. In this section, there is potential for heat exchange to the surroundings. This heat exchange can be determined by measuring the temperature at the test section inlet and comparing it to temperature exiting the preheater, as stated in Eq. C2.

$$q''_{R,T} = \dot{m}_R c_{P,R}\left(T_{R,in} - T_{pre,out}\right) \tag{C2}$$

For each case presented in Table E1, the heat transfer with the surroundings in the section downstream of the preheater is shown in Table C2.

A review of the energy balance results shows that the discrepancy between the power input into the electrical preheater and the measured heat input into the refrigerant is less than 7W for the cases examined. This discrepancy is due to heat transfer with the surroundings. In the flow section after the preheater, the maximum heat gained by the refrigerant is 8W. These results indicate that the heat transfer with the surroundings will have a minimal effect in the two-phase flow experiments performed in this research because typical preheater power inputs of 500W are used in the two-phase flow studies. A 15W heat gain from the surroundings (7W from the preheater section, 8W in the flow section after the preheater) would result in a 3% discrepancy in the preheater input power.

Table C2 – Heat transfer with surroundings in section between preheater and test section.

Case	Refrigerant Heat Gain/loss (W)	Percent of Heat Gain/Loss Compared with Preheater Input (%)
1	3.6	49
2	-1.1	-3.8
3	8.0	27.5
4	3.0	4.5
5	-0.6	-0.7

C.2 Energy Balance of Heat Exchange Test Section

An energy balance in the heat exchange test section was performed by comparing the heat lost by a single-phase refrigerant flowing in the tube side [Eq. (4.5)] and the heat gained by a flow of water on the shell side [Eq. (4.3)]. In this analysis, thermocouples were used to measure the refrigerant temperatures and RTDs were used to measure the water temperature. The energy balance results are given in Table C3. The energy balance results show that the maximum of discrepancy in the heat balance is approximately 2W (or 5%). In the two-phase flow investigations performed in this thesis, the typical heat loss in the refrigerant is approximately 70W. A 2W heat gain from the surroundings would results in a discrepancy of 2.9%.

Table C3 – Energy balance results of heat exchange test section.

Case	Refrigerant Heat Loss (W)	Water Heat Gain (W)	Difference in Heat Balance (W)	Difference in Heat Balance (%)
1	37.5	37.4	0.045	0.1
2	36.8	36.0	0.735	2.0
3	46.4	44.1	2.33	5.0

C.3 Energy Balance of Condenser

An energy balance in the condenser used to remove heat from the refrigerant was performed by comparing the heat lost by a single-phase refrigerant to the heat gained by a flow of water on the shell side. All measurements were taken using thermocouples and the energy balance results are given in Table C4. The energy balance results for the condenser show that there is a large discrepancy in the heat balance for all three cases tested. This error is believed to be due to an inaccurate prediction of the water heat gain as a result of using a rotameter to measure the water flow rate. It is recommended that this flow measurement device be replaced with a high precision flow meter if minimizing the discrepancy in the energy balance is desired. However, the measurement of energy in the condenser has no influence on the heat transfer results measured in the test section and minimizing the error in the condenser energy balance may not be a concern.

Table C4 – Condenser energy balance results.

Case	Refrigerant Heat Loss (W)	Water Heat Gain (W)	Difference in Heat Balance (W)	Difference in Heat Balance (%)
1	49.4	70.4	21.0	42.6
2	63.3	82.5	19.2	30.3
3	92.2	113.5	21.3	23.1

Appendix D – Numerical Simulations of Electric Field Strength

Numerical simulations to evaluate the electric field strength in an annular electrode configuration for various two-phase flow patterns were first presented by Cotton (2003). Cotton solved the electric field strength in a 2D cross-section for an annular and inverse annular flow pattern and solved for only the interfacial electric field strength in the stratified flow pattern case. In the model by cotton, the boundary conditions were a specified 8kV potential at the inner rod and a grounded condition at the surrounding tube. The tube wall thickness was not considered in the model.

The numerical simulations presented in this section are an expansion of the original work by Cotton (2003). In these simulations, the tube wall is modeled, which is required because the flow visualization section contains a quartz tube coated with an electrically conducting film of tin-oxide on the outer surface and the in the heat exchange test section a stainless steel tube is used. The differences in the electric field strength between these two cases are evaluated and will provide insight into whether the flow patterns observed inside the quartz tube are representative of the flow patterns inside the stainless steel tube.

D.1 The Numerical Model

A two-dimensional, numerical model was developed to evaluate the electric field strength inside a grounded quartz and stainless steel tube with high voltage applied to a concentric rod electrode inside the tube. The difference in the tubes is that quartz is a dielectric ($\varepsilon_r = 4.2$) and steel is an electrical conductor. The electrostatic equations for the two-phase domain are solved using the commercial finite element software package COMSOL Multiphysics 3.5. The electric field strength will be determined for three different flow distributions; a stratified flow, an inverse annular flow and an inverse annular flow along a liquid stratum. The electrostatic equations governing the electric field strength and solved using the finite element package are presented in equations D1 to D8. In the determination of the electric field strength, Gauss's law is first presented

$$\nabla \cdot \bar{D} = \rho_e \tag{D1}$$

If the dielectric fluid is assumed to be linear, isotropic and homogenous, the electric displacement can be described as

$$\bar{D} = \varepsilon \bar{E} \tag{D2}$$

Substituting in Eq. (D1) into Eq. (D2) yields

$$\nabla \cdot \bar{E} = \frac{\rho_e}{\varepsilon} \tag{D3}$$

In the absence of a change in the magnetic field, Faraday's law of induction gives

$$\nabla \times \bar{E} = \frac{\partial \bar{B}}{\partial t} = 0 \tag{D4}$$

Since the curl of the electric field is zero, the electric field can be defined by a scalar electric potential field, V

$$\bar{E} = -\nabla \mathrm{V} \tag{D5}$$

The electrical potential can be determined by substituting in Eq. (D3) into Eq. (D5) to give

$$\nabla^2 V = -\frac{\rho_e}{\varepsilon} \tag{D6}$$

In the simulations, it was assumed that there are no space and surface charges within the fluid. Therefore Eq. (D6) can be simplified to the Laplace equation to solve for the voltage potential

$$\nabla^2 V = 0 \tag{D7}$$

The boundary conditions used in solving the electrostatic equations is a specified voltage at the inner rod electrode and a ground condition at the outer tube surface. The electric field strength will be determined for the two flow distributions not evaluated by Cotton (2003), which are a stratified flow and an inverse annular flow with a lower liquid stratum. A grid independence study was performed for both flow distribution cases inside a quartz tube to determine the electric field strength for a meshes consisting of approximately 10000, 45000, 55000, 65000 and 75000 elements. In all cases, the error between successive mesh increases was found to be less than 0.1%. Therefore, the mesh of approximately 45000 elements is used to evaluating the electric field strength in both the flow distributions. Details of the flow distribution and mesh for the two flow distribution cases are shown in Figure D1 and Figure D2.

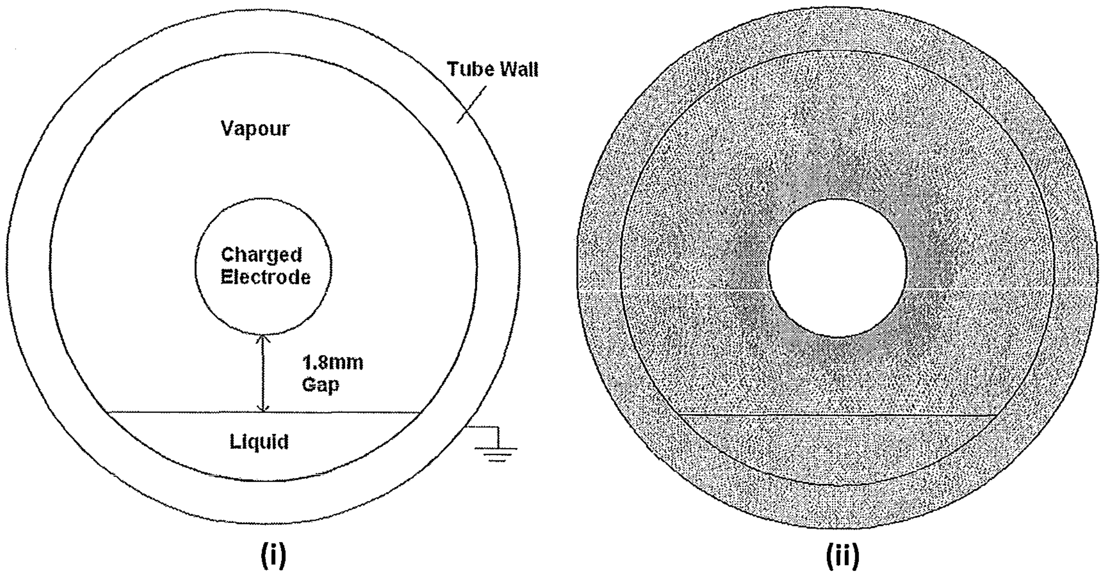

Figure D1 – Details of the (i) flow distribution domain and (ii) mesh for a stratified

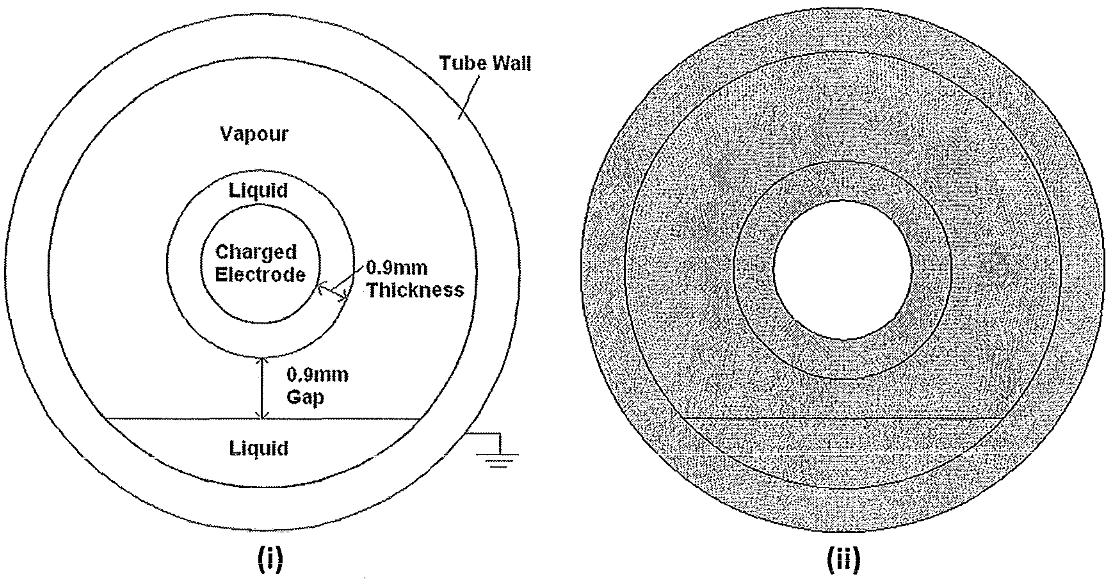

Figure D2 – Details of the (i) flow distribution domain and (ii) mesh for an inverse annular flow with a lower liquid stratum.

D.2 Electric Field Strength Results

D.2.1 Electric Field Strength in a Stratified Flow

The electric field strength distribution in a stratified flow for both a quartz and stainless steel tube is presented in Figure D3 and a plot electric field strength taken along the line profile is shown in Figure D4. From the numerical simulations, the highest electric field strength is observed to be near the central electrode, which explains the liquid extraction from the lower liquid stratum and onto the rod electrode observed in the experiments in Chapter 6. A comparison of the electric field strength of the quartz and stainless steel tubes shows that the maximum deviation in the electric field strength is 7.5% and the plot in Figure D4 shows that the trends in the distribution are also similar.

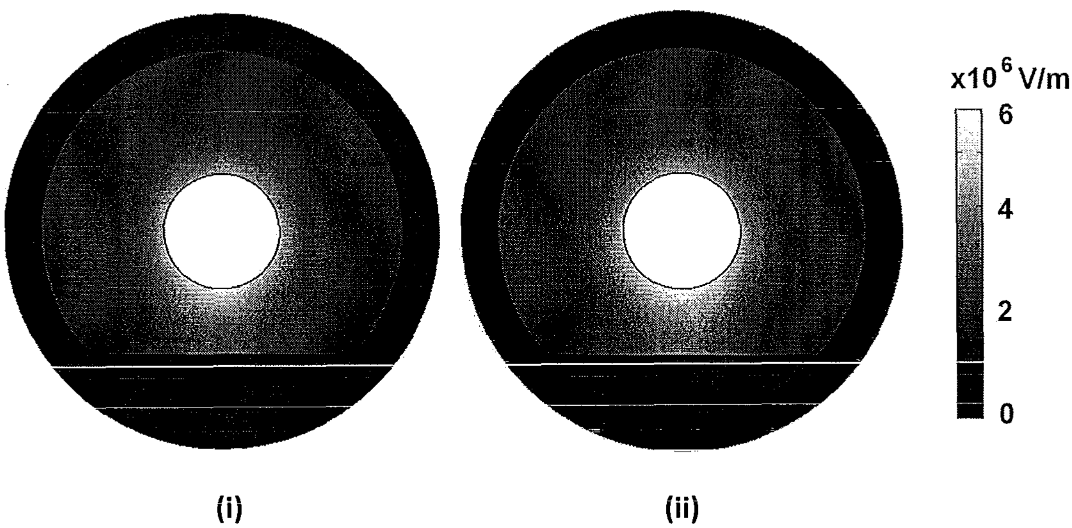

Figure D3 – Electric field strength distribution for a stratified flow distribution and an applied 8kV potential for the case of (i) a quartz outer tube and (ii) a stainless steel outer tube.

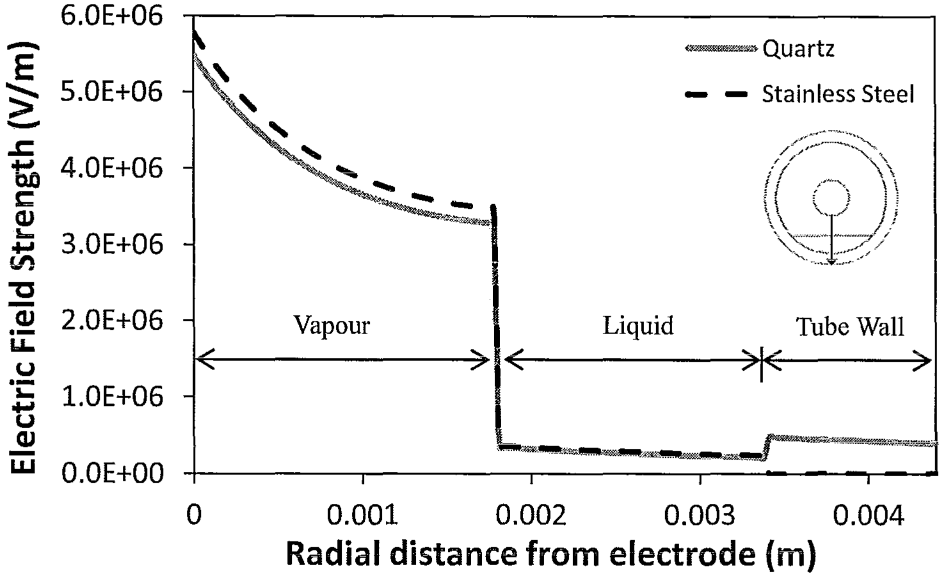

Figure D4 – Electric field strength distribution, taken along the profile indicated in Figure D3, for a quartz and stainless steel outer tube.

Therefore, it may be expected that the flow pattern observed in the quartz section is representative of the flow pattern in the heat exchange section.

D.2.2 Electric Field Strength in an Inverse Annular Flow with a Lower Liquid Stratum

The electric field strength distribution in an inverse annular flow with a lower liquid stratum for both a quartz and stainless steel tube is presented in Figure D5 and a plot electric field strengths taken along the line profile is shown in Figure D6. From the numerical simulations, the highest electric field strength is observed to be in the vapour region surrounding the liquid encircling the rod electrode. Therefore, according to the liquid extraction phenomenon, the liquid is expected to repulse from the rod electrode. A comparison of the electric field strength for both the quartz and stainless steel tubes shows that the maximum deviation in the electric field strength for this flow distribution is 11.4%. The plot in Figure D6 shows that the trends in the distribution are once again similar and therefore these simulation results suggest that the flow pattern observed in the quartz section is representative of the flow pattern in the heat exchange section.

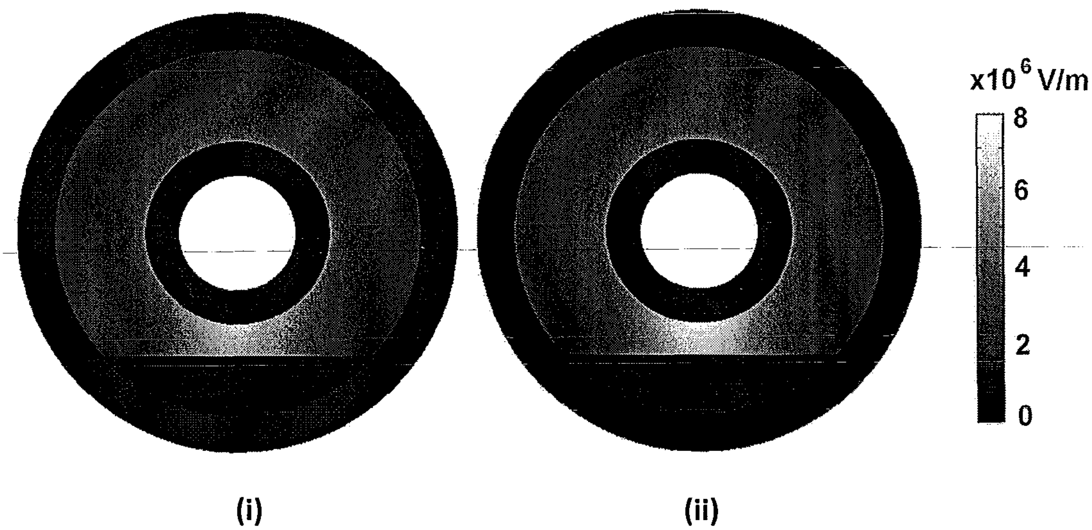

Figure D5 – Electric field strength distribution for an inverse annular flow with a lower liquid stratum and an applied 8kV potential for the case of (i) a quartz outer tube and (ii) a stainless steel outer tube.

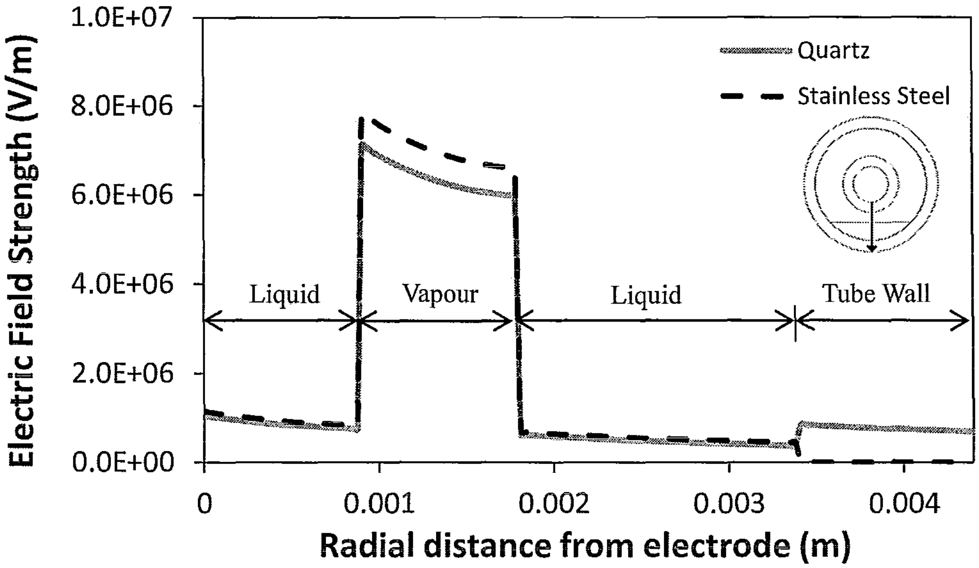

Figure D6 – Electric field strength distribution, taken along the profile indicated in Figure D5, for a quartz and stainless steel outer tube.

Appendix E – Two-Phase Flow Measurements using an Ultrasonic Technique

It is discussed in Chapter 7 that one of the mechanisms involved in the enhancement of heat transfer is due to the removal of the liquid thermal resistance from the heat transfer surface and into the central core. A potential method in measuring the liquid thickness in contact with the heat transfer surface is by using an ultrasonic technique. In this section, the fundamentals of the ultrasonic technique in measuring liquid thicknesses are presented followed by a discussion on the suitability of applying this measurement technique to the current experimental facility.

E.1 Fundamentals of Measuring Liquid Thickness in a Two-Phase Flow using the Ultrasonic Technique

The ultrasonic technique may be used to measure thickness by passing a sound wave through a material and measuring the time elapsed before an echo is returned. If the speed of sound through the material is known, then the thickness of the material can be determined as follows

$$d = {}^{ct}/_{2} \tag{E1}$$

where d is the thickness of the material, c is the speed of sound through a particular material and t is the time between measured pulses in a particular material. An echo is produced when the sound wave passes through an interface when there is a change in the acoustic impedance. A change in the acoustic impedance can be a result of changes in material or phase. The transmission and reflection process in an ultrasonic test measurement is illustrated in Figure E1.

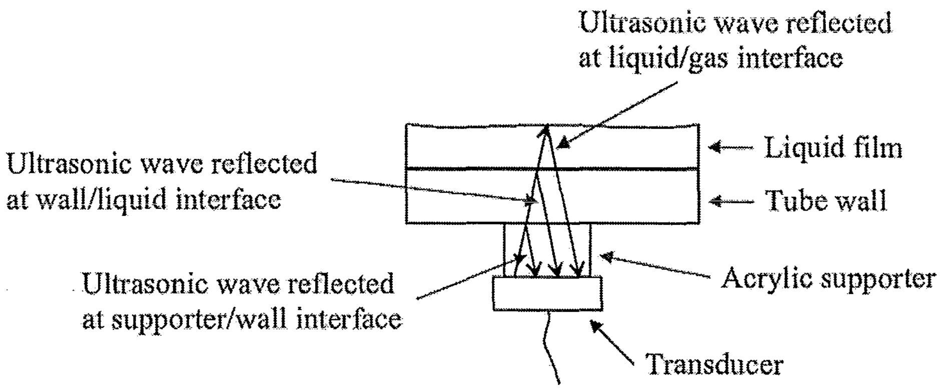

Figure E1 – Illustration of the pulse-echo method of used in the measurement of a liquid film thickness [Fiedler 2003].

E.2 Experimental Set-Up of the Ultrasonic Measurement System

The ultrasonic system used to measure liquid thickness consists of an Olympus M116H ultrasonic transducer (diameter of 6.35mm, 20MHz frequency) to emit and receive the sound pulse, a Panametric 5052UA ultrasonic analyzer to control the pulse emitted by the transducer and to convert the echo returned to the transducer to an electrical energy (voltage) and an Agilent 54621A oscilloscope to display the electrical energy data from the ultrasonic analyzer (i.e. a pulse echo waveform). The ultrasonic transducer used in this set-up is currently the smallest transducer currently available. A ultrasonic couplant was used between the transducer and test section to minimize noise in the measurement. A schematic of this test set-up is shown in Figure E2.

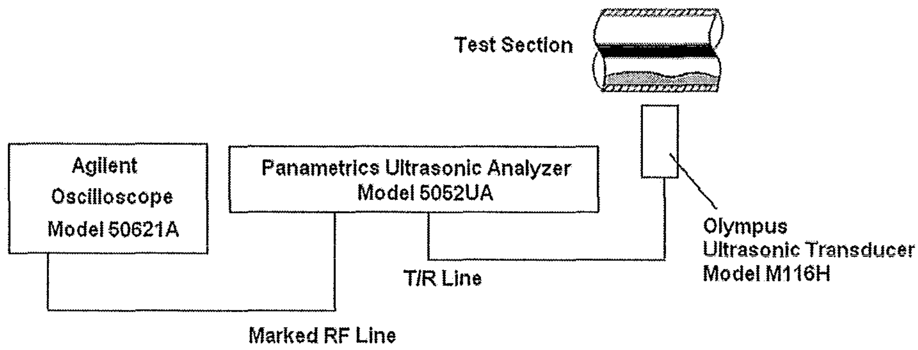

Figure E2 – Schematic of ultrasonic measurement system.

The ultrasonic system was calibrated using a glass beaker (wall thickness of 1mm) filled with various known thicknesses of water (4mm, 7mm and 9mm). The pulse echo waveform (average of 512 readings) of the 7mm thickness of water is shown in Figure E3. The speed of sound in water and quartz glass is 1483m/s and 5800m/s respectively [Olympus (2010)]. Therefore, the thickness of water is determined to be 7.13mm the from the pulse echo waveform. The error in the measurement is due to difficulties of identifying the exact echo corresponding to the liquid-air interface in the pulse echo waveform.

E.3 Measurement of R-134a Liquid Thickness using Ultrasonics

The ultrasonic technique was applied to the flow visualization section of the EHD loop in an attempt to measure the liquid thickness. The speed of sound in refrigerant R-134a for the test conditions is 495.94m/s [Guedes and Zollweg (1992)]. Two cases were investigated; one with a single-phase flow of liquid inside the annular channel to identify

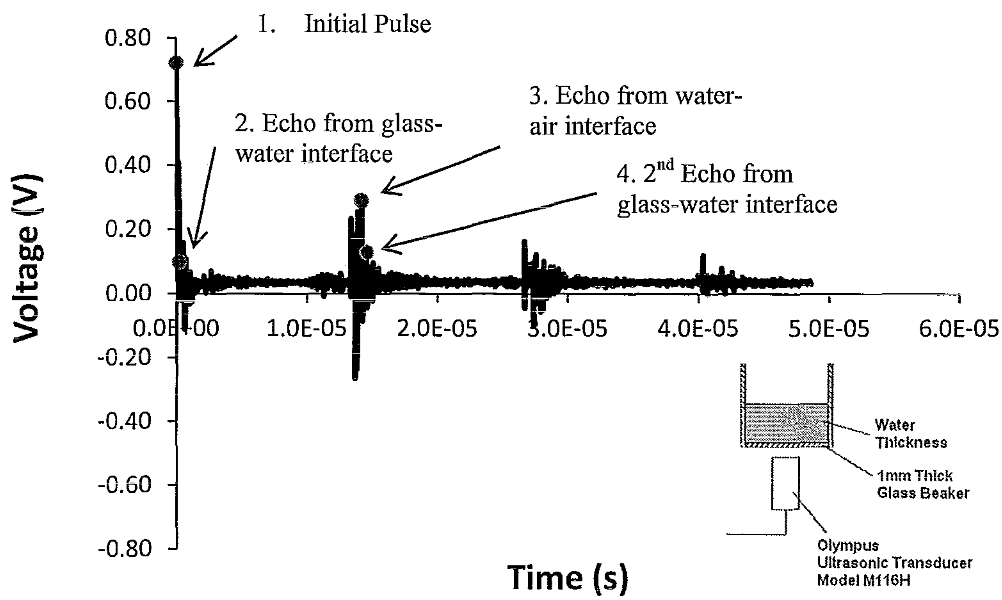

Figure E3 – Pulse echo waveform (average of 512 readings) of the measurements of a 7mm height of water inside a 1mm thick glass beaker.

the echo corresponding to the rod electrode and the second was a two-phase stratified flow pattern (mass flux of 55kg/m^{2}s and quality of 65%) to determine the height of the liquid stratum. In both cases, the ultrasonic transducer was placed on the bottom of the tube. The pulse echo waveform (average of 512 readings) for the single-phase flow and the two-phase stratified flow is shown in Figures E4 and E5 respectively.

A review of the pulse echo waveform for the two cases shows that the current set-up of the ultrasonic measurement system is not suitable for this particular geometry. For the case of a single-phase flow, no discernable echo was observed in the waveform and in the two-phase flow case, the echo corresponding to the liquid-vapour interface could not be identified. The ultrasonic technique was not successful in determining the liquid thickness in this geometry because of the curvature of the tube and rod. Figure E6 shows

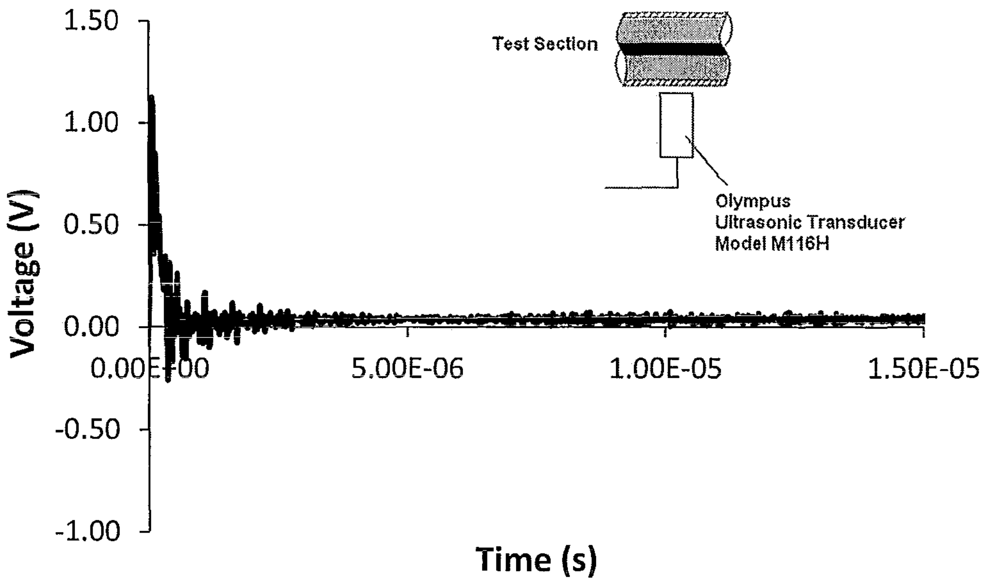

Figure E4 – Pulse echo waveform (average of 512 readings) of the measurements of a single-phase flow of R-134a inside the flow visualization test section.

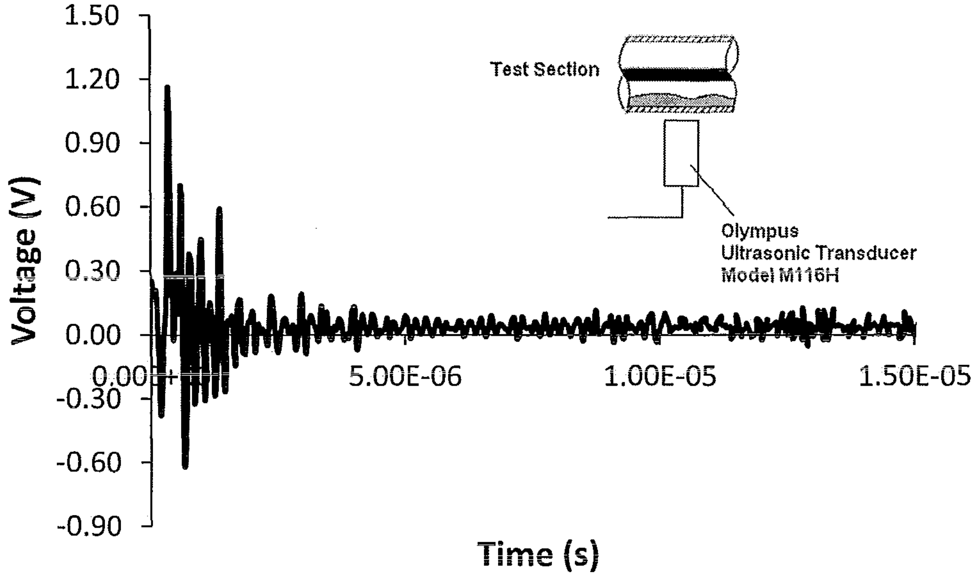

Figure E5 – Pulse echo waveform (average of 512 readings) of the measurements of a two-phase flow of R-134a ($G=55kg/m^2s$, $x=65\%$) inside the flow visualization test section.

the dimensions of the transducer to the test section and it is evident that the flat transducer cannot be completely mated to the curved tube. The ultrasonic transducer used in the experiments is currently the smallest probe available. In addition the curvature of the tube will result in multiple echos because of the non-flat interface. This multiple echo problem is also present with the rod electrode in the center of the tube. This explains the multiple echos observed in Figure E5. Therefore, it can be concluded that the ultrasonic technique is not suitable in this geometry, but as shown in the calibration tests in the previous section, it may be suitable technique in other test section geometries or when a smaller probe becomes available.

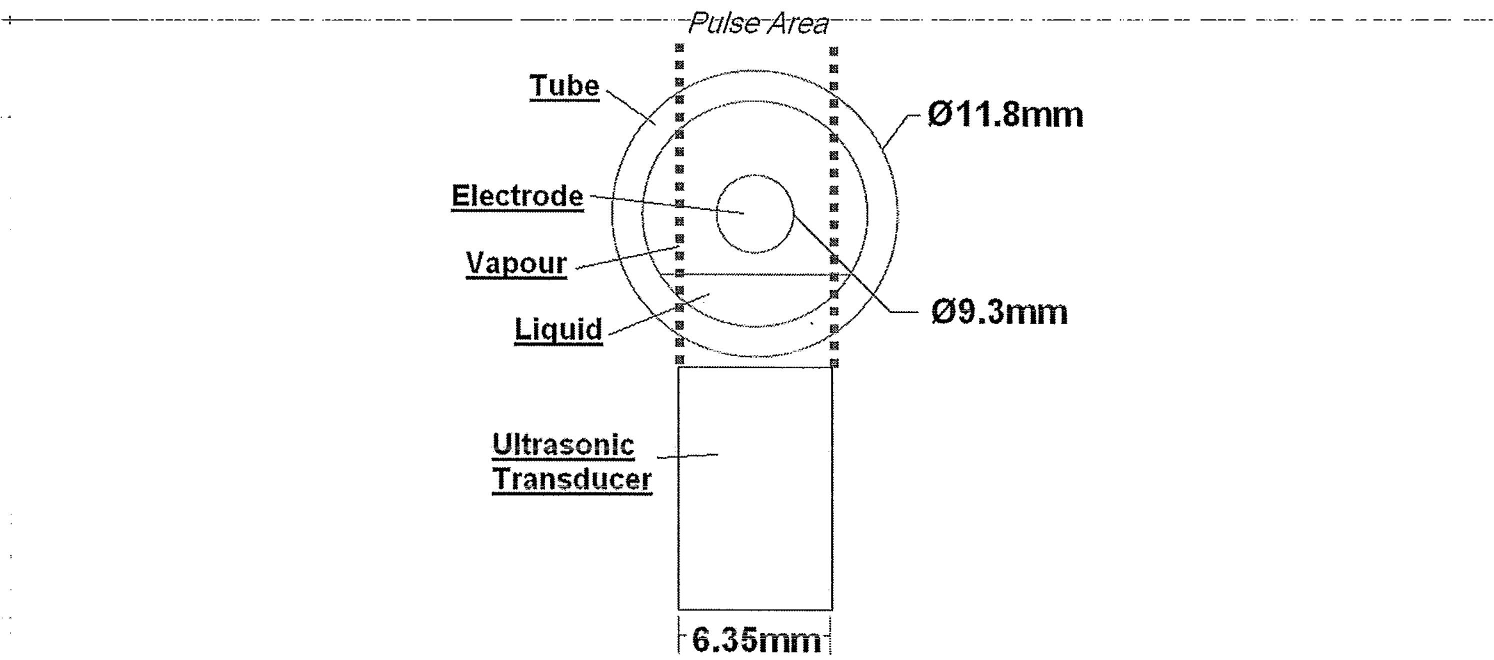

Figure E6 – Pulse echo waveform (average of 512 readings) of the measurements of a two-phase flow of R-134a (G=55kg/m^{2}s, x=65%) inside the flow visualization test section.

References

ASHRAE. (2001). Thermophysical properties of refrigerants. In *ASHRAE Handbook-Fundamentals, SI Edition.* ASHRAE Inc.

Atten, P., & Castellanos, A. (1995). Injection induced electrohydrodynamic flows. In J.S. Chang, A. J. Kelly, & J. M. Crowley, *Handbook of Electrostatic Processes* (pp. 121-146). New York: Marcel Dekker .

Atten, P., & Lacroix, J. C. (1978). Electrohydrodynamic stability of liquids subjected to unipolar injection: non linear phenomena. *Journal of Electrostatics, 5*, 439-452.

Avsec , D., & Luntz, M. (1937). *Comptes-Rendus, 204*, 420-428.

Azer, N. Z., Abis, L. V., & Soliman, H. M. (1972). Local heat transfer coefficients during annular flow condensation . *ASHRAE Transactions, 78*(2), 135-143.

Baker, O. (1954). Design of pipelines for simultaneous flow of oil and gas. *Oil and Gas Journal, 53*, 185-195.

Bologa, M. K., & Didkovesky, A. B. (1977). Enhancement of heat transfer in film condensation of vapour of dielectric fluid by superposition of electric fields. *Heat Transfer - Soviet Research, 9*(1), 147-151.

Breber, G., Palen, J. W., & Taborek, J. (1980). Prediction of horizontal tube-side condensation of pure components using flow regime criteria. *Journal of Heat Transfer, 102*, 471-476.

Carpenter, E. F., & Colburn, A. P. (1951). The effect of vapor velocity on condensation inside tubes. *Proceedings of General Discussion on Heat Transfer* (pp. 20-26). Inst. Mech. Eng. and ASME.

Cavallini, A., & Zecchin, R. (1974). A dimensionless correlation for heat transfer in forced-convective condensation . *Proceedings of the Fifth International Heat Transfer Conference, Japan Society of Mechanical Engineers, 3*, 309-313.

Cavallini, A., Censi, G., Del Col, D., Doretti, L., Longo, G. A., & Rossetto, L. (2002). Intube condensation of halogenated refrigerants. *ASHRAE Transactions, 108.*

Chang, J. S., & Watson, A. (1994). Electromagnetic hydrodynamics. *IEEE Transactions on Dielectrics and Electrical Insulation, 1*(5), 871-895.

Chato, J. C. (1962). Laminar condensation inside horizontal and inclined tubes. *ASHRAE Journal, 4*, 52-60.

Chisholm, D., & Laird, A. D. (1949). Two-phase flow in rough tubes. *Transactions ASME, 45*(1), 39-48.

Choi, H. Y. (1968). Electrohydrodynamic condensation heat transfer. *ASME Journal of Heat Transfer, 90*, 98-102.

Chu, B. T. (1959). Thermodynamics of electrically conducting fluids. *Physics of Fluids, 2*(5), 98-102.

Coelho, R. (1979). *Physics of Dielectrics for the Engineer.* New York: Elsevier Scientific Publishing Company.

Collier, J. G., & Thome, J. R. (1994). *Convective Boiling and Condensation.* Oxford: Clarendon Press.

Cotton , J. S., Brocilo, D., Shoukri, M., Smith-Pollard, T., & Chang, J. S. (1998). Mechanisms of electrohydrodynamic flow boiling heat transfer in coaxial flow channels of dielectric refrigerant R-134a. *IEEE Conference of Electrical Insulation and Dielectric Phenomena, 1*, 178-181.

Cotton, J. S. (2009). Electrohydrodynamic condensation heat transfer mechanisms under dc and ac applied voltages in a horizontal annular channel. *IEEE Transactions on Dielectrics and Electrical Insulation*(EHD Special Issue), 495-503.

Cotton, J. S., Brocilo, D., Chang, J. S., Shoukri, M. M., & Smith-Pollard, T. (2003). Numerical simulation of electric field distributions in electrohydrodynamic two-phase flow regimes. *IEEE Transactions on Dielectrics and Electrical Insulation, 10*(1), 37-51.

Cotton, J. S., Brocilo, D., Chang, J. S., Shoukri, M., & Smith-Pollard, T. (2003). Numerical simulation of electric field distributions in electrohydrodynamic two-phase flow regimes. *IEEE Transactions on Dielectrics and Electrical Insulation, 10*(1), 37-51.

Cotton, J. S., Shoukri, M., & Chang, J. S. (2001, August). Oscillatory entrained droplet EHD two-phase flow. *ASME Journal of Heat Transfer, 123*, 622.

Crowley, J. M. (1995). Electrostatic Fundamentals. *Handbook of Electrsostatic Processes*, 1-23.

Denat, A., Gosse, J. P., & Gosse, B. (1988). Electrical conduction of purified cyclohexane in divergent electric field. *IEEE Transactions on Electrical Insulation*, 545-554.

Drnovsek, J., Pusnik, I., & Bojkovski, J. (1998). Reduction of uncertainties in temperature calibrations by comparison. *Measurement Science and Technology* , *9*(11), 1907-1911.

Dukler, A. E. (1960). Fluid mechanics and heat transfer in vertical falling-film systems. *Chemical Engineering Progress Symposium Series 56, 30*, 1-10.

DuPont. (2005). *Transport Properties of DuPont Suva Refrigerants.*

Dyakowski, J., Trommelmans, J., & Berghmans, J. (1982). Theoretical investigation of the effect of an electric field upon vertical plate condensation heat transfer. *Proceedings in the Seventh International Heat Transfer Conference*, *5*, pp. 65-70.

El Hajal, J., Thome, J. R., & Cavallini, A. (2003). Condensation in horizontal tubes, part 1: two-phase flow pattern map. *International Journal of Heat and Mass Transfer, 46*, 3349-3363.

Faraday, M. (1838). *Experimental Researches* (Vol. 1). Dover Publications.

Fiedler, S., Yildiz, S., & Auracher, H. (2003). Determination of film thickness and flooding during reflux condensation in a small, inclined tube with an ultrasonic transducer. *International Journal of Energy Research, 27*, 315-325.

Friedel, L. (1979). Improved friction pressure drop correlatoins for horizontal and vertical two-phase pipe flow. *European Two Phase Flow Group Meeting*, Paper E2.

Fujino, T., Yokoyama, Y., & Mori, Y. H. (1989, May). Augmentation of Laminar Forced-Convective Heat Transfer by the Application of a Traverse Electric Field. *Journal of Heat Transfer, 111*, 345-351.

Gemant, A. (1929). Electrotech. *Zeit, 34*, 1225.

Grassi, W., Testi, D., & Saputelli, M. (2005). Heat transfer enhancement in a vertical annulus by electrophoretic forces acting on a dielectric liquid. *International Journal of Thermal Sciences, 44*, 1072-1077.

Hashizume, K. (1983). Flow pattern and void fraction of refrigerant two-phase flow in a horizontal pipe. *Bull JSME* , *26*, 1597-1602.

Hewitt, G. F. (1981). *ASME/AIChE 20th Heat Transfer Conference.* D.Q. Kemn Lecture.

Honda, T., & Atten, P. (1978). Electroviscous effect in poiseuille flow under electrolysis condition. *Proceedings of the 6th International Conference on Conduction and Breakdown in Dielectric Liquids*, 315-320.

Hopfinger, E. J., & Gosse, J. P. (1971). Charge transport by self-generated turbulence in insulating liquids submitted to unipolar injection. *The Physics of Fluids, 14*, 1671-1682.

Jaster, H., & Kosky, P. G. (1976). Condensation in a mixed flow regime. *International Journal of Heat and Mass Transfer, 19*, 95-99.

Jonassen, N. (1998). *Electrostatics.* New York: Chapman and Hall.

Kattan, N., Thome, J. R., & Favrat, D. (1998). Flow boiling in horizontal tubes: Part 1 - Development of a diabatic two-phase flow pattern map. *Journal of Heat Transfer, 120*, 140-147.

Kline, S. J., & McClintock, F. A. (1953). Describing uncertainties in single-sample experiments. *Mechanical Engineering, 75*(1), 3-8.

Kosky , P. G., & Staub, F. W. (1971). Local condensing heat transfer coefficients in the annular flow regime. *AIChE Journal, 17*(5), 1037-1043.

Kreith , F., & Bohn, M. S. (2001). *Principles of Heat Transfer* (6 ed.). Brooks/Cole.

Kuffel, E., Zaengl, W. S., & Kuffel, J. (2000). *High Voltage Engineering: Fundamentals* (2 ed.). Oxford: Butterworth-Heinemann.

Lacroix, J. C., Atten, P., & Hopfinger, E. J. (1975). Electro-convection in dielectric liquid layer subjected to unipolar injection. *Journal of Fluid Mechanics*, 539-563.

Landau, L. D., & Lifshitz, E. M. (1960). *Electrohydrodynamics of Continuous Media.* Pergamon Press Ltd.

Lockhart, R. W., & Martinelli, R. C. (1949). Proposed correlation of data for isothermal two-phase, two-component flow in pipes. *Chemical Engineering Progress, 45*(1), 39-48.

Melcher, J. R. (1981). *Continuum Electromechanics.* Cambridge, Massachusetts: M.I.T. Press.

Ng, K., Ching, C. Y., & Cotton, J. S. (2010, August). Transient two-phase flow patterns by application of a high voltage pulse width modulated signal and the effect on condensation heat transfer. *Proceedings of the 14th International Heat Transfer Conference.* Washington , D.C.: ASME.

Olympus. (2010). *Material sound velocities.* Olympus NDT.

Omega. (2004). The Temperature Handbook. Indianapolis: Curtis Publishing.

Raisin, J., Atten, P., Reboud, J. L., & Pollet, C. (2010). On-demand EHD injection of electrically neutral water droplets in oil. *7th Conference of the French Society of Electrostatics SFE 2010.* Montpellier, France.

Raisin, J., Reboud, J. L., & Atten, P. (2009). Electrocoalescence of two water drops in oil: experiment and modeling. *International Journal of Plasma Environmental Science and Technology, 3*(2), 127-132.

Rosson, H. F., & Myers, J. A. (1965). Point values of condensing film coefficients inside a horizontal tube. *Chemical Engineering Progress Symposium Series, 61*(59), 190-199.

Sadek, H. (2009). *Electrohydrodynamic control of convective condensation heat transfer and pressure drop in a horizontal annular channel.* PhD Dissertation, McMaster University.

Sadek, H., Ching, C. Y., & Cotton, J. S. (2010). Characterization of heat transfer modes of tube side convective condensation under the influence of an applied DC voltage. *International Journal of Heat and Mass Transfer, 53*, 4141-4151.

Shah, M. M. (1979). A general correlation for heat transfer during film condensation inside pipes. *International Journal of Heat and Mass Transfer, 22*, 547-556.

Shrimpton, J. (2009). *Charge Injection Systems: Physical Principles, Experimental and Theoretical Work.* Berlin: Springer Berlin Heidelberg.

Singh, A. (1995). *Electrohydrodynamic (EHD) Enhancement of In-Tube Boiling and Condensation of Alternate (Non-CFC) Refrigerants.* Ann Arbor: University of Maryland.

Singh, A., Ohadi, M. M., & Dessiatoun, S. (1997). Electrohydrodynamic (EHD) enhancement of in-tube condensation heat transfer of althernative refrigerants R-134a in smooth and microfin tubes. *ASHRAE Transactions, 103*(1), 813-823.

Smirnov, G. F., & Lunev, V. G. (1978). Heat transfer during condensation of vapour of dielectric in electric field. *Applied Electrical Phenomena, 2*, 37-42.

Soliman, H. M., Schuster, J. R., & Berenson, P. J. (1968). A general heat transfer correlation for annular flow condensation. *ASME Journal of Heat Transfer, 90*, 267-276.

Steiner, D. (1993). Heat transfer to boiling saturated liquids. *VDI-Wrmeatlas (VDI Heat Atlas).*

Suzuki, M., & Sawada, Y. (1983). Relative stabiities of metastable states of convecting charged-fluid systems by computer simulation. *Physical Review A, 27*, 478-489.

Taitel , Y., & Dukler, A. E. (1976). A model for predicting flow regime transitions in horizontal and near horizontal gas-liquid flow. *AIChE Journal , 2*, 43-55.

Tandon, T. N., Varma, H. K., & Gupta, C. P. (1982). A new flow regime map for condensation inside horizontal tubes. *Journal of Heat Transfer, 104*, 763-768.

Traviss, D. P., Rohsenow, W. M., & Baron, A. B. (1973). Forced-convection condensation inside tubes: A heat transfer equation for condenser design. *ASHRAE Transactions, 79*, 157-165.

Trommelmans, J., Janssens, J., Maelfat, F., & Berghmans, J. (1985). Electric field heat transfer augmentation during condensation of nonconducting fluids on a horizontal surface. *IEEE Transactions on Industry Applicatoins , 2*, 530-534.

Turnbull, R. (1968). Electroconvective instability with a stabilizing temperature gradient. I. Theory II. Experimental results. *Physics of Fluids*, 2588-2603.

Webb, R. L., & Kim, N.-H. (2005). *Principles of Enhanced Heat Transfer.* New York: Taylor and Francis Group.